

# **Measurement of Axial Induction Factor for a Model Wind Turbine**

*A thesis submitted to the College of Graduate Studies and Research in partial*

*fulfillment of the requirements for the degree of*

*Master of Science*

*in the*

*Department of Mechanical Engineering*

*University of Saskatchewan*

**by**

**Abul Fahad Akon**

# Permission to Use

In presenting this thesis in partial fulfilment of the requirements for a postgraduate degree from the University of Saskatchewan, I agree that the libraries of this University may make it freely available for inspection. I further agree that permission for copying of this thesis in any manner, in whole or in part, for scholarly purposes may be granted by the professor who supervised my thesis work or, in their absence, by the Head of the Department or the Dean of the College in which my thesis work was done. It is understood that any copy or publication or use of this thesis or parts thereof for financial gain shall not be allowed without my written permission. It is also understood that due recognition shall be given to me and to the University of Saskatchewan in any use which may be made of any material in my thesis.

Requests for permission to copy or to make other use of material in this thesis in whole or part should be addressed to:

Head of the Department of Mechanical Engineering

University of Saskatchewan

Saskatoon, Saskatchewan S7N 5A9

# Abstract

Understanding the velocity field information near the rotor plane of a wind turbine at various operating conditions is very important to understanding the aerodynamic performance of the wind turbine. Investigation of these flow fields has been an important area of study in experimental fluid dynamics for the last few decades. It is more convenient and cost effective to perform experiments with scaled-down model wind turbines rather than taking measurements around a full-scale model. Along with different experimental techniques, computational models to predict the performance of wind turbines have been developing. The basis of most of the commercially available codes is the Blade Element Momentum (BEM) method. However, the applicability and performance of these codes are often questionable at different operating conditions. Therefore, it is necessary to validate these codes with different wind turbine designs under a large variety of operating conditions. In this research project, two-dimensional PIV measurements near the rotor plane of a three-bladed, horizontal axis model wind turbine were taken at six different operating conditions and at 15 azimuthal angles. The results are presented in terms of axial induction factor. The radial distribution of axial induction factor at the rotor plane was compared to the results obtained from WT\_Perf, a typical BEM method. BEM fails to predict of the value of axial induction factor at the tip region for most of the operating conditions. However, the predictions are good at the root region. At the mid-span region, BEM has good predictions for operating conditions higher than the optimum operating condition, better in the optimum operating conditions and differs significantly at the operating conditions lower than optimum tip-speed ratio. The datasets obtained from the experiment will serve as a very good database for code designers for the validation of codes and development of models.

# Acknowledgements

First, I would like to express my heartiest respect and sincere gratitude to my supervisor, Professor James Donald Bugg, who has supported me throughout my thesis research with his patience, valuable knowledge and directions while allowing me the room to work in my own way. This work would have not been possible without his continuous help, guidance and confidence in my abilities.

I would also like to express my deepest appreciation and gratitude to my advisory committee members, Professor David Sumner and Professor David Torvi, who were always ready to answer all my questions and provide their valuable opinion regarding my thesis work whenever required without any hesitation.

My cordial thanks to Mr. Dave Deutscher for providing me all kinds of technical support needed during the data taking part of this thesis project.

I am very much thankful to Mr. Noorallah Rostamy for providing me with the Pitot tube boundary layer measurement datasets and also for helping me during PIV image analysis. Thanks also go to Mr. Andrew Schenstead for sharing his PIV datasets, a few of the figures and his experience with PIV measurements.

Last but not least, a credit goes out to some of my closest friends for their continuous help and support all through my program.

# Dedication

Dedicated to my parents, Mr. Abul Bashar Akon and Mrs. Ferdousi Begum.

# Table of Contents

Permission to Use .....	i
Abstract .....	ii
Acknowledgements .....	iii
Dedication .....	iv
Table of Contents .....	v
List of Tables .....	ix
List of Figures .....	x
Nomenclature .....	xiii
Acronyms .....	xv
<b>1 Introduction</b> .....	<b>1</b>
1.1 Flow around a Wind Turbine Rotor .....	2
1.2 Blade Element Momentum (BEM) Method .....	5
1.3 Motivation .....	7
1.4 Objectives .....	10
1.5 Organization of the Thesis .....	10
<b>2 Literature Review</b> .....	<b>12</b>
2.1 Introduction .....	12
2.2 Wake Velocity Measurements .....	12
2.3 Quantitative Flow Visualization Techniques .....	15

2.4 Global Properties and Comparison with Numerical Models .....	17
2.5 Computational Methods and Their Modifications .....	20
2.6 Experiments and Comparison with Numerical Analysis .....	23
<b>3 Experimental Setup and Instrumentation .....</b>	<b>33</b>
3.1 Introduction .....	33
3.2 Wind Tunnel .....	33
3.3 Freestream Velocity, Temperature and Density Measurement.....	35
3.4 Model Horizontal Axis Wind Turbine .....	35
3.5 Wind Turbine Speed Control Equipment .....	37
3.5.1 MAGTROL Hysteresis Brake .....	38
3.5.2 Encoder Wheel .....	39
3.5.3 Speed Controller .....	40
3.6 Temperature Sensor .....	40
3.7 Particle Image Velocimetry .....	41
3.7.1 Seeding and Illumination .....	42
3.7.2 Image Capture Equipment .....	44
3.7.3 PIV Trigger Equipment .....	44
3. 8 Uncertainty Analysis .....	45
3.8.1 Freestream Velocity .....	45
3.8.2 PIV Measurements of $U/U_\infty$ .....	45
3.8.3 Uncertainty in the Measurements of $U$ .....	48
3.8.4 Uncertainty in the Measurements of Axial Induction Factor .....	48

3.8.5 Uncertainty in Tip-Speed Ratio ( $\lambda$ ) .....	49
<b>4 The Experimental Approach .....</b>	<b>50</b>
4.1 Introduction .....	50
4.2 PIV Trigger Delay Calibration .....	50
4.3 Azimuthal Positions of the Turbine Blades .....	54
4.4 Operational Envelope of the Apparatus .....	55
4.5 The Run Matrix .....	56
4.6 PIV Image Calibration .....	59
4.7 PIV Image Capture .....	62
4.8 PIV Image Analysis .....	63
4.9 Image Masking .....	63
4.10 Outlier Rejection.....	64
<b>5 Results .....</b>	<b>65</b>
5.1 Introduction .....	65
5.2 Characteristic Curve .....	65
5.3 Velocity Field around the Rotor Plane .....	69
5.4 Axial Induction Factor .....	71
5.4.1 Variation of Axial Induction Factor in the Axial Direction .....	73
5.5 Radial Distribution of Axial Induction Factor at the Rotor Plane .....	78
5.5.1 Azimuthal Averaging of Axial Induction Factor at the Rotor Plane ...	80
5.6 Blade Element Momentum (BEM) results .....	83

<b>6 Conclusions and Recommendations</b> .....	90
6.1 Summary of Testing .....	90
6.2 Conclusions .....	91
6.3 Recommendations .....	92
6.4 Contribution to knowledge .....	94
<b>List of References</b> .....	95
<b>Appendix: The Effect of Blade Deflection on the Interpolation of Axial Induction Factor to the Rotor Plane</b> .....	99

# List of Tables

<b>Table</b>		<b>Page</b>
2.1	Summary of wind turbine aerodynamics studies.....	28
3.1	Dimensions of the Wind Tunnel.....	34
3.2	Uncertainties in tip-speed ratios ( $\lambda$ ).....	49
4.1	Operating conditions and locations of the Datasets.....	57
4.2	Sizes of the fields of view.....	58
4.3	The run matrix for the present experiments.....	58
5.1	Operating conditions and corresponding tip-speed ratios ( $\lambda$ ).....	82

# List of Figures

<b>Figure</b>		<b>Page</b>
1.1	Global status of wind power. (Data Source: GWEC Annual Market Report, 2010).....	2
1.2	One-dimensional analysis of the flow passing through the rotor plane of a wind turbine.....	3
3.1	Schematic Diagram of the Wind Tunnel (Reprinted from Adaramola, 2008).....	34
3.2	The model horizontal axis wind turbine; (a) mounted inside the wind tunnel and (b) the blade design.....	36
3.3	Schematic diagram of the model wind turbine mounted inside the wind tunnel and the coordinate system used. (Courtesy: Andrew Schenstead).....	37
3.4	The rotor and mount assembly of the MAGTROL Hysteresis Brake. (Image source: MAGTROL HB/MHB Data Sheet).....	38
3.5	Wind turbine rotor and magnetic brake shaft assembly.(Courtesy: Andrew Schenstead).....	39
3.6	Rear view of the encoder wheel. (Courtesy: Andrew Schenstead).....	40
3.7	Schematic diagram of the PIV system applied to the flow visualization around the rotor plane of a model horizontal axis wind turbine. (Courtesy: Andrew Schenstead for the Schematic Diagram of model HAWT and wind tunnel).....	42
3.8	Comparison of normalized velocity measurements within the boundary layer by the PIV and the Pitot tube.....	47

3.9	Distribution of $\Delta U/U_\infty$ obtained at 30 locations in the boundary layer.....	47
4.1	Plumb bob hanging from the tip of the quarter chord line at $\theta = 0^\circ$ ; (a) the string passing along the quarter chord line and (b) the string passing through rotor shaft centre.....	51
4.2	Laser sheet hitting the quarter chord line of Blade 1 at $0^\circ$ azimuth.....	52
4.3	Trigger delay calibration curve.....	53
4.4	Azimuthal Positions of Blade 1 where PIV measurements were taken (Courtesy: Andrew Schenstead for schematic of the blades).....	54
4.5	The experimental operational envelope.....	55
4.6	Operating characteristics curve for the model HAWT.....	56
4.7	Locations of the fields of view.....	59
4.8	Calibration images; (a) Root upstream field of view and (b) Tip downstream field of view.....	61
4.9	Portion of a raw image of tip field of view of the dataset $\lambda = 9.52$ at $\theta = 0^\circ$ .....	62
5.1	Comparison of characteristic curve obtained from the experiment and BEM method.....	67
5.2	A typical PIV vector field around the rotor plane of the model HAWT. ( $U_\infty = 14$ m/s and $N = 3000$ rpm).....	70
5.3	One of the tip vortices; (a) Tip vortex shown in a PIV raw image and (b) Velocity field in a tip vortex.....	71

5.4	Axial induction factor distribution over the whole flow field and the presence of periodic high induction bands; (a) operating condition: $U_\infty = 17$ m/s, $N = 4000$ rpm, $\theta = 15^\circ$ and (b) operating condition: $U_\infty = 17$ m/s, $N = 4000$ rpm and $\theta = 55^\circ$ .....	73
5.5	Axial variation of axial induction factor (a) $\theta = -15^\circ$ , (b) $\theta = 0^\circ$ , (c) $\theta = 15^\circ$ , (d) $\theta = 35^\circ$ (Operating condition $U_\infty = 17$ m/s, $N = 4000$ rpm and $\lambda = 6.16$ ).....	76
5.6	Axial variation of axial induction factor at $r/R=0.6$ for various azimuthal angles. (Operating condition $U_\infty = 17$ m/s, $N = 4000$ rpm and $\lambda = 6.16$ ).....	78
5.7	Radial distribution of axial induction factor (a) at different azimuthal angles. (Operating condition: $N = 3000$ rpm, $U_\infty = 14$ m/s and $\lambda = 5.61$ ).....	79
5.8	Azimuthal variation of axial induction factor (a).(Operating condition: $N = 3000$ rpm, $U_\infty = 14$ m/s and $\lambda = 5.61$ ).....	80
5.9	Azimuthally averaged radial distribution of axial induction factor (a) at different tip-speed ratios ( $\lambda$ ).....	82
5.10	Assessment of BEM predictions of axial induction factor for (a) $\lambda = 9.52$ (11 m/s and 4000 rpm), (b) $\lambda = 9.52$ (13.75 m/s and 5000 rpm), (c) $\lambda = 7.48$ (14 m/s and 4000 rpm), (d) $\lambda = 7.14$ (11 m/s and 3000 rpm), (e) $\lambda = 6.16$ (17 m/s and 4000 rpm and (f) $\lambda = 5.61$ (14 m/s and 3000 rpm).....	86
A.1	Radial distribution of axial induction factor (a) at the rotor plane considering and not considering bending effects at heavily loaded condition ( $\lambda = 6.16$ ).....	100

# Nomenclature

## *Roman alphabets*

$A$	Area of the rotor [ $\text{m}^2$ ]
$A_T$	Cross sectional area of the wind tunnel [ $\text{m}^2$ ]
$a$	Axial induction factor
$a'$	Tangential induction factor
$B$	Bias error
$C_D$	Drag coefficient
$C_L$	Lift coefficient
$C_p$	Power coefficient
$C_p^*$	Corrected power coefficient
$c$	Chord length [m]
$N$	Rotational speed [rpm]
$n$	Number of blades in the wind turbine
$P_\infty$	Absolute freestream static pressure [Pa]
$P_p$	Precision error
$R$	Radius of the rotor [m]
$R_a$	Specific gas constant for air [287 J/(kg. K)]
$r$	Radial distance from the axis of rotation [m]
$S$	Standard deviation

$T$	Torque [N.m]
$T_\infty$	Freestream temperature [K]
$U_\infty$	Freestream velocity [m/s]
$U_\infty^*$	Corrected freestream velocity [m/s]
$U$	Local velocity [m/s]
$U_1$	Velocity at the rotor plane [m/s]
$\dot{W}$	Power extracted by the wind turbine [W]
$\dot{W}_{wind}$	Power in the approaching wind [W]
$x$	Distance from the rotor plane [m]
$y$	Distance from the wind tunnel ground plane [m]

### ***Greek symbols***

$\alpha$	Angle of attack [degree]
$\phi$	Blade pitch angle [degree]
$\theta$	Azimuthal angle [degree]
$\Omega$	Rotational speed [°/s]
$\omega$	Wake angular velocity [rad/s]
$\rho$	Air density [kg/m <sup>3</sup> ]
$\lambda$	Tip-speed ratio
$\lambda^*$	Corrected tip-speed ratio

# Acronyms

AD	Actuator Disc
AF	Aerofoil
AL	Actuator Line
BEM	Blade Element Momentum
CFD	Computational Fluid Dynamics
FOV	Field of View
HAWT	Horizontal Axis Wind Turbine
HWA	Hot Wire Anemometry
IA	Interrogation Area
RNG	Re Normalized Group model
SST	Shear Stress Transport model
LDV	Laser Doppler Velocimetry
MEXICO	Model Experiments in Controlled Conditions
NACA	National Advisory Committee for Aeronautics
NREL	National Renewable Energy Laboratory
N-S	Navier Stokes
PIV	Particle Image Velocimetry
RANS	Reynolds Average Navier Stokes
UAE	Unsteady Aerodynamic Experiment

# Chapter 1: Introduction

Wind energy is a popular form of renewable energy due to its low carbon-dioxide (CO<sub>2</sub>) emissions compared to most conventional thermal power plants. Wind energy reduces the use of conventional fossil fuel and this ultimately helps to reduce the emissions of the gases responsible for the green house effect. The United States Department of Energy (DOE) and the American Wind Energy Association (AWEA) have predicted that by 2030 wind energy will contribute about 20% (around 300 GW) to the overall power demand in the United States and will reduce the emission of CO<sub>2</sub> by 25% (a cumulative total of more than 7.6 billion tons) (U. S. DOE, 2008). The analysis shows rapidly increasing demand for installed wind capacity in the United States. Demand for wind energy all over the world is also growing. In their annual market report, the Global Wind Energy Council (GWEC, 2010) reported the global status of wind power (see Figure 1.1). The demand for wind power across the world is increasing at a tremendously high rate.

Due to this increasing demand for wind energy, extensive research is being done to support wind turbine design. This is especially true in the area of wind turbine aerodynamics, an understanding of which is required to ensure safe and efficient extraction of energy from wind by wind turbines. Wind turbines capture the kinetic energy in the wind to generate electrical power. Energy extraction from the approaching wind is converted into electricity occurs in two stages. The first stage is extraction of power from the incoming wind at the rotor plane to produce shaft power. This stage is directly related to the aerodynamics of the wind turbine blades. To understand the aerodynamics of wind turbines, wind tunnel testing of wind turbine models is

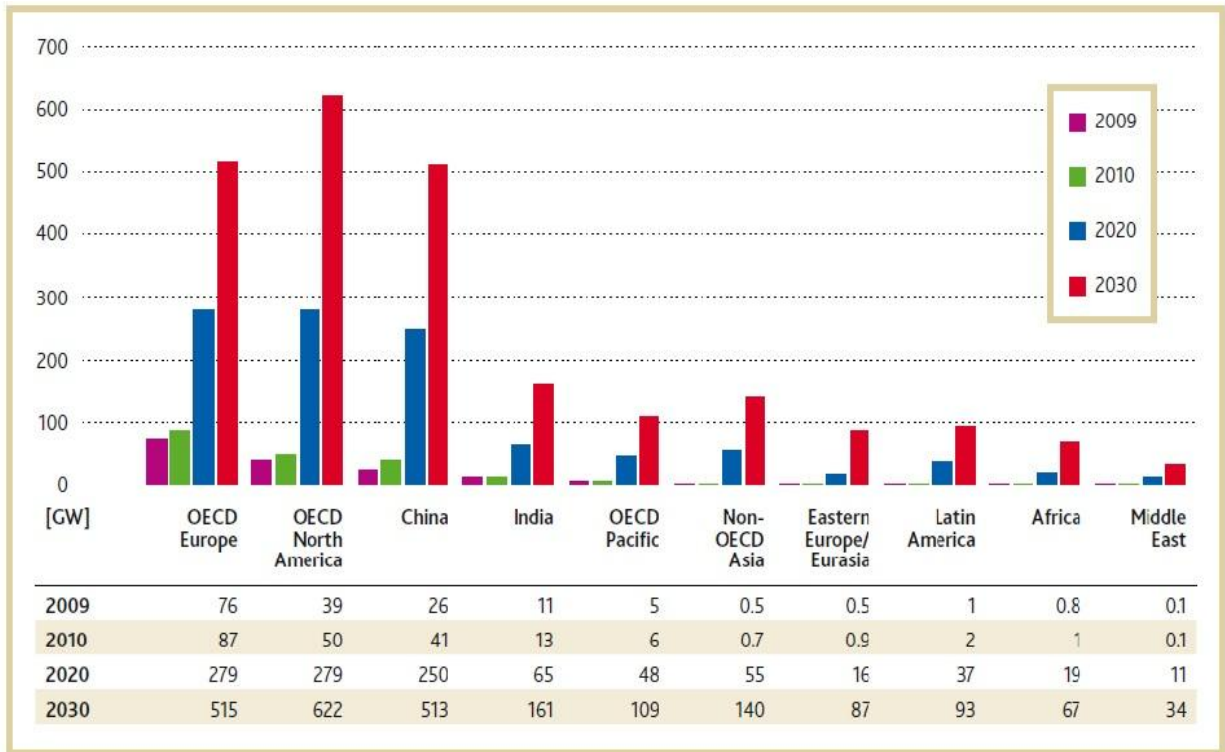


**Figure 1.1: Global status of wind power. (Reprinted with permission from GWEC Annual Market Report, 2010)**

very important. The second stage is related to the conversion of mechanical power into electrical power.

### **1.1 Flow around a Wind Turbine Rotor**

When wind approaches the rotor plane of a wind turbine, there is a decrease in the streamwise component of the velocity before the air passes through the rotor plane. To maintain a constant mass flow rate, this leads to an increase in the flow area as air deflects around the rotor plane. Figure 1.2 shows a schematic of the rotor plane of a wind turbine and flow around it based on simple one-dimensional analysis. The amount by which the freestream velocity reduces is the axial velocity deficit. The fraction by which the axial component of velocity is reduced is

known as the axial induction factor ( $a$ ). If the freestream velocity is  $U_\infty$  and the axial velocity at the rotor plane is  $U_1$ , then the axial induction factor is,

$$a = \frac{U_\infty - U_1}{U_\infty}. \quad (1.1)$$

The axial velocity at the rotor plane can be expressed in terms of the axial induction factor ( $a$ ) as

$$U_1 = U_\infty (1-a). \quad (1.2)$$

After passing through the rotor plane, the axial component of the velocity reduces further and in this very simple one-dimensional analysis becomes  $U_\infty (1-2a)$  far downstream. When the flow passes through the rotor plane, there is a pressure drop across the rotor plane. The slowing down of the flow downstream of the rotor plane corresponds to the pressure recovery back to atmospheric pressure. In this idealization, half of the flow induction occurs before the rotor plane and half of the induction occurs after the rotor. In the simple 1-D analysis (Figure 1.2), flow induction is shown only in one direction. In reality, this induction occurs also in the radial direction and in the tangential direction.

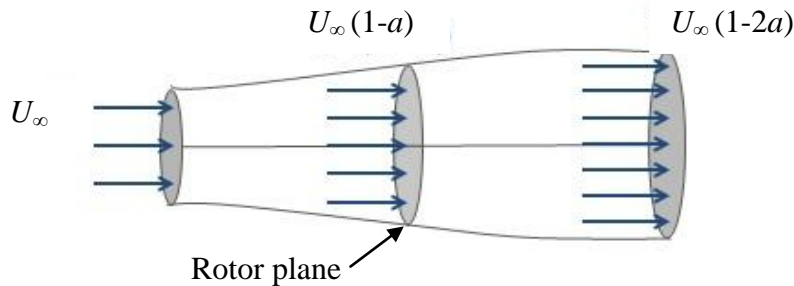


**Figure 1.2: 1-D analysis of the flow passing through the rotor plane of a wind turbine.**

Another induction factor used to describe the wind turbine flow field is the tangential induction factor ( $a'$ ) which is due to rotation of the flow in the wake. This is expressed as

$$a' = \frac{\omega}{2\Omega}, \quad (1.3)$$

where  $\Omega$  is the angular speed of the rotor and  $\omega$  is the angular velocity at which the wake rotates. High values of  $a'$  correspond to lower power production because of the kinetic energy associated with wake rotation.

The axial induction factor ( $a$ ) at the rotor plane is closely related to the power extracted by the wind turbine. If the wind approaching the turbine is completely brought to rest ( $a = 1$ ) by the turbine blades, no power will be extracted by the wind turbine since there will be no flow through the rotor plane. Also, if there is no change in the velocity of the wind passing through the turbine blades ( $a = 0$ ) no power will be extracted since the kinetic energy of the air before and after the turbine blades remains unchanged. The power ( $\dot{W}$ ) extracted by the wind turbine is related to the axial induction factor ( $a$ ) by

$$\dot{W} = \frac{1}{2} \rho A U_\infty^3 4a(1-a) \quad (1.4)$$

where,  $\rho$  is the air density,  $A$  is the rotor area,  $U_\infty$  is the freestream velocity and  $a$  is the axial induction factor at the rotor plane. The amount of power in the approaching wind is,

$$\dot{W}_{wind} = \frac{1}{2} \rho A U_\infty^3. \quad (1.5)$$

The fraction of power in the approaching wind that is extracted at the rotor plane is known as power coefficient ( $C_p$ ) and is defined as,

$$C_p = \frac{\dot{W}}{\dot{W}_{wind}}. \quad (1.6)$$

Another important parameter used to characterize wind turbine operating characteristics is the tip-speed ratio ( $\lambda$ ). It is defined as the ratio of the blade tip velocity to the freestream velocity and is expressed as

$$\lambda = \frac{\Omega R}{U_\infty}, \quad (1.7)$$

where  $\Omega$  is the rotational speed of the rotor,  $R$  is the radius of the rotor and  $U_\infty$  is the freestream velocity. The curve of power coefficient ( $C_p$ ) as a function of tip-speed ratio ( $\lambda$ ) is the characteristic curve for a wind turbine.

### **1.2 Blade Element Momentum (BEM) Method**

The Blade Element Momentum (BEM) method is the main design tool for the aerodynamic analysis of wind turbines. The BEM method is basically composed of two theories: Blade Element theory and Momentum theory. As inputs this method requires geometrical features of the wind turbine such as lift and drag coefficient ( $C_L$  and  $C_D$ ) data of the aerofoil sections as a function of angle of attack ( $\alpha$ ), spanwise pitch angle ( $\phi$ ) distribution, spanwise distribution of chord ( $c$ ), the number of blades ( $n$ ), tilt and blade coning and operating conditions such as wind speed ( $U_\infty$ ) and direction, turbulence, wind shear, density ( $\rho$ ) and rotational speed ( $\Omega$ ). From these inputs the BEM method calculates power ( $\dot{W}$ ), torque ( $T$ ) and the distribution of both the induction factors ( $a$  and  $a'$ ) as outputs.

The BEM method begins by discretizing the rotor plane into a number of radial segments. By applying linear and angular momentum theory, the BEM method calculates the thrust force

(force perpendicular to the rotor plane) and the torque around the rotor axis for each segment. The Blade Element theory portion calculates the thrust force and driving force acting on the blade elements from the lift and drag coefficient data. The lift and drag coefficient data are provided from experiments as a function of the angle of attack ( $\alpha$ ). To find angle of attack, the values of the induction factors are required. The forces and torques, obtained from these two theories contain the axial induction factor ( $a$ ) and tangential induction factor ( $a'$ ). The BEM method equalizes the thrust forces and driving torques obtained from the two theories by iterating the axial induction factor ( $a$ ) and tangential induction factor ( $a'$ ) distributions along the span of the blades. Once the final values of axial induction factor ( $a$ ) and tangential induction factor ( $a'$ ) distributions are found, the thrust force and torque on each blade element can be calculated. By integrating the thrust force and torque acting on the blade elements along the span of the blades, the total thrust force and torque is calculated. Torque and power coefficients can then be found. To obtain realistic values of these parameters, the BEM method also employs several correction factors like a tip-loss correction factor and correction factors for heavily loaded turbines.

Due to its capability to do calculations very fast, the BEM method is the most widely used aerodynamic model for the analysis of wind turbines (Hansen and Madsen, 2011). However, it strongly relies on good experimental aerofoil data and several empirical correction factors.

### 1.3 Motivation

With increasing demand for wind energy, the necessity for assuring the safe, efficient, economic and reliable operation of wind turbines is also increasing. Much research has been carrying out for the last few decades to improve the performance of wind turbines. Understanding the aerodynamics of wind turbines is the key factor to determining the power extracted by the wind turbine. To completely understand the aerodynamics of wind turbines and the complicated flow behavior around the rotor plane, testing of full-scale models and scaled-down models have become important areas of study in experimental fluid dynamics. Full-scale tests (Schreck, 2002 & Magnusson and Smedman, 1999) are always desirable since they give the most realistic results. However, due to the high cost of full-scale experiments, they are not always possible. Though the datasets of model wind turbine experiments suffer due to scaling effects, they are more feasible and less challenging than full-scale experiments. Apart from blockage and scaling effects, model wind turbine experiments in a wind tunnel can give excellent information about the aerodynamics and performance of full-scale wind turbines. They also have the flexibility to perform experiments in a variety of flow conditions. Moreover, the development of experimental apparatus and methodologies with less uncertainty has made scaled-down model wind turbine datasets more reliable.

In addition to different experimental methodologies, computational techniques have been developing to predict the performances of wind turbines. These can be found in Coton *et al.* (2007), Vermeer and Van Bussel (1990), Gupta and Leishman (2005), Madsen *et al.* (2007), Vries (1979), Du and Selig (2000), Lanzafame and Messina (2007). The advantages of computational methods over experimental techniques are lower costs and less time required to obtain results. However, when compared to experimental results, the agreement is poor most of

the time (Schreck, (2002), Ebert and Wood (1997), Whale *et al.* (2000b), Abe and Ohya(2004), Gupta and Leishman (2005)). Computational predictions of wind turbine performance might be good at some operating conditions, but fail at other operating conditions. This indicates that modifications to computational models are still required. Most computational models strongly rely on experiments to incorporate corrections so that good agreement with the experimental results can be obtained over a wide range of operating conditions. That is why experimental datasets with different wind turbine designs and at different operating conditions are needed. The basis of most commercial design codes is the Blade Element Momentum method (BEM) (Section 1.2). Though very fast in calculation, the dependency on reliable aerofoil datasets has made the predictions by BEM questionable. At one of the calculation stages, BEM iterates the value of the axial induction factor ( $a$ ) and tangential induction factor ( $a'$ ) at the rotor plane. Validation of these induction factors with experimental data at various operating conditions is needed to assess BEM predictions. The experimental datasets are used not only for this validation purpose, but also serve as an excellent database to code designers to make necessary correlations where numerical and analytical expressions get very complicated.

Particle Image Velocimetry (PIV) is a whole field velocity measurement technique which obtains a large number of measurements within a short period of time compared to other experimental techniques. In order to validate the performance of the BEM method, Schenstead (2012) designed a model horizontal axis wind turbine and took PIV measurements upstream of the rotor plane. Azimuthally-averaged radial distributions of axial induction factor ( $a$ ) at the rotor plane obtained from PIV were compared to the radial distribution of axial induction factor ( $a$ ) predicted by the BEM method. His datasets were taken only at three operating conditions. Schenstead's results at the rotor plane were obtained by extrapolating the results obtained on the

upstream side to the rotor plane. The BEM method predicts the radial distribution of axial induction factor ( $a$ ) at the rotor plane. However, it is very difficult to take PIV measurements at the rotor plane as the presence of the blades provides obstacles to the camera to take images at the rotor plane and the reflections from the blades hamper the quality of the PIV images. Taking PIV measurements on both the upstream and downstream sides and finding the radial distribution of axial induction factor ( $a$ ) at the rotor plane by interpolating the results between the sides would be a better representation of the axial induction factor ( $a$ ) at the rotor plane than the results based only on the upstream side.

This thesis project describes the PIV measurements on both upstream and downstream sides of the rotor plane of a model horizontal axis wind turbine at six different operating conditions (five tip-speed ratios) and 15 azimuthal positions (angular positions of wind turbine blades) of the blades to find the radial distribution of axial induction factor ( $a$ ) at the rotor plane. This thesis also describes the comparison of azimuthally averaged and axially interpolated axial induction factor ( $a$ ) obtained from the PIV experiments to those obtained from the BEM method in order to assess the performance of the BEM method. The results are useful not only for code validation but also will serve as an excellent database for code designers to improve their design codes.

## **1.4 Objectives**

The general objective of this research project is to investigate the flow around the rotor plane of a model wind turbine at different freestream velocities and different rotor speeds. The results will be presented in terms of the axial induction factor ( $a$ ). The research project has the following specific objectives:

1. To take PIV measurements around a model wind turbine in the wind tunnel.
2. To measure axial induction factor ( $a$ ) as a function of radial position ( $r$ ), axial position ( $x$ ) and azimuthal position ( $\theta$ ) with respect to the wind turbine blades.
3. To interpolate the axial induction factor ( $a$ ) in the axial direction ( $x$ ) and average it in the azimuthal direction ( $\theta$ ) to yield axial induction factor ( $a$ ) as a function of only the radial position ( $r$ ) at the rotor plane.
4. To compare the results obtained from the experiment to the results obtained from the Blade Element Momentum method.

## **1.5 Organization of the Thesis**

Chapter 2 contains a comprehensive review of previous studies of wind turbine aerodynamics, model-scale and full-scale experiments along with the computational methods to investigate wind turbine flow phenomena. Chapter 3 briefly describes the model HAWT design, experimental setup, PIV technique and other instrumentation used. Chapter 4 demonstrates the preliminary testing of the model HAWT, trigger delay calibration method, PIV image calibration method and details about how the experimental datasets were taken. Chapter 5 contains the

experimental and BEM results. This chapter also compares the experimental results to the BEM results. Chapter 6 contains concluding remarks and recommendations.

# Chapter 2: Literature Review

## 2.1 Introduction

Converting the kinetic energy in the wind into electrical energy by means of wind turbines occurs in two stages. The first step is to extract energy from the incoming wind into shaft work at the rotor. The second step is to convert the shaft work into electricity in a generator. Extraction of wind energy at the rotor plane is dependent on the aerodynamics of the turbine blades. Many analytical, experimental and computational studies have been carried out to completely understand the underlying physics of power extraction at the rotor plane and to investigate the flow near the rotor plane of a wind turbine. These studies have contributed greatly to improving the performance of wind turbines. With the development of experimental techniques, researchers in fluid dynamics have been extremely motivated to perform experiments with scale models, full-scale machines, or even in the field. Considering the costs and time constraints associated with experimental investigations, computational studies to unveil the complex flow behavior and predict the performance of wind turbines at different operating conditions have also been developed.

## 2.2 Wake Velocity Measurements

The wake can be divided into two regions: the near-wake region and the far-wake region. The near-wake region is the region immediately behind the rotor and here the presence of the turbine blades is most prominent and the flow field is three dimensional. The extent of the near-wake region can be approximated as one diameter downstream from the rotor plane (Vermeer *et*

*al.*, 2003). The presence of tip vortices is one of the most important characteristics of the near-wake region since they not only influence the flow to a great extent but also cause vibration and noise (Massouh & Dobrev, 2007). The far-wake is important to the mutual dependence of wind turbines in a wind farm and the issue of positioning them to ensure maximum efficiency in wind farm operations (Vermeer *et al.*, 2003). Vermeer *et al.* (2003) contains a review of experimental and computational studies performed in the near-wake and far-wake region.

In order to investigate the formation and development of the three-dimensional near-wake velocity field, tip vortices properties and diffusion mechanism of hub vortices, Ebert and Wood (1997, 1999, 2001) conducted an experiment with a model wind turbine in a wind tunnel. The model wind turbine was two-bladed with a rotor diameter of 250 mm. The blade cross-section was a NACA 4418 aerofoil with constant chord and constant twist along the span. Radial velocity distributions of the flow field behind the rotor plane were measured at six different axial distances from the rotor plane for three different tip-speed ratios by X-wire anemometry. To void the influence of wind tunnel blockage, measurements were restricted within a two-chord distance. The authors found the effect of the circumferential vorticity in the blade boundary layers which was responsible for the formation of downstream axial vorticity. The phase-locked average velocity fields obtained from this experiment were compared to vortex panel code predictions and better agreement was found at higher tip-speed ratios. They also observed notable velocity deficits downstream of the rotor plane and the amount of deficit increased as the axial distance increased. This is due to the expansion of the wake as it travels downstream. Their experimental results also revealed the presence of an increasing amount of angular momentum in the tip vortices as the tip-speed ratio increased. This residual angular momentum in the tip vortices actually has detrimental effects on the output power available from wind turbines. This

strongly suggests the necessity of incorporating the tip vortices structure in computational models. However, this study was performed in controlled conditions considering uniform inflow conditions inside a wind tunnel and ignoring the effects of non-uniformity due to boundary layers in the incoming flow on the wake profiles.

In reality, wind turbines operate in atmospheric turbulent boundary layers which have an influence on the wake. To study the effects of such boundary layers, Chamorro and Porte-agel (2009) carried out an experiment with a model three-bladed wind turbine (GWS/EP-6030 x 3) placing it in two types of boundary layers. The model wind turbine had a rotor diameter of 150 mm. They performed hot-wire measurements to determine the cross-sectional distribution of mean velocity, velocity deficit and turbulence intensity up to 15 diameters downstream of the rotor plane. It was found that even though the cross-sectional distribution of velocity deficit was axi symmetric, the velocity profile was not. This was due to the presence of non-uniformity in the incoming boundary layer. It was also found that the velocity deficit decreased with axial distance but was not negligible even at a distance of 15 rotor diameters downstream.

Formation, development and properties of the near wake were investigated experimentally by hot-wire anemometry over different tip-speed ratios up to a distance of four chords downstream of the rotor plane by Dan-mei and Zhao-hui (2009). The experiment was performed at model scale with a three-bladed 500 mm diameter model wind turbine. The cross section was an NREL S809 aerofoil with adjustable pitch. They found the distribution of circumferentially averaged velocity deficit and mean velocity. In the distribution of mean velocity, the decay and expansion of the three-dimensional wake were clearly observed.

There are many other studies with model wind turbines in wind tunnels focused on the flow behavior in the wake region to investigate the tip vortex properties and their influence on output power from the wind turbines. These can be found in Massouh and Dovrev (2007), Zhang *et al.* (2012), Snel *et al.* (2007), Whale *et al.* (1996) and Whale *et al.* (2000b).

All the studies mentioned above on wake and velocity fields were conducted on scaled-down models. Magnusson and Smedman (1999) investigated the wake of a full-scale wind turbine and compared the results with other full-scale and wind tunnel simulation results. The full-scale wind turbine was a three-bladed 180 Danwind turbine with rotor diameter of 23 m. The authors reported that for larger values of the torque coefficients the value of the velocity deficit gets larger.

### ***2.3 Quantitative Flow Visualization Techniques***

Quantitative flow visualization techniques have been very popular in the area of experimental fluid dynamics due to their nonintrusive characteristic and the fact that very rich flow information can be obtained. When applied to wind turbine aerodynamic research, this can give qualitative information very near to the rotor plane or even at the rotor plane to investigate the influence of the rotor on the flow field around it (Vermeer *et al.*, 2003). That is why Particle Image Velocimetry (PIV) and a few other quantitative visualization techniques have been used in wind turbine research.

As described by Whale *et al.* (1996), Infield *et al.* (1990) is one of the pioneers of extracting quantitative information from applying PIV to wind turbine aerodynamics. Facing difficulties to theoretically model the complex behavior of the flow around wind turbines,

especially at yawed conditions, they showed that it was possible to obtain realistic flow information by means of experimental techniques. To obtain the detailed profiles of the bound circulation and tip vortex, the authors conducted a wind tunnel test of a 0.9 m diameter model wind turbine at normal and yawed conditions. To capture the velocity fields around the rotor plane PIV was used. They successfully identified the application of PIV as a tool for measuring velocities around wind turbine models and later made full-scale measurements with a 17 m diameter wind turbine.

Grant *et al.* (1991) extended this work and contributed in acquiring more quantitative information about the circulation around a single blade and in the extended flow regions behind the rotor plane. They also showed the application of PIV in characterizing the trailing edge vortices. Flow around a full-size three-bladed Marcel 0.9 m diameter commercial wind turbine with untwisted and tapered blades was investigated. The blade sections consisted of NACA 4613 at the tip which changes to NACA 3712 in the middle section and NACA 4611 at the root. This experiment provided an excellent demonstration on how PIV can be applied both behind the rotor plane and around a blade. They also discussed the data processing techniques used to obtain velocity fields. From the results, the authors were very optimistic in further investigation of circulation along the blades for a full-scale wind turbine using the PIV technique. With the same model wind turbine, Grant and Parkin (2000) conducted PIV measurements at different yaw and azimuthal angles to observe the velocity field of the trailing edge vortices. They found the variation of circulation shed as a function of both yaw angles and azimuthal angles. The results demonstrate the necessity of wind turbine experiments at different operating conditions in order to improve the design.

Whale *et al.* (1996) took PIV measurements downstream of a model horizontal axis wind turbine. A three-bladed model horizontal axis wind turbine (Vestas WM 19s) with a NACA 632xx aerofoil was used in the experiment. The blades had variable twist, chord and thickness distributions along the span. Their measurements were compared to available experimental data sets obtained from two full-scale wind turbines. Comparisons were made of mean velocities at five different tip-speed ratios. The wake velocity deficits of model-scale and full-scale measurements had significant differences. The authors suggested that these differences were due to scaling effects, blockage effects and uncertainties associated with the full-scale experiment. This experiment provided a good opportunity to assess the PIV measurements in a scaled down model and their relationship to full-scale measurements. Though there were no clear conclusions suggested by the authors, it clearly demonstrated the potential of PIV as a velocimetry technique to be used in wind turbine research.

There are other experiments that used PIV as the flow measurement technique to explore the vortex wake (Massouh and Dobrev, 2007) and structure (Whale *et al.*, 2000b), flow structure behind the rotor plane (Zhang *et al.*, 2012), analyzing flow fields in both upstream and downstream side (Snel *et al.*, 2007 and Medici *et al.*, 2009) and measuring performance of model wind turbines (Shimizu and Kamada, 2001). In these studies PIV was successfully applied as a flow measurement technique.

#### ***2.4 Global Properties and Comparison with Numerical Models***

In order to provide data sets for code validation, in addition to the flow field information, many studies focused on the power coefficients, torque coefficients, axial force coefficients and

other global properties of the turbine rotor. These studies also helped to improve the design of the rotor for enhancing maximum power output and ensuring safe operation during unsteady conditions. Shimizu and Kamada (2001) developed a passive flap mechanism which was able to control excessive power to ensure safe operation during abnormal operating conditions. The model was a three-bladed model HAWT of 1.4 m diameter with a tapered and twisted NACA 4415 cross section. The pitching mechanism of the blades was found more effective than a flapping mechanism to reduce the excessive power. Taking velocity measurements with two-dimensional Laser Doppler Velocimetry (LDV) on both the sides of the rotor plane and applying phase-locked average technique at different azimuthal positions, the study determined that the velocity downstream of the rotor tip was very close to half of the freestream velocity. This is in a very good agreement with the simple one-dimensional momentum theory.

The performance of a three-bladed NREL s826 aerofoil section model wind turbine of diameter 0.9 m was investigated by Krogstad *et al.* (2010) to validate the performance of a commercially-available Reynolds-averaged Navier-Stokes solver (Fluent). The calculations were carried out using fully turbulent  $k-\omega$  SST and  $k-\varepsilon$  RNG turbulence models. The model-scale experimental results of power prediction agreed very well with the results obtained from the computational model. At the design tip-speed ratio, the difference in predicted power was within 2%. However, the computational model overestimated the power coefficient value at higher tip-speed ratios.

Abe and Ohya (2005) conducted numerical and experimental investigations behind a model wind turbine and found a value of power coefficient greater than the Betz limit. They modified the turbine using a diffuser with a large flange to accelerate the incoming flow. With the same model wind turbine, Toshimitshu *et al.* (2008) carried out PIV measurements behind

the wind turbine model and showed that the possible reason for the inflow acceleration was the presence of strong separation vortices behind the flange creating a very low pressure region. The experimental results of Abe and Ohya (2005) were compared to a bare wind turbine and a Navier-Stokes solver with non-linear eddy viscosity modeling, advanced closure approximation being considered within it (Abe and Ohya, 2004). Hot-wire measurements of velocity fields were taken and it was seen that power coefficient for the augmented design was four times higher than that of a bare wind turbine. For the tip-speed ratios where there was no separation on the blade surface (at moderate and high tip speed ratios), the prediction of the computational model was found better matched with the experimental results.

Medici *et al.* (2009) showed that in addition to the wake flow characteristics, the approach flow has a significant effect on the power production from wind turbines. This study gave some new information about the incoming flow and its effect under both normal and yawed conditions. They used a non-twisted three-bladed model wind turbine with a Gottingen 417A aerofoil section and a 0.18 m diameter. Hot-wire anemometry and PIV were used to capture the tangential, radial and axial components of upstream velocity fields at different yaw angles of the rotor. Though minimal attention has been given to the upstream flow in the literature, the authors showed that even at a distance of three rotor diameters upstream, the flow field is influenced by the presence of the rotor and the flow field is three-dimensional. It was suggested that it is important to consider these upstream flow characteristics in the performance and power prediction calculations.

## ***2.5 Computational Methods and their Modifications***

Considering the time and cost of experimental studies, computational and numerical methods are developing. The Blade Element Momentum (BEM) method, prescribed wake model, free wake model, actuator disc model (AD), actuator line model (AL) and Navier-Stokes codes are some of the models for wind turbine flow predictions (Snel *et al.*, 2007). In addition to these there are other models for characterizing the wake, stall flow and modeling the performance at different operating conditions. These can be found in Du and Selig (1998), Madsen and Rasmussen (2004), Johansen *et al.* (2009), Sorensen and Kuik *et al.* (2009), Masson *et al.* (2001), Whale *et al.* (2000a) and Shen *et al.* (2009). Many studies have been done to improve the accuracy and reduce the uncertainties of these computational models so that wind turbine flow phenomena can be predicted well over a large range of operating conditions.

The basis of most commercially available wind turbine design codes is the Blade Element Momentum (BEM) method due its simplicity and speed (Hansen and Madsen, 2011). However, there are lots of assumptions incorporated into the BEM method which make the prediction unrealistic for a variety of operating conditions (Vries, 1979). This has motivated development of other models and comparisons with BEM methods. Gupta and Leishman (2005) showed a comparison of the BEM method with the Finite Volume Method (FVM). At low tip-speed ratios there was good agreement between the methods for thrust and power prediction. However, at higher tip-speed ratios, for high wake induction near the tip, the BEM method failed to predict power and torque coefficients where the FVM was able to predict these phenomena at almost all operating conditions. At yawed flow conditions, the FVM's flexibility was higher than the BEM method. The results indicated some limitations of BEM for a wide range of operating conditions.

Madsen *et al.* (2007) showed a comparison of the BEM method to the Actuator Disc (AD) model and proposed some modifications to the existing BEM model in order to enhance accuracy. They figured out two discrepancies in the BEM method; overestimation of induction in the inner part as the pressure variation was neglected in the wake from wake rotation and underestimation of induction on the outer part. The authors suggested incorporation of an axial velocity component which is induced due to the pressure variation in the wake with the velocity at the disc. The second discrepancy was taken care of by incorporating a mass flow factor to the rotor mass flow, as it was found that underestimation of induction at the tip occurs mainly due to decreased inflow near the tip resulting from wake expansion. After these modifications were done, the results obtained from both the methods showed a close match.

Du and Selig (2000) suggested a modification to the BEM method considering the effect of rotation at the blade boundary on the delay of separation. This, in turn, affects the lift and drag. They investigated these effects by a 3D incompressible, steady, momentum integral boundary layer equation and suggested to add a complementary term in the calculation of the lift and drag coefficients.

The “turbulent wind mill state” is a condition where wind turbines do not normally operate. This state is considered to be a high induction state. For completeness, however, a code should consider these states (Buhl, 2005). The induction calculation method in this state proposed by Glauert fails as it does not consider tip and hub losses and has a discontinuity in the relationship of thrust coefficient and axial induction factor ( $a$ ). Buhl (2005) proposed a new method of calculation which is applicable for the turbulent wind mill state. He derived a new equation for calculating the axial induction factor ( $a$ ) which removes the discontinuities in

previous calculations and found a great match with experimental datasets. This method was claimed to be the best for calculations in the turbulent wind mill state.

In BEM calculations, it is very challenging to correctly evaluate the induction factors (axial induction factor and tangential induction factor). Lanzafame and Messina (2007) applied the BEM method by incorporating a new expression for tangential induction factor ( $a'$ ) and using the axial induction factor ( $a$ ) expression from Buhl (2005) and compared his results with NREL's Unsteady Aerodynamics Experimental results (Schreck, 2002). In this study the aerodynamic coefficients were obtained from a best-fit curve available in the literature. Though they found good agreement with experimental results, the authors lacked extensive experimental datasets.

Vries (1979) lists the assumptions made in BEM calculations and the areas where those assumptions affect the calculations. He concluded that the accuracy of the tip correction factor in BEM greatly controls the overall accuracy of the results. He also felt the need for more experimental datasets to correct the assumptions and produce new correlations.

After the National Renewable Energy Laboratory's Unsteady Aerodynamic Experiment (NREL's UAE) (Schreck, 2002) and blind comparisons of their datasets with several computational methods, it was revealed that further improvements of the computational models are needed. Coton *et al.* (2002) lists some of the major steps undertaken after NREL's Unsteady Aerodynamic Experiment. They also tested the prescribed wake model developed in Glasgow University against the NREL's experimental datasets. It was found that including a dynamic wake model enhances predictions even at high yaw angles. The authors emphasized the

importance of selection of input parameters, especially blade aerofoil data, to obtain improved predictions from the models.

Though there are new methods being invented and old methods being modified, the need for experimental datasets can never be denied for the validation of those methods. Experimental datasets should also be provided to help the code designers identify the regions of the flow phenomena where more calculation efforts are needed.

## ***2.6 Experiments and Comparison with Numerical Analysis***

To check the validity of predictions from numerical and computational analysis, there have been lots of experiments solely dedicated to this validation purpose. The experiments were done either in the wake (near or far) or on the upstream side and both with full-scale and scaled-down models.

Vermeer and Van Bussel (1990) took three-dimensional velocity measurements by Hot Wire Anemometry (HWA) in the near wake of a model wind turbine. It was a two-bladed model HAWT with a NACA 0012 aerofoil section and a diameter of 1.2 m. The model HAWT blade had a constant chord of 0.08 m and variable twist along the span. The experimental results were used to validate two computer codes; PREDICHAT and VIAX. The basis of the codes is the acceleration potential approach. There was a very good match of experimental data with predicted data in the axial velocity distributions except for the regions of quickly changing flow. Dissimilarities were also found near the root of the blades when maximum blade load was applied. These dissimilarities in the predictions were attributed to the wake circulation.

For validation of the inviscid free-wake code, Rotor Vortex Lattice Method (ROVLM), developed in the University of Stuttgart, Whale *et al.* (2000b) measured the velocity and vorticity

of the near wake of a two-bladed flat-plate model wind turbine of diameter 175 mm. The velocity field behind the rotor plane was captured by PIV and was compared with the ROVLM results. The ROVLM results agreed with the experimental results qualitatively as it predicted the shape of the wake boundary and the contraction of the wake in the downstream side very well. However, the code failed to predict the influences of Reynolds number and failed to characterize the stalled flow behavior for the blade inboard sections. These led to further modification of the ROVLM code to give realistic predictions.

Just as the numerical codes suffer significantly due to the need for validation data, the experimental results have uncertainties due to inaccuracies of the instruments. Reliable experimental datasets having less uncertainty and scaling effects are always desirable. Being motivated by this, the National Renewable Energy Laboratory (NREL) conducted tests with a full-scale model wind turbine in the NASA Ames wind tunnel (Schreck, 2002). The purpose of this full-scale test was to provide extremely reliable data with less experimental uncertainty and without any significant scaling effect. A 2-bladed wind turbine of rotor diameter 10.1 m was tested at 14 different rotor alignment conditions. The twisted and tapered blades had a uniform cross section of the s809 aerofoil design. The large cross section of the wind tunnel ensured purity of measured data in terms of scaling effects. Inflow velocities, wake velocities and several global properties including normal force coefficient, moment coefficient and torque coefficient were measured for different freestream conditions from 5 m/s to 25 m/s. A small portion of these values were provided to the invited code developers from different countries and a blind comparison of their codes was performed. Among all the codes there were BEM codes and Navier-Stokes codes. This comparison provided an excellent opportunity to comprehend the recent state of the codes and the lack of reliability in prediction. The maximum error was found

for the normal force coefficient and it was as large as 50% in some operating conditions. At lower speeds and lower angles of attack when the aerodynamic analysis is comparatively less complicated, the errors in predictions were at least 15%. However, this experiment provided a large, extremely reliable and realistic dataset of flow fields around a wind turbine for the validation of computational methods under a large variety of operating conditions. There were several steps undertaken by the code developers after this blind comparison. These can be found in Coton *et al.* (2002).

Considering the lack of datasets for the validation of computational models researchers have focused on creating reliable datasets with different model wind turbines at a large variety of flow conditions. The MEXICO (Model Experiments in Controlled Conditions) project conducted by Snel *et al.* (2007) is one of those projects. In order to provide datasets for validation of extended BEM and CFD models, they created a dataset for load and detailed aerodynamics measurements. A three-bladed model HAWT with twisted and tapered blades was tested at a large variety of operating conditions, rotor geometry and inflow conditions. The blade cross section was DU 91-W2-250 at the root, RIS $\phi$  A1-21 at the middle and NACA 64-418 at the tip. Flow fields on the upstream and downstream side were captured by PIV for different azimuthal positions of the blades and at different yaw angles of the rotor. The datasets of the NREL Unsteady Aerodynamics Experiment (Schreck, 2002) was limited only to blade pressure distributions and blade load whereas for the MEXICO project (Snel *et al.*, 2007) the flow field at the rotor plane was measured. The MEXICO project can be considered as a complementary project to the NREL UAE NASA Ames experiment. For the BEM method, free-wake models and other CFD calculations, information about the induction properties are very important. This project provided an opportunity, for the first time, to investigate the development of induction

upstream and downstream of the rotor. For all CFD codes it is important to know the velocity field near the blades and this information was obtained from this experiment. This project also helped improve tip correction models at both normal and yawed conditions.

The MEXICO project and NREL's Unsteady Aerodynamic Experiment were carried out in controlled conditions. In reality, wind turbines operate in a turbulent boundary layer which has an effect on the wake velocity fields. For improved modeling by the codes these effects should be considered. Zhang *et al.* (2012) performed experiments on a model HAWT in a turbulent boundary layer. Wake velocity profiles were captured by stereo PIV in two-dimensional planes. The model was a three-bladed wind turbine with GWS/EP-5030 x 3 and the rotor diameter was 0.13 m. Their intention was to help in making accurate simulations considering the non-uniformity of flow.

Haans *et al.* (2008) conducted an experiment to investigate the near-wake formation and development with a hope to provide datasets for validation of near-wake calculation models. They used a 1.2 m diameter model HAWT consisting of two blades of NACA 0012 section with constant chord but variable pitch. Three-dimensional velocity fields were investigated by hot-wire anemometry at different azimuthal blade positions using phase-locked averaging. The experimental results determined the azimuthally-averaged value of axial induction factor at the rotor plane. Though no measurements were taken at the rotor plane, the value of axial induction factor at the rotor plane was extracted by least square fit to the datasets taken in the downstream side. The authors also reported azimuthal variation of velocity vectors at the rotor plane. The results and datasets of this experiment are particularly useful for BEM method validation and improvement as BEM relies heavily on the values of induction at the rotor plane.

Massouh and Dobrev (2007) captured three-dimensional velocity fields on the downstream side of a model wind turbine at different azimuthal positions by means of PIV and HWA. To capture the radial and axial components, PIV was used and the tangential velocity component was measured by HWA. Their intention was to create a reference for CFD codes for calculations in the three-dimensional wake. The model used in this experiment was a three-bladed Marcel Rutland 503 wind turbine of 500 mm diameter rotor and untwisted, variable-pitch blade with chord distribution along the span. This experiment provided an excellent dataset for induced velocities in both axial and tangential directions which is helpful for code developers. However, the flow fields right at the rotor plane were not measured which would have been very good information for BEM validation.

Table 2.1 contains a summary of the studies that have been reviewed. Some of the key design features of the wind turbine, the purpose of the study, and the areas of investigation are presented in a tabular form.

Table 2.1: Summary of wind turbine aerodynamics studies.

Authors	Year	Wind Turbine Design	Primary Focus	Methodology	Purpose
Chamorro <i>et al.</i>	2009	Number of Blades: 3 AF section: GWS/EP-6030 x 3 Rotor Diameter: 0.150 m	Cross sectional distribution of mean velocity and velocity deficit	HWA	Investigation of turbulence in the wake and the effect of boundary layer flow
Dan-mei and Zhao-hui	2009	Number of Blades: 3 AF section: NREL S809 Rotor Diameter: 0.5 m Features: Adjustable pitch	Near wake and velocity deficit measurements	HWA	Understand the physical features of the flo field
Ebert and Wood	1997 1999 2001	Number of Blades: 2 AF section: NACA 4418 Rotor Diameter: 0.25 m Features: constant chord and twist	Document the development and formation of near wake	X-Wire Anemometry	Comparison with Panel Code predictions
Grant <i>et al.</i>	1991	Number of Blades: 3 AF section: Marlec Rutland Rotor Diameter: 0.91 m Features: Commercial blade	Characterizing the tip vortices and circulation around the blade	PIV	Providing more qualitative information on circulation around blade

Table 2.1: Summary of wind turbine aerodynamics studies (cont.)

Authors	Year	Wind Turbine Design	Primary Focus	Methodology	Purpose
Grant and Parkin	2000	Number of Blades:3 AF section: NACA 4613 at tip, NACA 3712 at mid and NACA 4611 at the root. Rotor Diameter: 0.9 m Features: Untwisted, tapered and constant pitch blades	Velocity field of the trailing edge vortices	PIV	Validate the prediction codes
Haans <i>et al.</i>	2008	Number of Blades: 2 AF section: NACA 0012 Rotor Diameter: 1.2 m Features: Constant chord and variable pitch	Measurements of near wake at normal and yawed conditions	Constant temperature anemometry	Understand the near wake development and provide data for numerical model validation
Krogstad <i>et al.</i>	2010	Number of Blades: 3 AF section: NREL s826 Rotor Diameter: 0.9 m Features: Untwisted and variable chord	Measure performance of the model wind turbine	6-component force balance	Provide data for computational code validation
Magnusson and Smedman	1999	Number of Blades: 3 AF section: Danwind turbines Rotor Diameter: 23 m Features: 4 full scale turbines in farm.	Velocity deficit and torque coefficient	Instrumentation developed in Department of Meteorology in Uppsala. In field measurements	Comparison of full scale measurements and experiments

Table 2.1: Summary of wind turbine aerodynamics studies (cont.)

Authors	Year	Wind Turbine Design	Primary Focus	Methodology	Purpose
Massouh and Dobrev	2007	Number of Blades: 3 AF section: Marcel Rutland 503 Rotor Diameter: 0.5 m Features: Untwisted, Variable Chord, Constant Pitch of 10°	Axial, radial and tangential components of velocity	PIV and HWA	Create database for CFD computations
Medici <i>et al.</i>	2009	Number of Blades: 3 AF section: Gottingen 417A Rotor Diameter: 0.18 m Features: Non-twisted	Measure the flow field in the upstream side	HWA and PIV	Provide flow field information in the upstream side
Schreck	2002	Number of Blades: 2 AF section: s809 Rotor Diameter: 10.1 m Features: Full scale, Twisted and tapered blades	Flow fields at a large variety of operating conditions, torque, moment and normal force coefficients	Five hole pressure probes	Comparison with numerical analysis
Shimizu and Kamada	2001	Number of Blades: 3 AF section: NACA 4415 Rotor Diameter: 1.4 m Features: Tapered and twisted	Velocity field measurements in both upstream and downstream	2-dimensional LDV	Develop a system for controlling power output

Table 2.1: Summary of wind turbine aerodynamics studies (cont.)

Authors	Year	Wind Turbine Design	Primary Focus	Methodology	Purpose
Snel <i>et al.</i>	2007	Number of Blades: 3 AF section: DU 91-W2-250 (root), RIS $\phi$ A1-21 (mid), NACA 64-418 (tip). Rotor Diameter: 4.5 m Features: Twisted and tapered	Flow field mapping around the rotor and in the near wake	PIV	Create database for load and aerodynamics measurements
Vermeer and Van Bussel	1990	Number of Blades: 2 AF section: NACA 0012 Rotor Diameter: 1.2 m Features: Constant chord and variable twist	3 dimensional flow field measurements in the near wake	HWA	Verification for prediction codes PREDICAT and VIAX
Whale <i>et al.</i>	1996	Number of Blades: 3 AF section: NACA 632xx Rotor Diameter: Features: Twist, chord and thickness distribution	Mean velocity in the downstream side	PIV	Assess the applicability of small scale PIV measurements
Whale <i>et al.</i>	2000b	Number of Blades: 2 AF section: Flat plate Rotor Diameter: 0.175 m Features: Untwisted and linear tapered	Wake velocity measurements	PIV	Comparison with Rotor Vortex Lattice Method (ROVLM)
Zhang <i>et al.</i>	2012	Number of Blades: 3 AF section: GWS/EP-5030 x 3 Rotor Diameter: 0.13 m Features: Nearly flat plate	Near wake velocity field	PIV	Understanding mechanism of near wake formation and create database

Although there are many studies in the wake region which provide validation datasets for computational models, there are a very limited number of experiments on the upstream side to investigate the flow behavior. Simple, one-dimensional momentum theory indicates that half of the induction occurs on the upstream side and half occurs on the downstream side. Therefore, the flow on the upstream side also has significant effects on the induction factors at the rotor plane as well as power extracted by the wind turbine. Schenstead (2012) took PIV measurements on the upstream side of a model wind turbine at different azimuthal positions and investigated the axial and azimuthal variation of axial induction factor ( $a$ ). His purpose was to compile a reference dataset for BEM method validation. For validation of the BEM method, it is important to provide the values of axial induction factor at the rotor plane. Schenstead's measurements of axial induction factor ( $a$ ) at the rotor plane were done by extrapolating the values of axial induction factor ( $a$ ) on the upstream side to the rotor plane. It is very challenging to make PIV measurements right at the rotor plane to find axial induction factor ( $a$ ) as a function of radial distance ( $r/R$ ) at the rotor plane. By making PIV measurements also downstream of the rotor plane at the same operating conditions as Schenstead's and by interpolating the results to the rotor plane, an improved representation of the axial induction factor ( $a$ ) at the rotor plane of the model wind turbine can be achieved.

# Chapter 3: Experimental Setup and Instrumentation

## 3.1 Introduction

The experimental setup and instrumentation used in this thesis research will be described in this chapter. The working principles of some of the instruments will also be described.

## 3.2 Wind Tunnel

The low-speed, closed-return wind tunnel available in the Department of Mechanical Engineering at the University of Saskatchewan was used for the experiments. There are two separate test sections in the wind tunnel, a low-speed test section and a high-speed test section. The dimensions of these two sections are shown in Table 3.1.

Figure 3.1 shows a schematic diagram of the wind tunnel used in this experiment. Flow is driven through the test sections and the return passage by a constant-speed, variable-pitch fan. The fan is powered by a 100-hp electric motor. The corners of the wind tunnel are provided with a set of turning vanes to help maintain uniform flow. The flow passes through a pair of fine mesh turbulence reduction screens situated at the entrance of the low-speed test section. The purpose of the turbulence-reduction screens is to reduce the turbulence intensity. After passing through the low-speed test section, the flow passes through a 7:1 contraction and moves into the high-speed test section. The model Horizontal Axis Wind Turbine (HAWT) was mounted in the high-speed test section. The flow then passes through the diffuser, another two set of corner vanes and

Table 3.1: Dimensions of the Wind Tunnel

Sections	Length (m)	Width (m)	Height (m)
Low-speed section	7	2.97	2.4
High-speed section	1.96	1.13	0.91

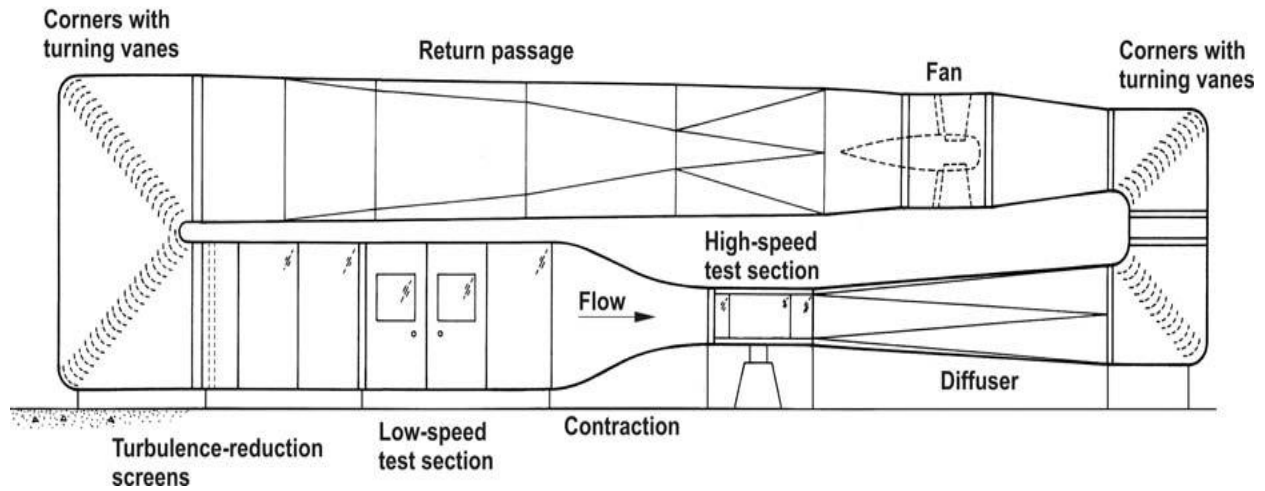


Figure 3.1: Schematic diagram of the wind tunnel (reprinted from Adaramola, 2008)

returns to the fan. The walls of the high-speed test section are made of Plexiglas which provides optical access to the flow around the model. The ceiling of the high-speed test section is provided with a rectangular hole to allow the laser to pass through without any attenuation.

The range of freestream velocities ( $U_\infty$ ) that can be achieved in the high-speed test section of this wind tunnel is  $10 \text{ m/s} \leq U_\infty \leq 50 \text{ m/s}$ . Below 10 m/s the freestream velocity is not steady and velocities beyond 50 m/s cannot be achieved due to the limited capacity of the fan. The longitudinal freestream turbulence intensity is 0.6% and outside of the test-section boundary layers the non-uniformity of the velocity is 0.5% (Adaramola, 2008).

### ***3.3 Freestream Velocity, Temperature and Density Measurement***

A Pitot-static probe (United Sensor, PAC-T-9-T-KL, MINIJACK, 0624) was placed in the high-speed test section of the wind tunnel to measure the freestream velocity. It was located at mid height of the test section and 400 mm downstream from the contraction exit. The probe was extended 90 mm into the flow preventing it from being influenced by the wind tunnel wall boundary layers. The dynamic pressure is measured from the difference between the static and total pressure using a differential pressure transducer (BOC EDWARDS Barocel Pressure Sensor, 590DF 10 H<sub>2</sub>O 0.05% W/THRML PKG). All these data were acquired by a computer with a National Instruments PCI-603 IE 16-bit data acquisition system running LabVIEW software.

Freestream temperature was measured with a T-type thermocouple integrated with the Pitot-static probe. The absolute static pressure was measured by an absolute pressure transducer (Datametrics Barocel Pressure Sensor, 600A-1000T-S13-H21X-4, Range: 1000 TORR). Then, the density ( $\rho$ ) was calculated from the ideal gas equation,

$$\rho = \frac{P_{\infty}}{R_a T_{\infty}}, \quad (3.1)$$

where  $R_a$  is the specific gas constant for air (287 J/(kg . K)),  $T_{\infty}$  (K) is the freestream temperature, and  $P_{\infty}$  (Pa) is the absolute freestream static pressure.

### ***3.4 Model Horizontal Axis Wind Turbine***

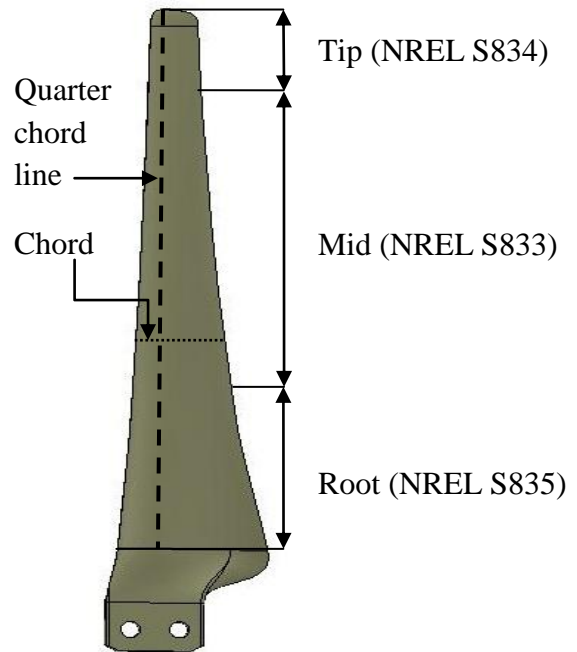
The model horizontal axis wind turbine used in this experiment is designed and built at the University of Saskatchewan by Schenstead (2012). The rotor of the model HAWT has three blades separated by 120°. It was mounted inside the wind tunnel at 0° yaw angle in an upwind

configuration. The rotor was mounted on a magnetic brake which was mounted at the top of the model HAWT tower. To enhance aerodynamic performance the blades are constructed from three different aerofoil sections along their span. The aerofoil sections are NREL's S835, S833 and S834 from the root to the tip respectively (Schenstead, 2012). The radius of the rotor is 25 cm and the radius of the nose cone is 5 cm. The blades also have a variable chord and twist distribution along their span. Figure 3.2 shows a picture of the model HAWT used in this experiment and the blade design.

Figure 3.3 shows a schematic diagram of the model HAWT mounted inside the wind tunnel and establishes the coordinate system used. The axis of rotation of the rotor is chosen as the  $x$  axis and is aligned with the flow direction. The centre of the rotor is the origin of the



(a)



(b)

**Figure 3.2: The model horizontal axis wind turbine; (a) mounted inside the wind tunnel and (b) the blade design (Courtesy of Andrew Schenstead).**

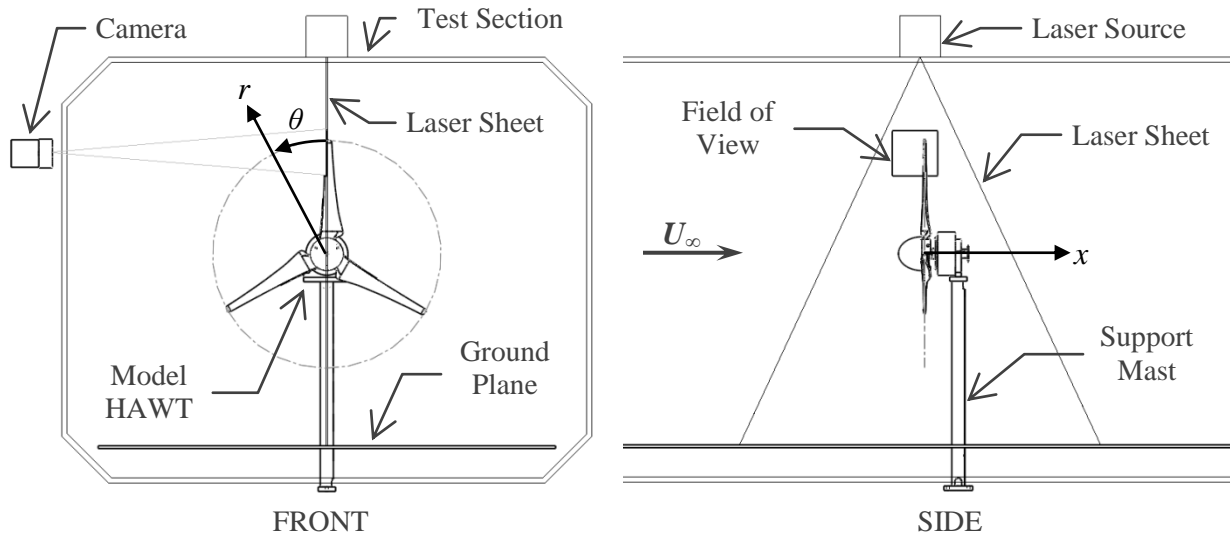


**Figure 3.3: Schematic diagram of the model wind turbine mounted inside the wind tunnel and the coordinate system used. (Courtesy: Andrew Schenstead)**

coordinate system and the radial coordinate ( $r$ ) is measured from that centre. One of the three blades was marked along the quarter chord line and was designated as Blade 1. When this blade is at vertical position, the azimuthal angle ( $\theta$ ) was considered to be  $0^\circ$  and was considered to be positive in the direction of rotation.

### **3.5 Wind Turbine Speed Control Equipment**

The wind turbine rotational speed was controlled by a speed controller and a MAGTROL hysteresis brake. The whole speed control system can be divided into three main components:-

1. MAGTROL hysteresis brake;
2. Encoder wheel;
3. Speed controller,

### 3.5.1 MAGTROL Hysteresis Brake

A MAGTROL hysteresis brake (Magtrol HB-140) was used to provide a reaction torque to the wind turbine rotor shaft. Figure 3.4 shows the rotor and mount assembly of the Magtrol hysteresis brake. Using a reticulated pole structure and a specialty steel rotor/shaft assembly, the hysteresis magnetic effect produces a torque dependent upon the current applied. The wind turbine rotor is directly mounted to the magnetic brake shaft (see Figure 3.5). When the field coil is not energized the rotor rotates freely on its bearings. When a current is applied the air gap between the rotor and pole structure becomes magnetized and provides a braking action on the rotor (drag cup).

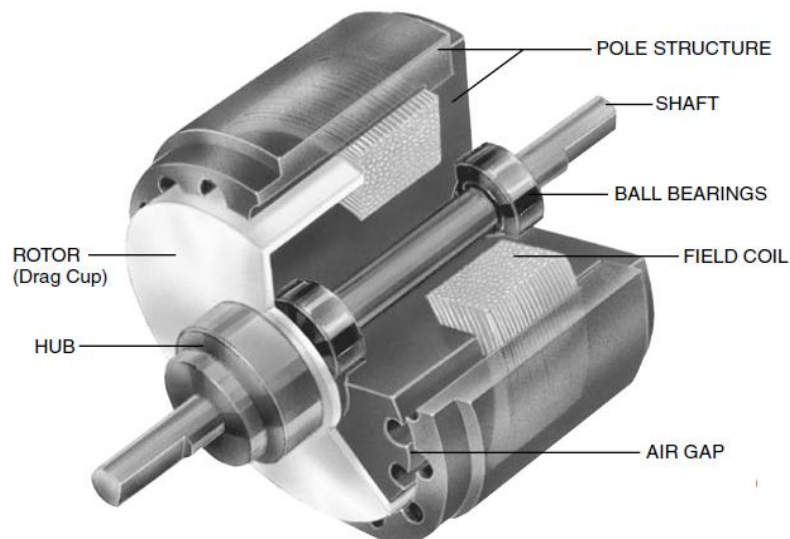


**Figure 3.4: The rotor and mount assembly of the MAGTROL hysteresis brake. (Image source: MAGTROL HB/MHB Data Sheet).**

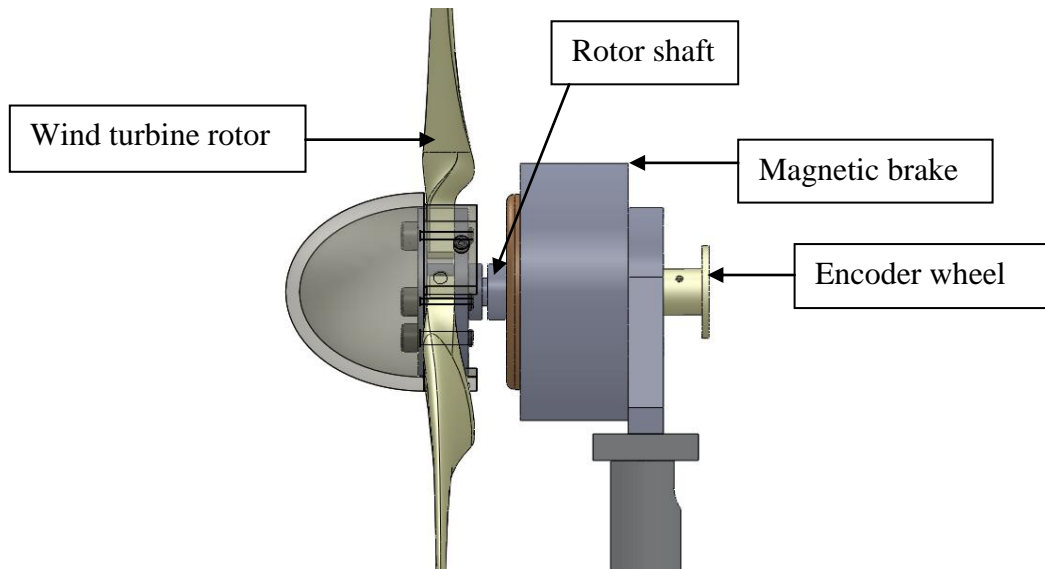


**Figure 3.5: Wind turbine rotor and magnetic brake shaft assembly. (Courtesy: Andrew Schenstead)**

The braking torque is proportional to the current flowing through the field coil. The brake is attached via a pillow block bearing to the model wind turbine tower.

### **3.5.2 Encoder Wheel**

An encoder wheel is attached to the model wind turbine rotor shaft. Figure 3.6 shows the rear view of the encoder wheel. There are two small holes drilled near the edge of the encoder wheel separated by  $180^\circ$  and a third hole placed at a smaller radius. Two pairs of infrared diodes and infrared detectors are positioned on either side of this rotating disk. The diode/detector pair positioned at the outer radius produces a 2 pulse/revolution signal used by the speed controller. The diode/detector pair positioned at the inner radius produces 1 pulse/revolution and is used to trigger the PIV system (see Section 3.7.3)

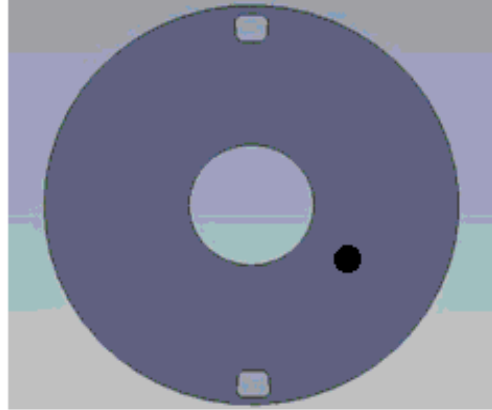


**Figure 3.6: Rear view of the encoder wheel. (Courtesy: Andrew Schenstead).**

### **3.5.3 Speed Controller**

A Magtrol 6100 speed controller was used to control the speed of the wind turbine. One channel of the shaft encoder sends two pulses to the speed controller for each revolution of the turbine blades. The closed-loop speed control system uses a Proportional and Integral (PI) control routine. The “P” parameter was set to 75 and the “I” parameter was set to 20. The algorithm adjusts the current to be sent to the magnetic brake to maintain the set point speed (Magtrol Model 6100 Closed loop Speed Control user’s manual, 2005).

### **3.6 Temperature Sensor**

Power generated by the model HAWT is dissipated to heat in the windings of the magnetic brake. The portion of this heat which does not convect to air passing over the brake serves to increase the temperature of the magnetic brake. As suggested in the user’s manual, the temperature of the brake should not exceed 100°C. A T-type thermocouple connected to a digital

temperature reader (OMEGA digital temperature meter) was placed on the surface of the magnetic brake and during the experiment temperature readings were monitored carefully. When the temperature reached 90°C, testing was suspended to allow the brake to cool down.

### ***3.7 Particle Image Velocimetry***

Particle Image Velocimetry (PIV) is an experimental, quantitative, flow visualization technique. It is an indirect velocity field measurement technique in which the flow is seeded with tracer particles. The particles in the flow region under investigation are illuminated by a laser light sheet. Two consecutive images of the flow field are captured within a very short period of time by a camera and are saved in a computer. These images are then analyzed to find the two-dimensional instantaneous velocity field of the flow region under consideration. Though this method was initially qualitative, developments in optics, lasers, electronics and computer techniques have made it possible to obtain quantitative measurements of complex instantaneous velocity fields. An additional advantage of using PIV over single-point measurement techniques is the ability to determine flow velocities at a very large number of points simultaneously which results in a notable reduction of time in taking experimental data. The nonintrusive characteristics of PIV have also made it attractive. The main objective of this research project is to investigate the flow around a model HAWT. PIV is well suited to obtain the velocity field information compared to point measurement techniques since the whole dataset can be obtained in a relatively shorter period of time.

Figure 3.7 shows a schematic of the PIV system used for flow visualization around the rotor plane of a model horizontal axis wind turbine. This system will be described below.

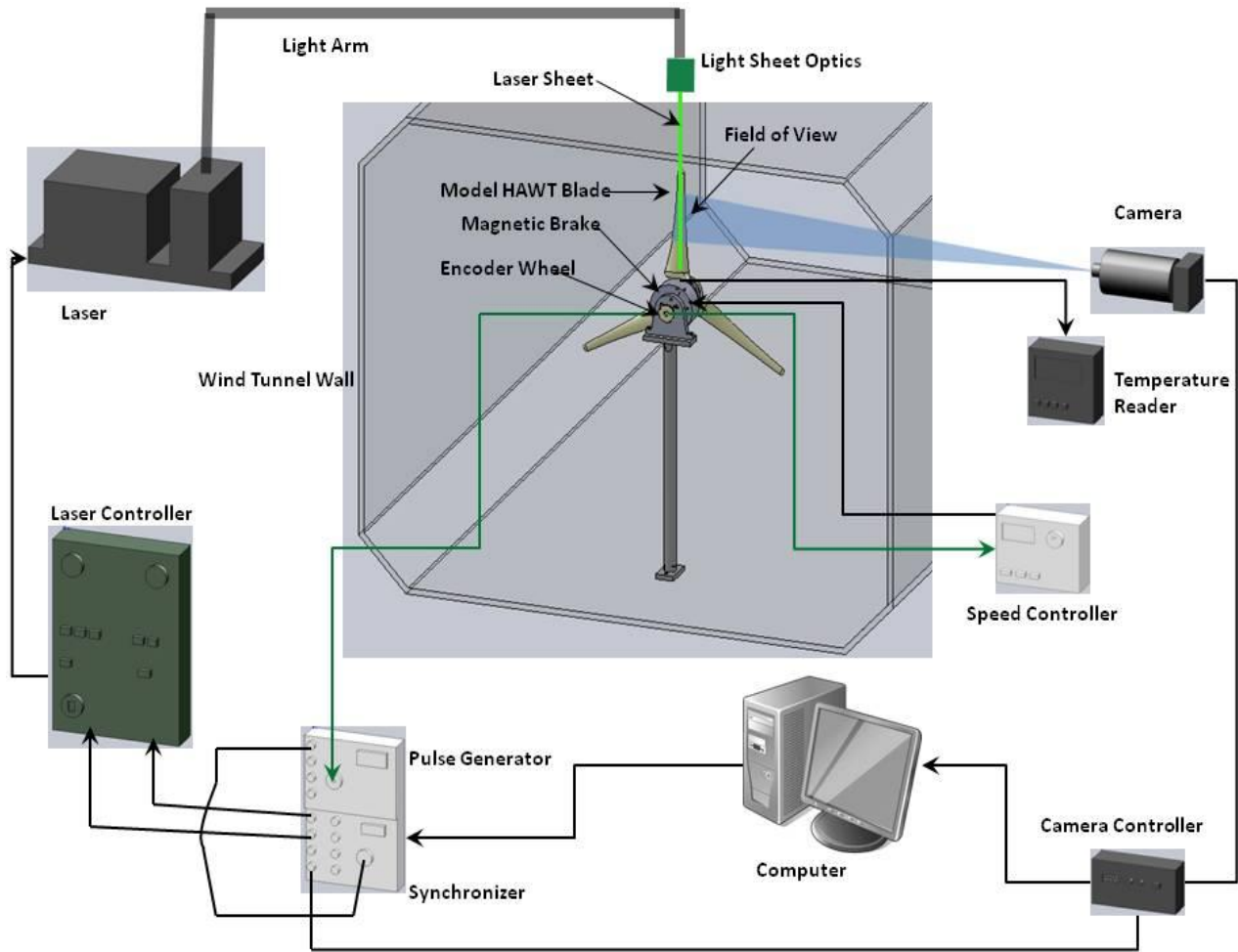


**Figure 3.7: Schematic diagram of the PIV system applied to the flow visualization around the rotor plane of a model horizontal axis wind turbine. (Courtesy: Andrew Schenstead for the Schematic Diagram of model HAWT and wind tunnel)**

### 3.7.1 Seeding and Illumination

#### Fog Generator

To seed the flow a theatrical fog generator (RadioShack FOGGER, 700 W, 70 m<sup>3</sup>/min, Warm up Time: 4 minutes) was placed in the low-speed test section of the wind tunnel. The production of particles was controlled from outside of the wind tunnel with a remote control.

Since the wind tunnel is a closed return type, the particles re-circulate and the loss of particles is only due to deposition of particles on the wind tunnel walls. Some trial images were captured and analyzed to check for satisfactory seeding density. Once it was achieved, seeding was done at a regular interval to make up particle losses. It was assumed that the particles move at the same velocity of the flow. The fog used for this study was Universal Regular Performance Fog Fluid.

### **Laser and Laser Sheet Optics**

The lasers used in this experiment have two power levels. Low power laser is used for ensuring that the laser sheet is aligned correctly and high power is required for illuminating the tracer particles in the field of view. Dual Nd:YAG 200 mJ/ pulse (Newwave Research, Solo 200XT PIV) lasers were used in this study. PIV measurements require two images to be taken a very short time apart. Within that short time ( $\Delta T$ ), two laser pulses are required. However, most pulsed lasers are not able to produce two pulses in that short of a time interval as it takes some time to energize. The energizing time is usually greater than the time required between two consecutive images. The maximum rate at which the current laser can be triggered is 15 Hz. Therefore, two laser sources were used to allow very short intervals between images. The minimum time interval that can be achieved with the existing system is from 0 $\mu$ s. The light pulses were transmitted to the test section through a light arm. The light arm provides the flexibility to move the laser sheet without moving the laser itself.

The laser beam needs to be converted to a light sheet so that it can illuminate the field of view. This was achieved by light sheet optics which consists of two lenses: a spherical lens and a cylindrical lens. The purpose of the spherical lens is to control the thickness of the light sheet and

the cylindrical lens is used to spread the laser beam to form a sheet. A 200 mm spherical lens and a -15 mm cylindrical lens combination was used when measurements were taken at the tip and mid-span portions of the rotor plane and a combination of a 500 mm spherical lens and a -25 mm cylindrical lens was used when measurements were taken at the root section.

### ***3.7.2 Image Capture Equipment***

A MegaPlus ES 4020 digital camera was used to capture the PIV images. The resolution of the camera is 2048 X 2048 pixels. This camera was also used to take the calibration images.

### ***3.7.3 PIV Trigger Equipment***

In this study, PIV images were taken at 15 azimuthal positions relative to the turbine blades (see Section 4.3). This section will describe the triggering system used to take images at the desired azimuthal position.

#### **Pulse Generator and Synchronizer**

The PIV camera and lasers must be triggered at specified and repeatable azimuthal positions of the model wind turbine blades. This is achieved by the combination of a pulse generator and a synchronizer.

The encoder on the wind turbine shaft was connected to the trigger input of the pulse generator (Berkeley Nucleonics Corporation, Model 505 Pulse/Delay Generator). For each rotation of the rotor shaft, the encoder sends a signal to the pulse generator at a fixed azimuthal

position of the rotor. The role of the pulse generator was to prevent trigger signals from the shaft encoder from being passed to the synchronizer during times when the PIV system was not ready to take the next measurement. This was necessary because the rotor speeds (3000 rpm to 5000 rpm) were much faster than the maximum repetition rate of the PIV system (7.5 Hz). To achieve this, the width of the output pulses from the pulse generator was set to 0.5 s and this output pulse was used as a trigger input for the synchronizer. This restricted the data acquisition rate to 2 Hz, well within the capabilities of the PIV system. Two of the synchronizer's (Berkeley Nucleonics Corporation, Model 505 Pulse/Delay Generator) eight output channels were connected to the laser controller and one of the output gates was connected to the camera. The synchronizer was programmed to impose a specific time delay before sending signals to these output channels. That time delay (obtained from PIV trigger calibration, see Section 4.3) is necessary to ensure that images are taken at the desired azimuthal positions

### ***3.8 Uncertainty Analysis***

#### ***3.8.1 Freestream Velocity***

The maximum uncertainty in Pitot-static tube freestream velocity measurements is 0.5%.

#### ***3.8.2 PIV Measurements of $U/U_\infty$***

To assess the uncertainties in the PIV measurements of  $U/U_\infty$ , 500 pairs of PIV images were taken of a boundary layer velocity profile in the high-speed test section of the wind tunnel. The measurements were taken at  $U_\infty = 20.1$  m/s. The velocities were measured at 30 different points in the  $y$  direction (distance perpendicular to the wind tunnel ground plane) inside the

boundary layer and were normalized by the freestream velocity ( $U_\infty$ ). The normalized velocities measured within the boundary layer were compared to the Pitot tube measurements of ( $U/U_\infty$ ) in the boundary layer performed by Rostamy (2012). The PIV and Pitot tube datasets were compared at the same streamwise location. Figure 3.8 compares the normalized velocity measurements at 30 locations within the boundary layer at the centre of the wind tunnel's high-speed test section. The normalized boundary layer profile is shown against normalized wall-normal distances (normalized by boundary layer thickness,  $\delta = 52$  mm). The PIV profile for  $U/U_\infty$  was generated from the first 200 pairs of images. It can be assumed that the difference in the measurements of  $U/U_\infty$  by PIV and the Pitot tube ( $\Delta U/U_\infty$ ) follows the normal distribution (see Figure 3.9). The bias error ( $B$ ) and the precision error ( $P_p$ ) in the measurements of  $U/U_\infty$  were found from the mean and standard deviation of the distribution of errors ( $\Delta U/U_\infty$ ). Then the total uncertainty in the PIV measurements of  $U/U_\infty$  was found by the following equation,

$$\Delta \left( \frac{U}{U_\infty} \right)_{\text{PIV}} = \sqrt{B^2 + P_p^2} = \sqrt{B^2 + (t_{95}S)^2}, \quad (3.2)$$

where  $S$  is the standard deviation and  $t_{95}$  is the Student's t-distribution with 95% confidence interval (which can be assumed to be 2).

For the first 200 images, the uncertainty in the measurements of  $U/U_\infty$  is 2.4%. To check for the dependence of the uncertainty on ensemble size of PIV images, the same analysis was done using the last 200 pairs of the 500 PIV images and then considering all of the 500 pairs of the images. The uncertainty in the measurement of  $U/U_\infty$  considering the last 200 pairs of PIV images was 1.95% and when all 500 pairs were considered the uncertainty was 1.97%. These uncertainty values indicate that ensemble sizes more than 200 pairs would not significantly reduce the uncertainty.

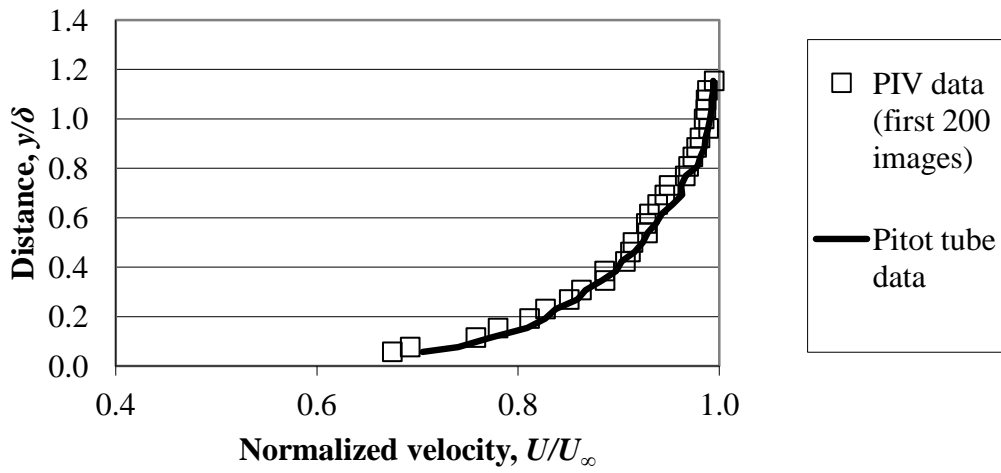


**Figure 3.8: Comparison of normalized velocity measurements within the boundary layer by the PIV and the Pitot tube.**

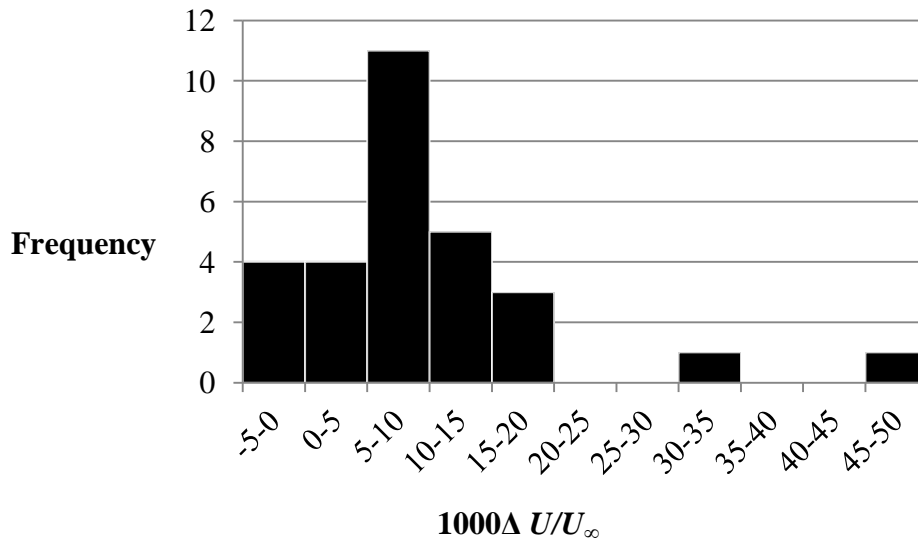


**Figure 3.9: Distribution of  $\Delta U/U_\infty$  obtained at 30 locations in the boundary layer.**

### 3.8.3 Uncertainty in the Measurements of $U$

The velocity at any point ( $U$ ) can be expressed in terms of the freestream velocity ( $U_\infty$ ) as

$$U = \left( \frac{U}{U_\infty} \right) U_\infty. \quad (3.3)$$

Therefore, the uncertainty in the PIV measurements of  $U$  consists of the uncertainties in the measurements of  $U/U_\infty$  and in the measurements of  $U_\infty$ . The maximum uncertainty in the measurement of  $U/U_\infty$  is 2.4% and the uncertainty in the Pitot tube measurements of  $U_\infty$  is 0.5%. This leads to an uncertainty of 2.45% in the measurements of  $U$ .

### 3.8.4 Uncertainty in the Measurements of Axial Induction Factor ( $a$ )

The expression for axial induction factor ( $a$ ) is

$$a = \frac{U_\infty - U}{U_\infty}. \quad (3.4)$$

This expression can also be written as

$$a = 1 - \frac{U}{U_\infty}. \quad (3.5)$$

Therefore, the uncertainty in axial induction factor ( $a$ ) is dependent on the uncertainty in the measurements of  $U/U_\infty$ . The uncertainty in  $U/U_\infty$  is dependent on the uncertainties in  $U$  (2.45%) and  $U_\infty$  (0.5%). This leads to the uncertainties in the measurements of axial induction factor ( $a$ ) in a range from 9.8% to 0.15% for a range of axial induction factor ( $a$ ) from 0.2 to 0.9 respectively.

### 3.8.5 Uncertainty in Tip-Speed Ratio ( $\lambda$ )

The tip-speed ratio ( $\lambda$ ) expression is obtained from  $\Omega$ ,  $R$  and  $U_\infty$  by

$$\lambda = \frac{\Omega R}{U_\infty}. \quad (3.6)$$

This can also be expressed in terms of  $N$ ,  $R$  and  $U_\infty$  as

$$\lambda = \frac{2\pi NR}{60U_\infty}. \quad (3.7)$$

The uncertainties associated with  $R$ ,  $N$  and  $U_\infty$  propagate and are responsible for the total uncertainty in tip-speed ratio ( $\lambda$ ). The uncertainty in  $R$  was assumed negligible. The variation in  $N$  was observed to be approximately 15 rpm and the maximum uncertainty in the measurement of  $U_\infty$  is 0.5%. Table 3.2 shows the resulting uncertainties in the measurement of tip-speed ratio ( $\lambda$ ) for each operating point in the run matrix.

Table 3.2: Uncertainties in tip-speed ratios ( $\lambda$ )

Rotational speed, $N$ (rpm)	Freestream velocity, $U_\infty$ , (m/s)	Tip-speed ratio, $\lambda$	Uncertainty in $N$ , $\Delta N$ (rpm)	Uncertainty in $U_\infty$ , $\Delta U_\infty$ (m/s) (0.5%)	Uncertainty in Tip-speed ratio	% uncertainty in Tip-speed ratio
3000	11	7.14	15	0.055	0.05	0.71
3000	14	5.61	15	0.07	0.04	0.71
5000	13.75	9.52	15	0.068	0.06	0.58
4000	11	9.52	15	0.055	0.06	0.63
4000	14	7.47	15	0.07	0.05	0.63
4000	17	6.15	15	0.085	0.04	0.63

# Chapter 4: The Experimental Approach

## 4.1 Introduction

In this chapter the trigger delay calibration and PIV image calibration procedures will be described. In addition, the operational envelope will be established, the run matrix will be defined, and some preliminary tests and the PIV image analysis methods will be described.

## 4.2 PIV Trigger Delay Calibration

The PIV trigger delay calibration is very important to determine the delay time ( $t_{\text{delay}}$ ) required to take PIV images at particular azimuthal positions relative to the turbine blades. The encoder wheel sends a trigger signal to the pulse generator at a fixed angular position ( $\theta_{\text{trig}}$ ). The delay time is the time needed for blade 1 to advance to the desired azimuthal positions ( $\theta_{\text{PIV}}$ ) from  $\theta_{\text{trig}}$ .

The relation between the azimuthal positions of the blades relative to the PIV light sheet ( $\theta_{\text{PIV}}$ ) and delay times ( $t_{\text{delay}}$ ) is

$$\theta_{\text{PIV}} - \theta_{\text{trig}} = \Omega t_{\text{delay}} + \Omega t_{\text{elec}} , \quad (4.1)$$

where  $\theta_{\text{PIV}}$  is the position of blade 1 when PIV data is taken,  $\theta_{\text{trig}}$  is the position of blade 1 when the shaft encoder pulse is produced,  $\Omega$  is the rotor angular velocity,  $t_{\text{delay}}$  is the required delay, and  $t_{\text{elec}}$  is an inherent delay in the PIV electronics. The left hand side of this equation is the

angular distance the rotor travels between when an encoder trigger signal is produced and when PIV data is taken. This equation can be written as

$$t_{\text{delay}} = (\theta_{\text{PIV}} - \theta_{\text{trig}}) (\Omega^{-1}) - t_{\text{elec}} . \quad (4.2)$$

A calibration process is required to determine  $\theta_{\text{trig}}$  and  $t_{\text{elec}}$ . This was done by determining the  $t_{\text{delay}}$  required to produce  $\theta_{\text{PIV}} = 0$  for various turbine speeds ( $\Omega$ ).

To establish  $\theta = 0^\circ$  position, the model HAWT was mounted inside the wind tunnel without the nose cone. Blade 1 was fixed in the vertical position by hanging a plumb bob from the tip of the blade at the quarter chord point. The blade was made vertical by ensuring that the string from which the plumb bob was hanging passed through the rotor shaft centre. This is the  $0^\circ$  azimuthal position of blade 1. Figure 4.1 shows the plumb bob hanging and the string passing along the quarter chord line and the rotor shaft centre.



(a)



(b)

**Figure 4.1: Plumb bob hanging from the tip of the quarter chord line at  $\theta = 0^\circ$ : (a) the string passing along the quarter chord line and (b) the string passing through rotor shaft centre.**

The light sheet was then directed downwards from the top of the wind tunnel and carefully positioned so that it hit the quarter chord line at the tip of blade 1 and also struck the centerline of the wind tunnel on the ground plane. Figure 4.2 shows the laser hitting the tip of the quarter chord line. This procedure ensures that the light sheet is aligned at the  $\theta^\circ = 0$  position.

The camera was then temporarily positioned so that the laser hitting the quarter chord line was clearly visible. Then, the plumb bob was removed, the wind tunnel was turned on, and the turbine speed was varied from 2000 rpm to 5000 rpm in increments of 500 rpm. At each turbine speed, the synchronizer delay time ( $t_{\text{delay}}$ ) was determined by trial and error until the light sheet illuminated the quarter chord line. These delay times were plotted against the inverse of  $\Omega$  in Figure 4.3 and a linear least-squares line is fitted to the data. The slope of this line is  $-\theta_{\text{trig}}$  and the y-intercept is  $-t_{\text{elec}}$ .



**Figure 4.2: Laser sheet hitting the quarter chord line of Blade 1 at  $0^\circ$  azimuth.**

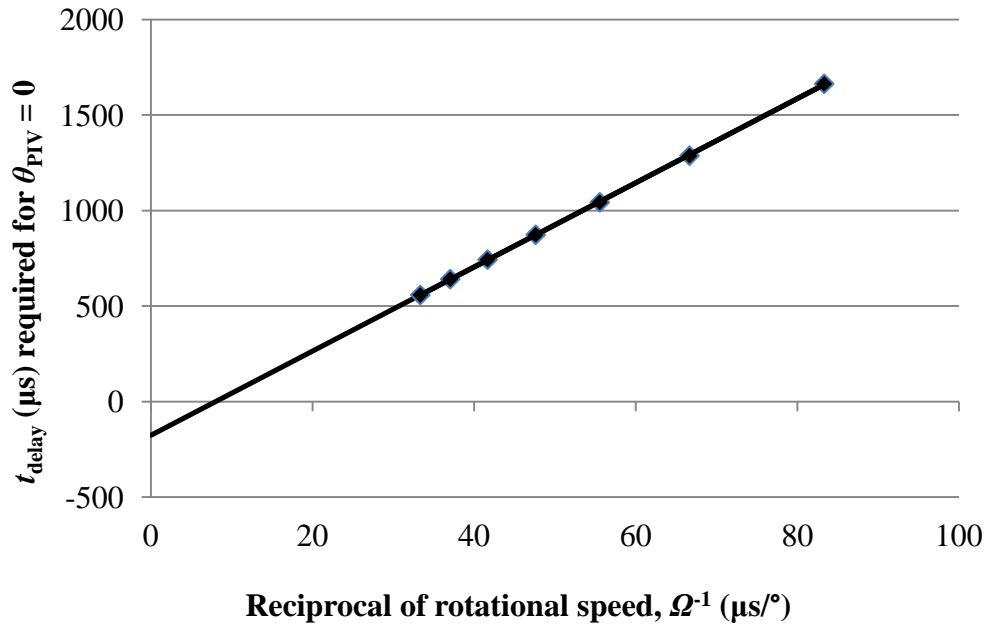


**Figure 4.3: Trigger delay calibration curve.**

The value of  $\theta_{\text{trig}}$  was found to be  $-22.01^\circ$  and the value of  $t_{\text{elec}}$  was found to be  $176.22 \mu\text{s}$ . The value of  $\theta_{\text{trig}}$  will vary depending on the position on the shaft where the rotor is mounted. Hence, each time the rotor was decoupled from the shaft a new trigger delay calibration was performed as it could not be ensured that each time the rotor was mounted exactly at the same position on the shaft.

Once  $\theta_{\text{trig}}$  and  $t_{\text{elec}}$  are determined, the  $t_{\text{delay}}$  required for any desired  $\theta_{\text{PIV}}$  can be determined from equation 4.2.

### 4.3 Azimuthal Positions of the Turbine Blades

In order to investigate the variation of axial induction factor ( $a$ ) with the blade position PIV images were taken at 15 different azimuthal positions of blade 1 relative to the PIV plane. Instead of changing the PIV plane of measurement with respect to the vertical position of the turbine blade, measurements were taken at a fixed PIV plane but at different angular positions of blade 1. The model HAWT has three blades and the angles between the blades are  $120^\circ$ . Due to the symmetry of the turbine rotor, one third (angle between two blades) of the entire rotor plane can be considered as the representative section. The angle between blade 1 and blade 2 was divided into 18 positions as shown in Figure 4.4. The range of angles chosen for this purpose is  $-15^\circ < \theta < 95^\circ$ . As greater variations were expected closer to the blade, smaller increments were chosen near the blade. Within the range  $-15^\circ < \theta < 15^\circ$  positions were chosen at  $5^\circ$  increments whereas within the rest of the range positions at  $10^\circ$  increments were chosen.

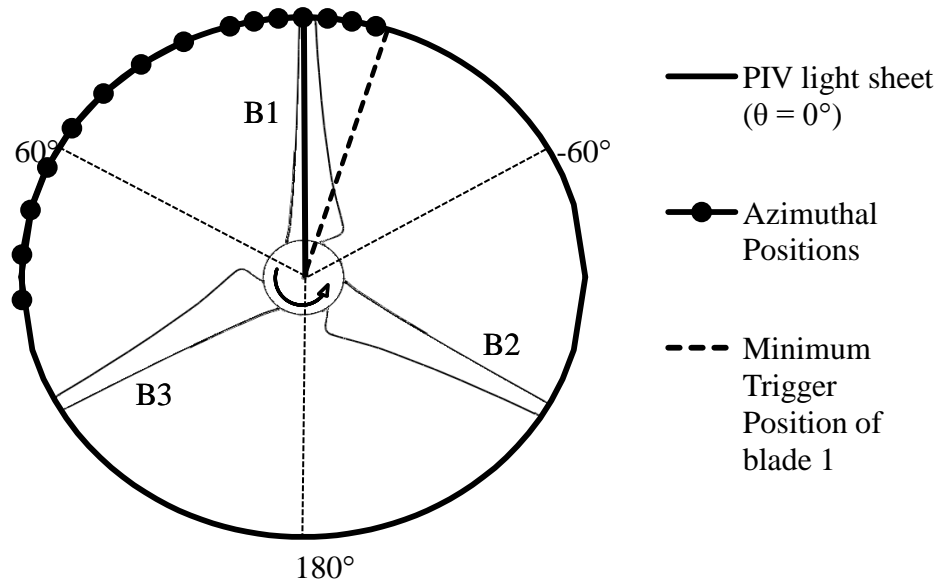


**Figure 4.4: Azimuthal positions of blade 1 where PIV measurements were taken (Courtesy: Andrew Schenstead for schematic of the blades)**

#### 4.4 Operational Envelope of the Apparatus

The two main operational parameters that can be varied in this apparatus are the freestream velocity ( $U_\infty$ ) and the rotor speed ( $N$ ). This section will define the operational envelope in this parameter space. The freestream velocity in the wind tunnel does not remain steady below 10 m/s. At any speed higher than 17 m/s the model HAWT generates too much power which over heats the magnetic brake and it cannot run very long. At very high rotational speed centrifugal forces on the turbine blades become very high causing a very high stress in the blades which could lead to a mechanical failure of the blades. Therefore, the rotational speed was limited to 5000 rpm. Low freestream velocities and high rotational speeds (i.e. high  $\lambda$ ) cannot be achieved as the kinetic energy in the flow is not sufficient to run the model HAWT at higher speeds. High freestream velocities and low rotational speeds (i. e. low  $\lambda$ ) could not be achieved as the speed controller fails to control the speed of the model HAWT. Figure 4.5 shows the experimental operational envelope.

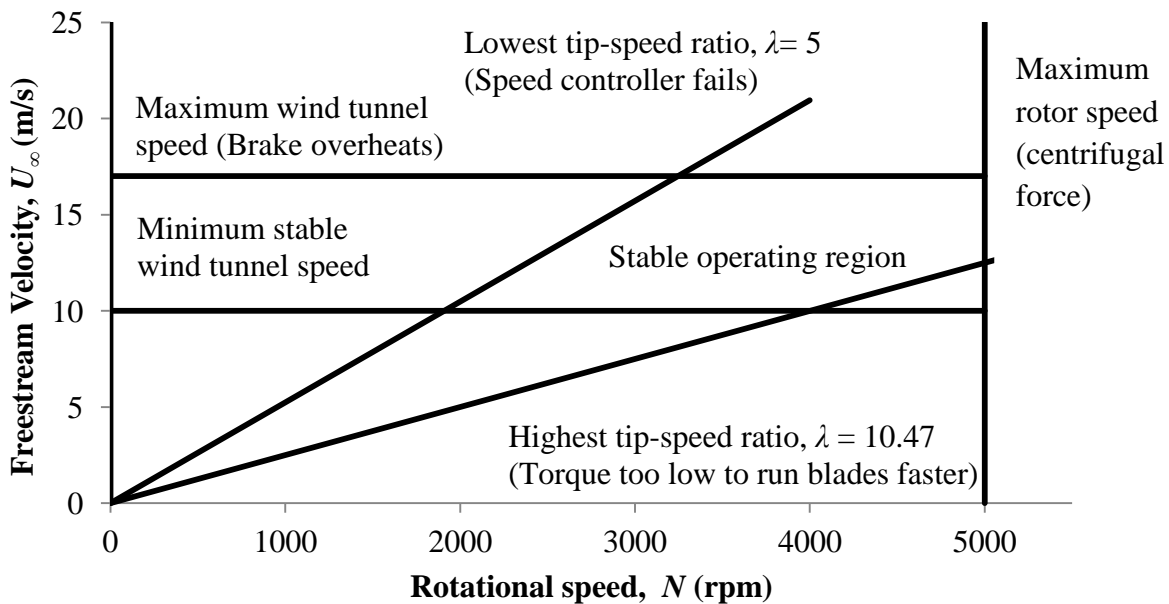
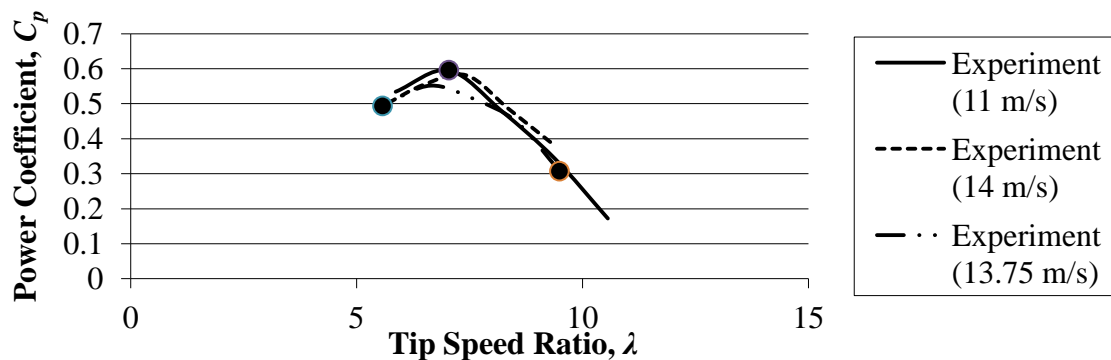


Figure 4.5: The experimental operational envelope.

#### 4.5 The Run Matrix

To determine the operating conditions at which PIV measurements would be taken, a preliminary test of the model was performed. The wind tunnel was run at 11 m/s, 14 m/s and 13.75 m/s. For each freestream velocity, the turbine was run at speeds from 2000 rpm to 5000 rpm in increments of 500 rpm. Based on preliminary testing, operating characteristics curves of the model wind turbine were produced and operating conditions were chosen as-  $\lambda = 9.52, 7.14$  and 5.61. The circles in Figure 4.6 show the new operating conditions on the operational characteristics curve for the model HAWT used in this study.

PIV measurements were taken at five tip-speed ratios. Schenstead (2012) took data upstream of the rotor at three tip-speed ratios. The present study will complete these datasets by taking PIV measurements at the same conditions but downstream of the rotor. In addition, one tip-speed ratio studied by Schenstead (2012) will be repeated but it will be achieved by a different combination of freestream velocity and rotational speed of the rotor. Also, two additional tip-speed ratios will be studied. The values of the tip-speed ratios ( $\lambda$ ) are chosen so that full range of operating behavior from optimum operating condition (optimum  $C_p$ ) to non-



**Figure 4.6: Operating characteristics curve for the model HAWT.**

optimum operating condition (high  $\lambda$ ) can be investigated. Table 4.1 shows the operating conditions of Schenstead (2012), the operating conditions for present study and dataset locations used in present study.

For each of the tip-speed ratios ( $\lambda$ ), PIV images were taken at 15 different azimuthal positions ( $\theta_{PIV}$ ) of the turbine blades. To capture the whole flow field near the rotor plane along the radial distance of the model HAWT, three fields of view were required on the upstream side. These fields of view (FOV) were named as TIP FOV, MID FOV and ROOT FOV. Due to the presence of the magnetic brake on the downstream side, only two fields of views were required to cover the radial distance of the blades; TIP FOV and ROOT FOV. Fields of views were chosen in such a manner so that sufficiently large particle sizes were obtained to get good correlations for the PIV image analysis. Table 4.2 shows the sizes of the fields of view on both the upstream and downstream sides. Both the TIP FOVs covered a little beyond the tip to capture the flow field over the blade tip. The bottom edge of the upstream ROOT FOV and downstream ROOT FOV were set at a little bit above the centre line due to the presence of the nose cone on the upstream side and the magnetic brake on the downstream side.

Table 4.1: Operating conditions and locations of the Datasets.

Experiment	Freestream velocity, $U_\infty$ (m/s)	Rotor speed, $N$ (rpm)	Tip Speed Ratio, $\lambda$ (-)	Dataset Locations
Schenstead (2012)	11	4000	9.52	Only on the upstream side
	14	4000	7.48	
	17	4000	6.16	
Present Study	11	4000	9.52	Only on the downstream side
	14	4000	7.48	
	17	4000	6.16	
	11	3000	7.14	Both upstream and downstream side
	14	3000	5.61	
	13.75	5000	9.52	

Table 4.2: Sizes of the fields of view.

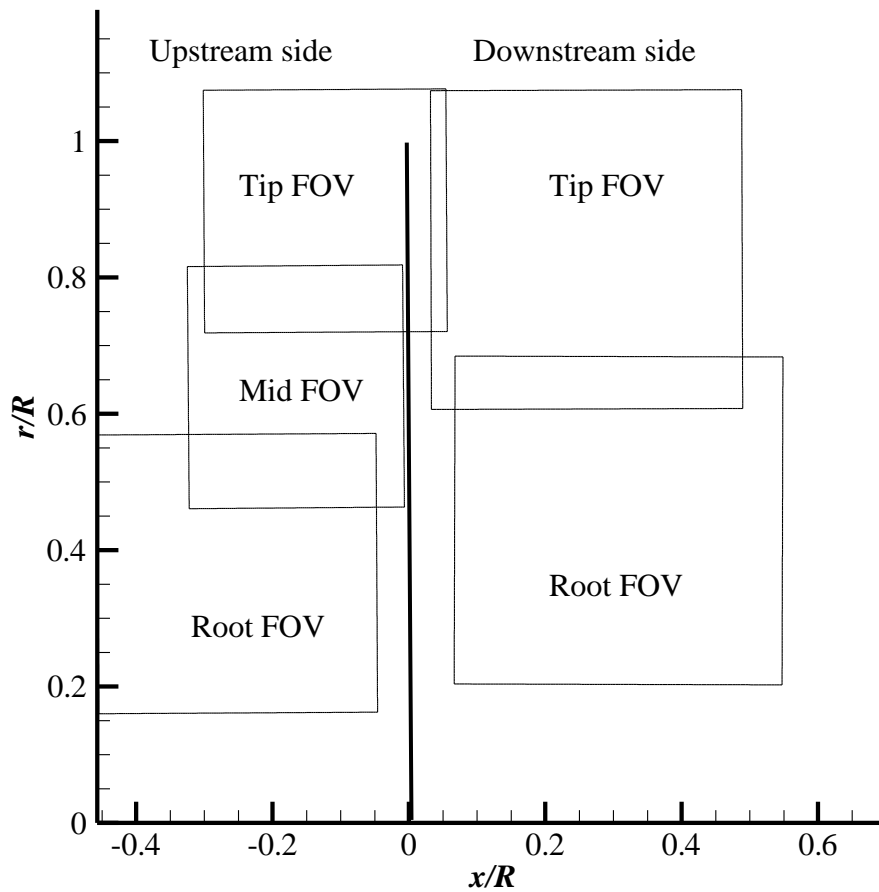
Rotor plane side	Field of View	Approximate Size of the Field of View
Upstream side	Tip FOV	9 cm x 9 cm
	Mid FOV	9 cm x 9 cm
	Root FOV	10 cm x 10 cm
Downstream side	Tip FOV	12 cm x 12 cm
	Root FOV	12.2 cm x 12.2 cm

Figure 4.7 shows the locations of the fields of view when the blade is at  $0^\circ$  with respect to the PIV plane of measurement.

At each operating conditions and at each of the 15 azimuthal positions of the turbine blades 200 pairs of PIV images were captured for each field of view. Table 4.3 shows the run matrix for the experiment.

Table 4.3: The run matrix for the present experiments.

Location of FOV	Freestream Velocity, $U_\infty$ (m/s)	Rotor Speed, $N$ (rpm)	Tip Speed Ratio, $\lambda$	Number of Azimuthal Positions, $\theta$	Number of FOV	Raw Image Pairs	Total Raw Image Pairs	Dataset Size
Upstream	11	3000	7.14	15	3	200	108000	864 GB
	14	3000	5.61					
	13.75	5000	9.52					
Downstream	11	3000	7.14	15	2			
	14	3000	5.61					
	13.75	5000	9.52					
	11	4000	9.52					
	14	4000	7.48					
	17	4000	6.16					



**Figure 4.7: Locations of the fields of view.**

#### **4.6 PIV Image Calibration**

Because the velocity field is measured as a composite of five fields of view (see Figure 4.7) there is a need to transform the velocity field data from the five individual “camera” coordinate systems to a single global coordinate system (as defined in Figure 3.3). PIV raw images are in the camera coordinate system. Analyzing PIV images gives the displacement of the tracer particles and velocity fields in the camera coordinates. It calculates displacements of

particles in pixels and velocities in pixels per unit time. To convert camera coordinates into the global coordinate system, PIV image calibration is needed. The first step of this calibration procedure is to take calibration images by the PDVshow software. A vertical steel ruler was placed at a location in the field of view where the horizontal global coordinate ( $x$  coordinate) of one of its edges was known. When the upstream side of the rotor was under investigation the steel ruler was placed vertically touching the tip of the nose cone with the 0 mark on the steel ruler placed exactly at the tip of the nose cone. It was assumed that the centre of rotation of the rotor plane passes exactly through the tip of the nose cone. Figure 4.8 (a) shows the calibration image of the upstream ROOT FOV. It was known that the tip of the nose-cone was 56 mm from the rotor plane. When the downstream side was considered the steel ruler was placed vertically touching the rear edge of the magnetic brake. The horizontal distance of the rear edge of the magnetic brake was known to be 67 mm from the rotor plane. Figure 4.8 (b) shows the downstream ROOT FOV calibration image.

In order to perform the calibration, the calibration image needs one point for which both the global coordinates and the camera coordinates were known. This point was given as one of the inputs in a Excel calibration file. The coordinates of this point are used to calculate the required translation when converting the camera coordinates into global coordinates. To calculate the required rotation around the axis perpendicular to the field of view, pixel values of any two points on one edge of the steel ruler were given input to the Excel calibration file. The centimeter marks on the steel ruler in the calibration image indicate the vertical distance in the



(a)



(b)

**Figure 4.8: Calibration images: (a) Root upstream field of view and (b) Tip downstream field of view.**

global coordinate system from the center of rotation of the rotor plane which passes through the origin. To calculate the calibration factor, pixel values and actual measurements along the steel ruler were plotted. The slope of a best-fit line yielded the calibration factor. The calibration factor is actually the factor by which the camera coordinates (pixels) need to be multiplied to give global coordinates (m). Depending on the camera position, the direction of flow in PIV images can be varied from left to right or from right to left. The calibration file also adjusts the flow direction always to the conventional left to right direction.

#### 4.7 PIV Image Capture

For PIV image capture PIVAcquire Ver 1.2.1 software was used. There are two modes in which this software can be run: focus mode and PIV mode. Focus mode is required to align the light sheet along the field of view and PIV mode is for taking PIV images. The software was run in PIV mode and putting required delay time obtained from the PIV trigger calibration file 200 pairs of raw images were captured at each of the azimuthal positions of the blades. The raw images could be viewed in RawView (Version 1.2.2). Both of the images of a single pair are saved in one file and both of the images can be viewed by toggling in between the two images. Figure 4.9 shows one of the raw images of the upstream TIP FOV when the model HAWT was running at  $\lambda = 9.52$  and  $\theta = 0^\circ$ .

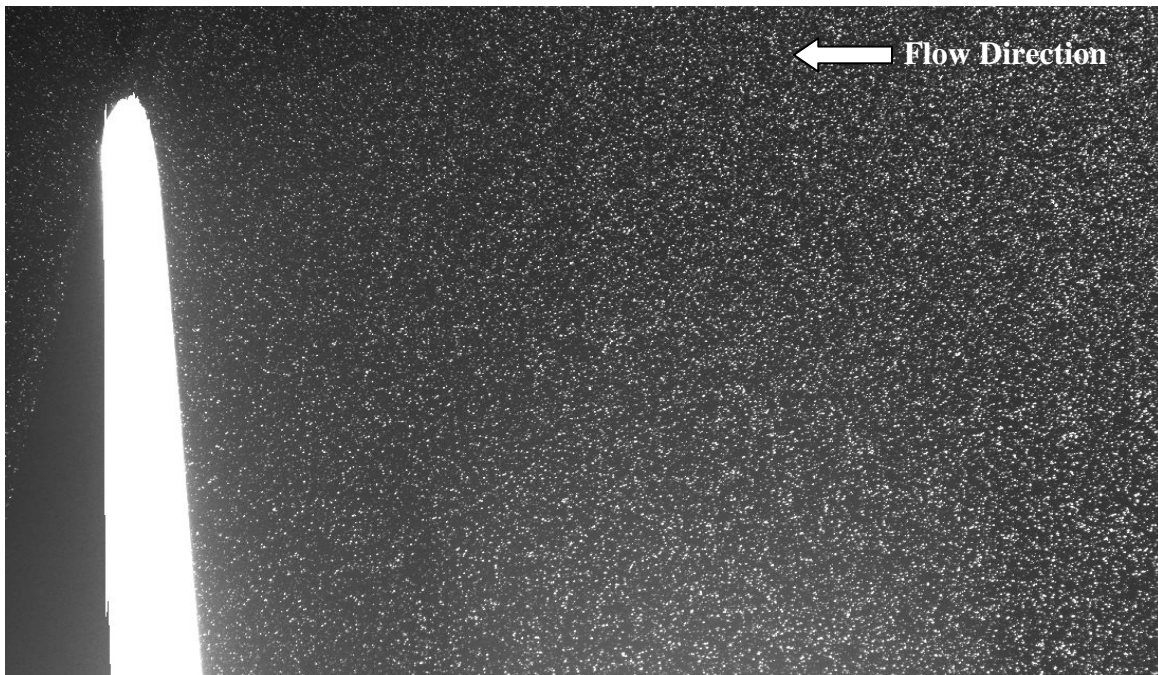


**Figure 4.9: Portion of a raw image of tip field of view of the dataset  $\lambda = 9.52$  at  $\theta = 0^\circ$ .**

#### **4.8 PIV Image Analysis**

Image analysis was performed with PIVAnalysis (Ver. 1.5.4) software. In this software all 200 pairs of images at each azimuthal position were loaded and analyzed together. During image analysis, the images are divided into a finite numbers of smaller areas known as interrogation areas (IA). By correlating one IA of the first image with the corresponding IA in the second image the software finds the displacement of the particles in that IA. To analyze the images obtained from this experiment an interrogation area of 64x64 pixels with 50% overlap in both  $X$  and  $Y$  directions was used. The analysis settings were set to Half-Padded FFT with Gaussian sub-pixel algorithm. To find the peak of the correlation plane the Relative Maxima peak finding algorithm was used. Analysis was done in two levels with smaller interrogation areas (32 pixels). This two-level analysis allows the use of smaller interrogation areas even if the particle displacement in the images is larger. Analyzing in this manner produces a velocity field with a total of 16,384 velocity vectors.

#### **4.9 Image Masking**

Some of the raw images had significant reflections from the model HAWT blades, nose cone and magnetic brake. The vectors in these regions were undoubtedly spurious since particles were not visible. To avoid these spurious vectors in the final vector field, the images were masked in the regions where too much reflection was observed. A masking file was created for each group of affected images. During analysis, these masking files were loaded in the analysis software. In the analysis with masking, the masking region is totally overlooked by the analysis software and no information about particle displacements is produced.

#### **4.10 *Outlier Rejection***

After PIV analysis there are always some randomly aligned vectors present. If the sizes of the interrogation areas are too small then the correlation becomes weak and it can give birth to spurious vectors in the vector field. In the outlier reject part of PIV image analysis, these vectors are identified and replaced with vectors interpolated from nearby good vectors. For outlier rejection OutlierReject (Ver. 1.5.4) software was used. Outlier identification was done by Cellular Neural Network (CNN) algorithm (Shinneeb, 2006). For outlier replacement, a Gaussian weighing function with a width of 8 pixels was used. This process resulted in a mean data file containing the average vector field information of 200 pairs of images. In such a manner the data files for each of the operating conditions, each of the azimuthal positions and each of the fields of view were generated.

These data files can be loaded and plotted in any plotting software to visualize the flow fields. For plotting the vector fields Tecplot 360 2010 was used.

# Chapter 5: Results

## 5.1 Introduction

In this chapter, the experimental results and the Blade Element Momentum method results will be presented. First, characteristic curves generated from the experimental data and the Blade Element Momentum method will be compared. Then, the PIV results will be presented and will be ultimately compared with BEM predictions of the radial distribution of axial induction factor ( $a$ ) at the rotor plane.

## 5.2 Characteristic Curve

A plot of power coefficient ( $C_p$ ) versus tip-speed ratio ( $\lambda$ ) is the characteristic curve for a wind turbine. Wind tunnel tests of the model horizontal-axis wind turbine (HAWT) were performed to obtain the characteristic curve and to determine the operating conditions at which PIV measurements would be made. The wind tunnel was operated at three different freestream velocities (11.16 m/s, 14.1 m/s and 13.8 m/s) and the model HAWT was operated at different rotational speeds ranging from 2000 rpm to 5000 rpm. For each run, the freestream velocity was fixed and the rotational speed was varied in 500 rpm intervals to obtain different tip-speed ratios. For each tip-speed ratio, the current supplied to the hysteresis brake was recorded. Corresponding values of torque were found from the hysteresis brake calibration curve. This torque is equal to the torque generated by the model HAWT. Multiplying this torque by the rotational speed ( $\Omega$ ) of the model wind turbine yields the power generated. Due to the hysteresis inherent in the brake, two values of torque can be found corresponding to each current

measurement. The difference between these two torques is the uncertainty in each measurement. The hysteresis curve has a maximum error of 0.159 N.m in torque at a current of 0.304 A. The power coefficient ( $C_p$ ) values were found by using the following equation,

$$C_p = \frac{\dot{W}}{\frac{1}{2} \rho A U_\infty^3}, \quad (5.1)$$

where  $\dot{W}$  is the actual power generated by the model HAWT,  $\rho$  is air density,  $A$  is the rotor area and  $U_\infty$  is the freestream velocity.

A characteristic curve for the same wind turbine geometry was generated by WT\_Perf for Trip2 and multiRe conditions (Buhl, 2004). These two conditions are related to how the separation of the boundary layer on the wind turbine blades are treated in the Blade Element Momentum (BEM) method. For the Trip2 calculations, the boundary layer separation is assumed to occur at a predefined fixed location on the blade. For the multiRe calculations, the boundary layer separation point varies with operating conditions. Figure 5.1 compares the characteristic curve between the experiments and the BEM predictions for the three different freestream velocities.

At lower tip-speed ratios the wind turbine runs very slow and most of the incoming flow passes between the blades without contributing to power production. That is why at lower tip-speed-ratios the value of power coefficient is lower. At high tip-speed ratios the power coefficient is also low since the wind turbine is running so fast that the rotor plane appears more like a solid wall to the incoming flow. There is an optimum tip-speed ratio where the wind turbine runs most efficiently giving maximum power output. The tip-speed ratio corresponding

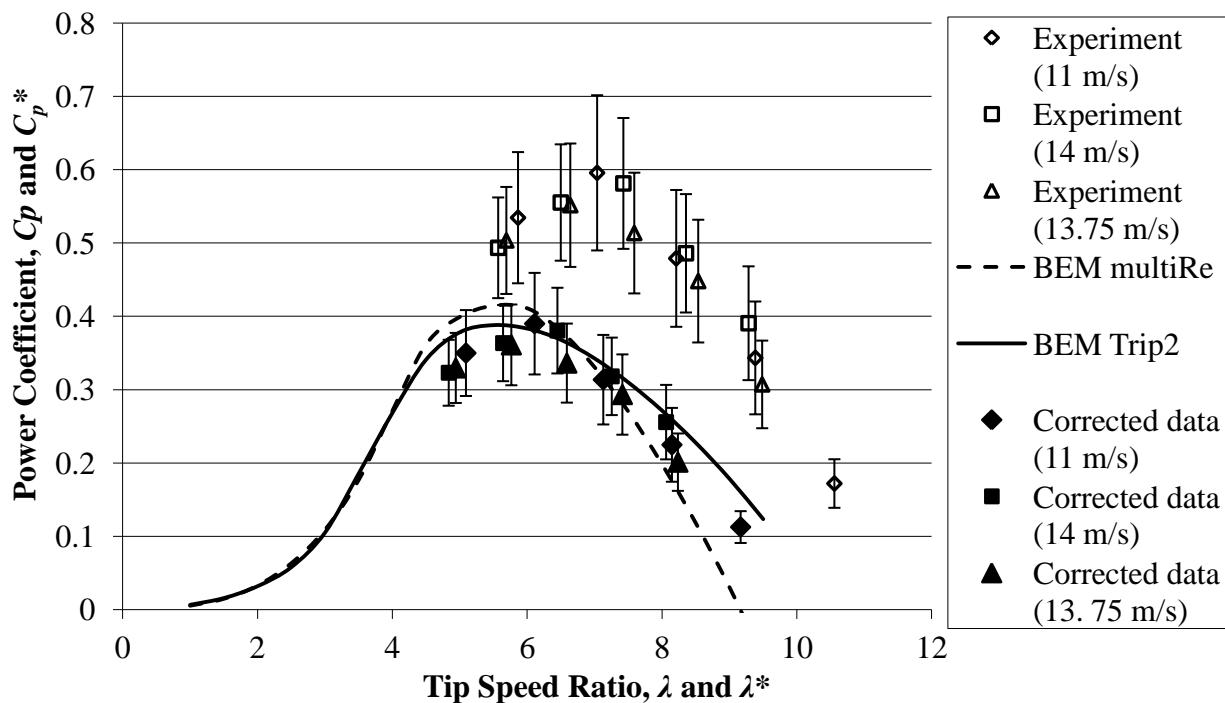


**Figure 5.1: Comparison of characteristic curve obtained from the experiment and BEM method.**

to this maximum power coefficient is known as the optimum tip-speed ratio. The experimental optimum tip-speed ratio is higher than the optimum tip-speed ratio for the BEM predictions. Maximum power that can be achieved occurs at tip-speed ratios near six as predicted by the BEM method whereas the achievable maximum power in the uncorrected experimental data occurred at tip-speed ratios near seven.

The model wind turbine inside the wind tunnel generates more power than is predicted by the Blade Element Momentum method at all the operating conditions. In wind tunnel experiments, the experimental dataset suffers confinement effects due to the wind tunnel walls. As the flow approaches the rotor plane it cannot deflect around the rotor as much as the flow

around a wind turbine operating in open atmospheric conditions. The confinement effect of the wind tunnel walls force the air flow to follow a constrained path around the wind turbine rotor plane leading to the generation of more power. To correct for these effects, Werle (2010) derived a correction factor for the optimum power coefficient (optimum  $C_p$ ) and scaled it over all operating conditions to obtain

$$C_p^* = \left(1 - \frac{A}{A_T}\right)^2 C_p, \quad (5.2)$$

where  $A$  is the cross-sectional area of rotor plane,  $A_T$  is the cross sectional area of the wind tunnel,  $C_p$  is the uncorrected power coefficient and  $C_p^*$  is the corrected power coefficient. In this thesis, the corrected freestream velocity ( $U_\infty^*$ ) was corrected using

$$U_\infty^* = \frac{U_\infty}{\left(1 - \frac{A}{A_T}\right)^{2/3}}, \quad (5.3)$$

which was used to calculate a corrected tip-speed ratio using

$$\lambda^* = \frac{R\Omega}{U_\infty^*}. \quad (5.4)$$

These equations reduce the experimental power coefficients to more realistic values. In Figure 5.1, corrected power coefficients ( $C_p^*$ ) as a function of corrected tip-speed ratio ( $\lambda^*$ ) are also shown for different freestream conditions. The corrected results of the power coefficients match with the BEM results much better than the uncorrected data.

From the experiment it was not possible to obtain the values of power coefficients at low tip-speed-ratios. In fact, data could not be taken at tip-speed ratios lower than  $\lambda = 5$ . This was due

to the inability of the speed controller to perform consistently. However, it was possible to obtain results at these lower tip-speed ratios from the Blade Element Momentum method.

### ***5.3 Velocity Field around the Rotor Plane***

In total, five PIV fields of view (three upstream and two downstream) were used to find the velocity field around the rotor plane of the model HAWT. The PIV images of these fields of view were taken at 15 azimuthal angles for five tip-speed ratios and were analyzed to generate two-dimensional velocity fields (radial and axial components) around the rotor plane. Since PIV is a whole-field measurement technique, instantaneous two-dimensional velocity fields at a large number of points in the fields of view could be generated in a relatively short period of time. Figure 5.2 shows the mean velocity field for  $U_\infty = 14$  m/s,  $N = 3000$  rpm,  $\theta = 5^\circ$ . The velocity field contains 81,920 velocity vectors. The figure presented shows every eighth vector in both directions.

From Figure 5.2 it is observed that the data contain radial and axial components of velocity at any point from  $0.46R$  upstream to  $0.58R$  downstream and up to a radial distance of  $1.08R$  from the centre of rotation (except for the masking regions). Due to laser reflections from the blades, nose cone and magnetic brake, the vectors in these masked regions were neglected. Similar velocity fields were generated from all of the PIV images taken at all the blade azimuthal angles at all operating conditions. One of the advantages of this kind of vector field is the richness of data in terms of flow field information. Slices can be extracted from any plane to find the axial or radial variation of either of the two components of the velocity field. These vector fields, along with the freestream velocity, contain information about the axial induction factor ( $a$ ) at every location.

The vector field reveals the presence of the vortices generated from the blade tips of the HAWT. Some vector fields contain two vortices and some of them have one vortex. The number of vortices expected to be present in the vector field depends on the vortex convection time downstream of the rotor plane and on the size of the fields of view. Due to the smaller size of the

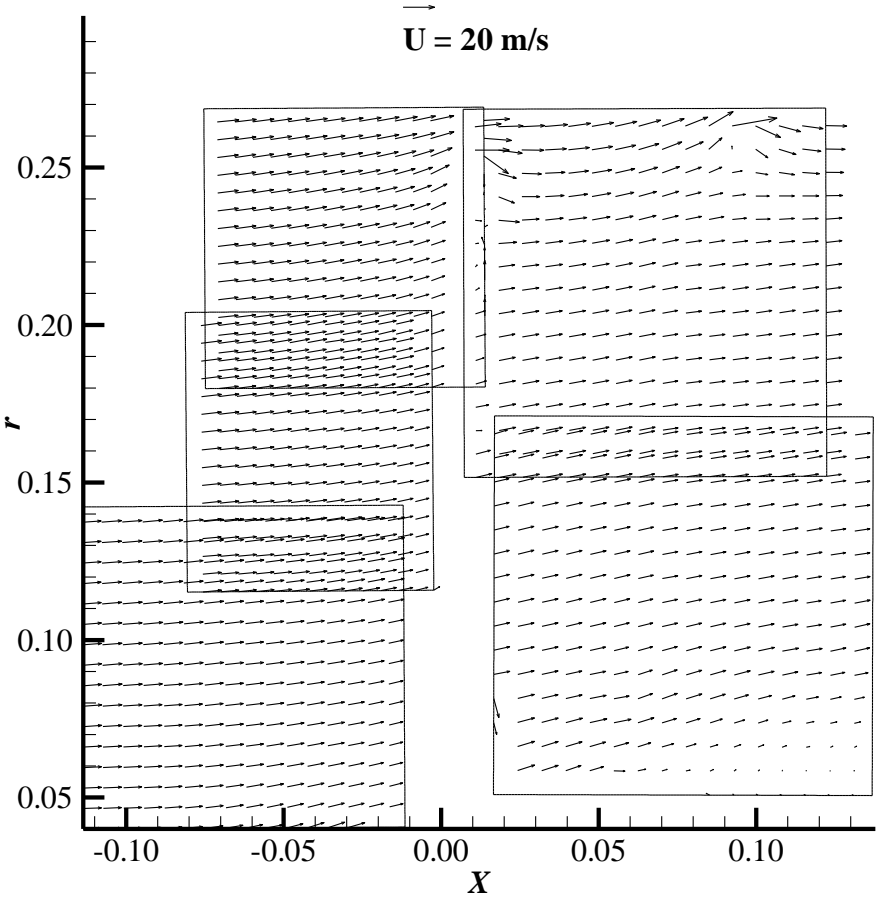


**Figure 5.2: A typical PIV vector field around the rotor plane of the model HAWT. ( $U_\infty = 14 \text{ m/s}$  and  $N = 3000 \text{ rpm}$ )**

fields of view on the downstream side, three vortices (generated from three blades of the model HAWT) were never observed at the same time in a single vector field.

Figure 5.3 shows a PIV image of one of the tip vortices cut from a full raw image and the corresponding velocity field of the tip vortex. The vectors generated in the core of the tip vortex are spurious as there are no seed particles found in this region. Due to the very strong rotation in the core of the vortices, seed particles were thrown out resulting in poor correlation during the PIV analysis. Smaller seed particles would be required to measure the velocity in the core of these tip vortices.

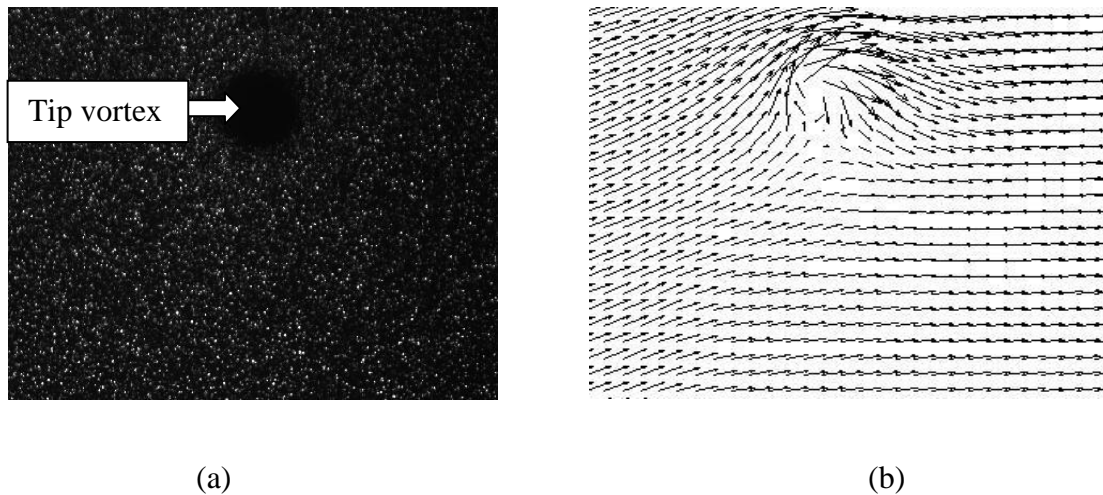


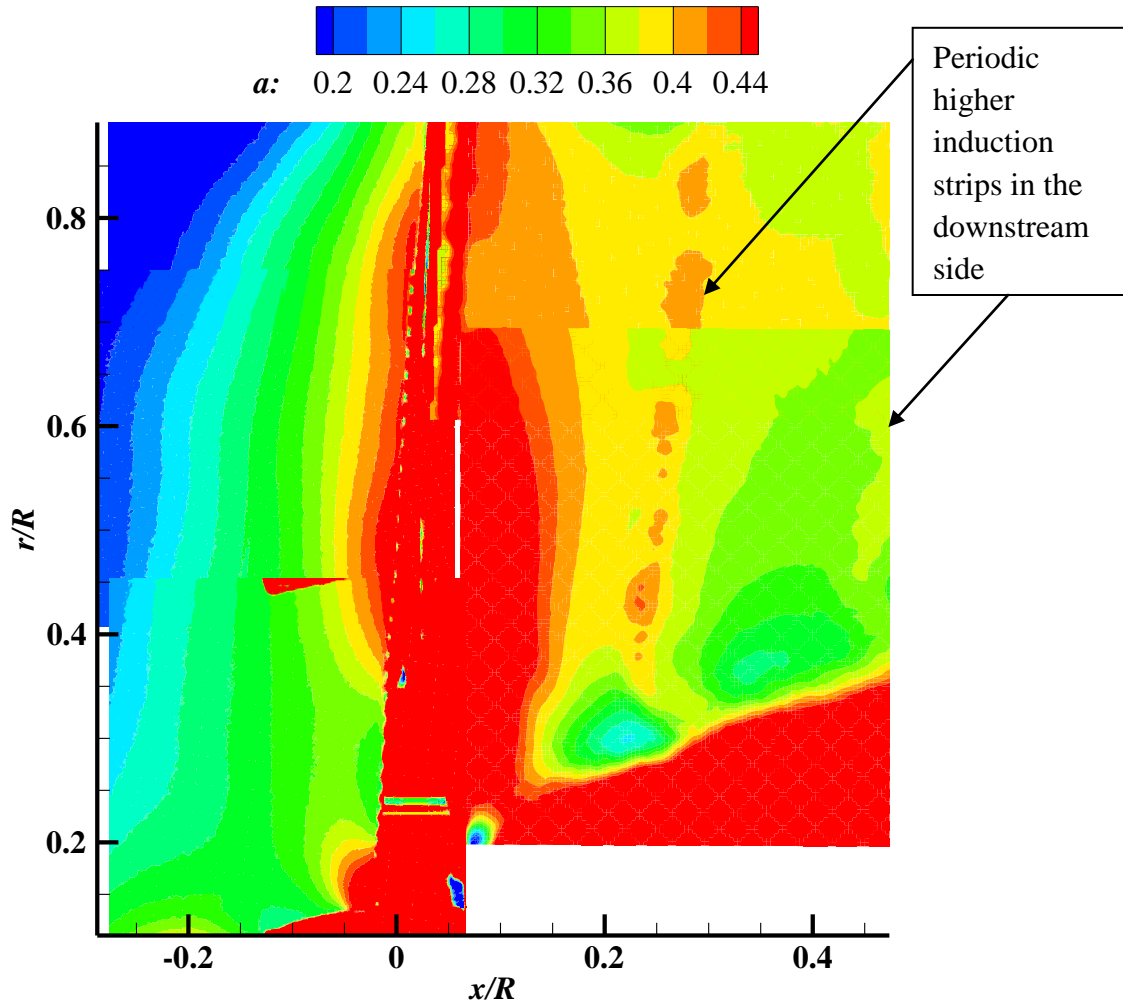
**Figure 5.3: One of the tip vortices: (a) tip vortex shown in a PIV raw image and (b) velocity field in a tip vortex.**

#### **5.4 Axial Induction Factor**

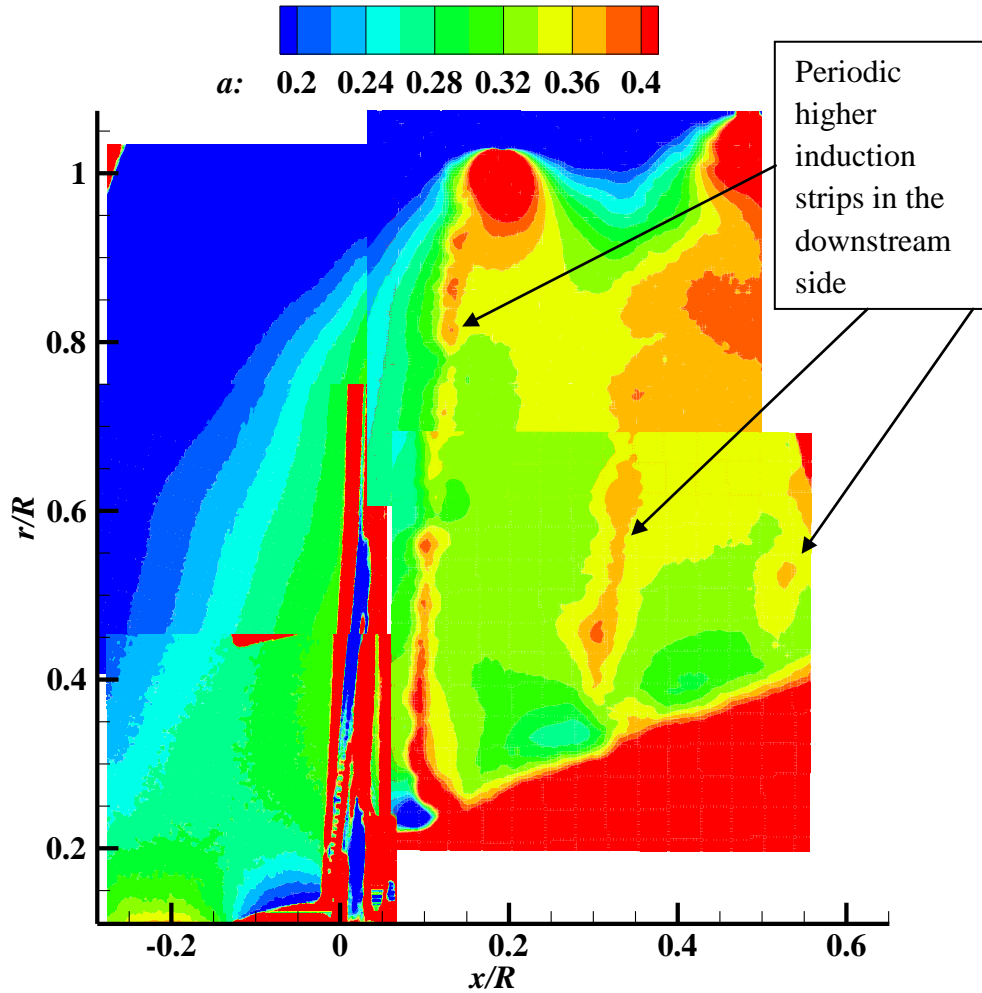
The axial induction factor ( $a$ ) at every location in the flow field was computed by

$$a = \frac{U_\infty - U}{U_\infty}, \quad (5.5)$$

where  $U$  is the axial component of velocity at any point inside the velocity field and  $U_\infty$  is the freestream velocity. Figures 5.4(a) and (b) show the axial induction factor ( $a$ ) distribution surrounding the rotor plane. The most striking features of these plots are the periodic “bands” of high induction factor that appear to be shed from the rotor and are being convected downstream in the rotor wake.



(a)



(b)

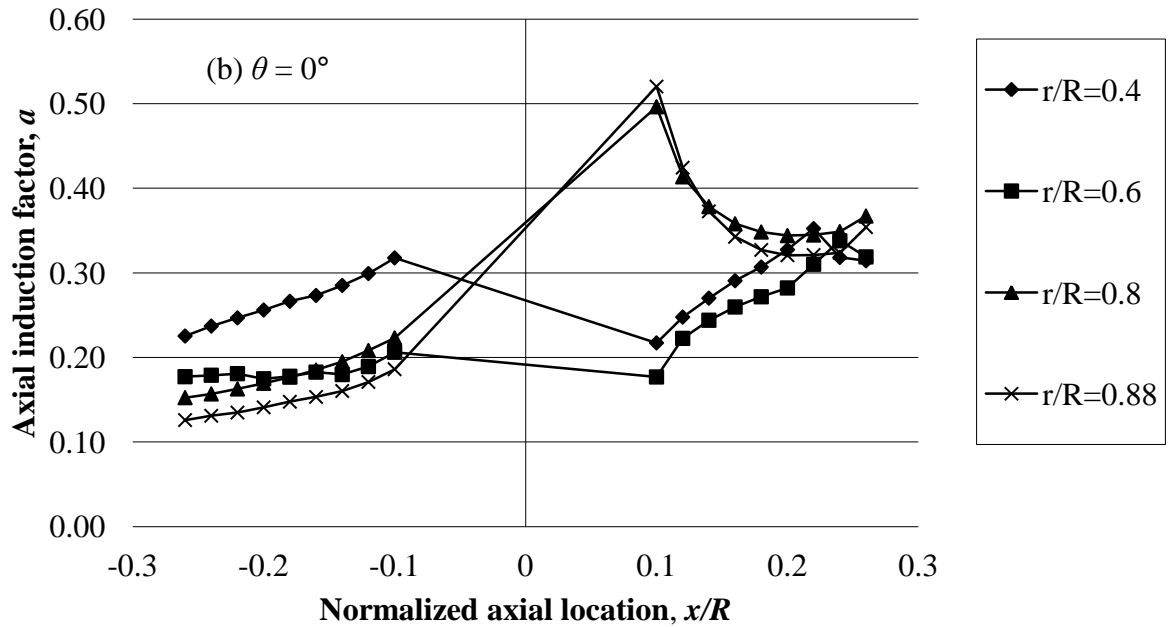
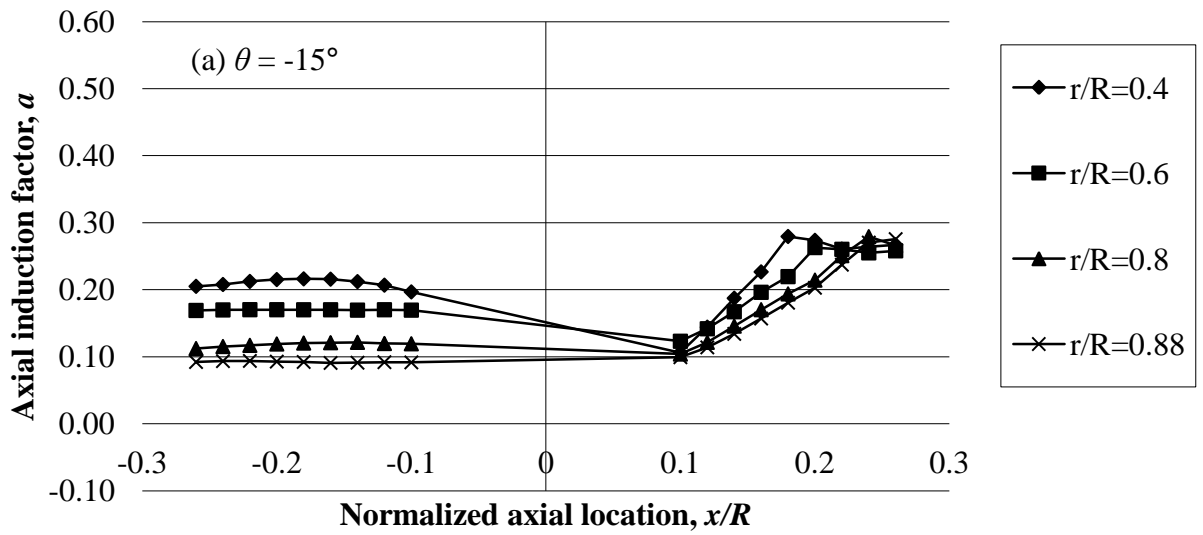
**Figure 5.4: Axial induction factor distribution over the whole flow field and the presence of periodic high induction bands; operating condition:  $U_\infty = 17$  m/s,  $N = 4000$  rpm, (a)  $\theta = 15^\circ$  and (b)  $\theta = 55^\circ$ .**

#### **5.4.1 Variation of Axial Induction Factor in the Axial Direction**

Next, the variation of axial induction factor ( $a$ ) in the axial direction was investigated. From axial induction fields such as Figure 5.4, four profiles at constant radial locations ( $r/R = 0.4, 0.6, 0.8$  and  $0.88$ ) were extracted. Data extracted in this manner reduced the flow information to a smaller number of points in the whole velocity field under investigation. Data

was eliminated very near the rotor plane ( $|x/R| > 0.1$ ) due to high levels of reflection from the blades.

Figure 5.5 shows the axial variation of axial induction factor ( $a$ ) at four radial locations when  $U_\infty = 17$  m/s and  $N = 4000$  rpm ( $\lambda = 6.16$ ) for  $\theta = -15^\circ, 0^\circ, 15^\circ$  and  $35^\circ$ . Similar figures were generated for all of the azimuthal positions and for all tip-speed ratios (90 plots in total). From Figure 5.5 it is observed that for negative azimuth position ( $\theta = -15^\circ$ ), when the reference blade is yet to cross the PIV plane, the axial induction factor ( $a$ ) upstream of the rotor plane remains almost constant in the axial direction at all of the radial locations shown. However, downstream of the rotor plane it increases sharply with axial distance indicating a reduction in the axial velocity as the air moves downstream from the rotor plane. Beyond approximately  $x/R = 0.2$  the axial induction factor ( $a$ ) remains constant. At  $\theta = 0^\circ$  (Figure 5.5 (b)), the value of axial induction factor ( $a$ ) increases while approaching the rotor plane at all radial locations. Immediately downstream of the rotor plane, outboard sections (radial locations near the blade tip) show higher values of axial induction factor than for inboard sections (radial locations near the centre of rotation). This increased value of axial induction factor ( $a$ ) for the outboard section appears to be due to the presence of the tip vortices. For the outboard sections, axial induction factor ( $a$ ) falls sharply farther downstream while the inboard sections increase.



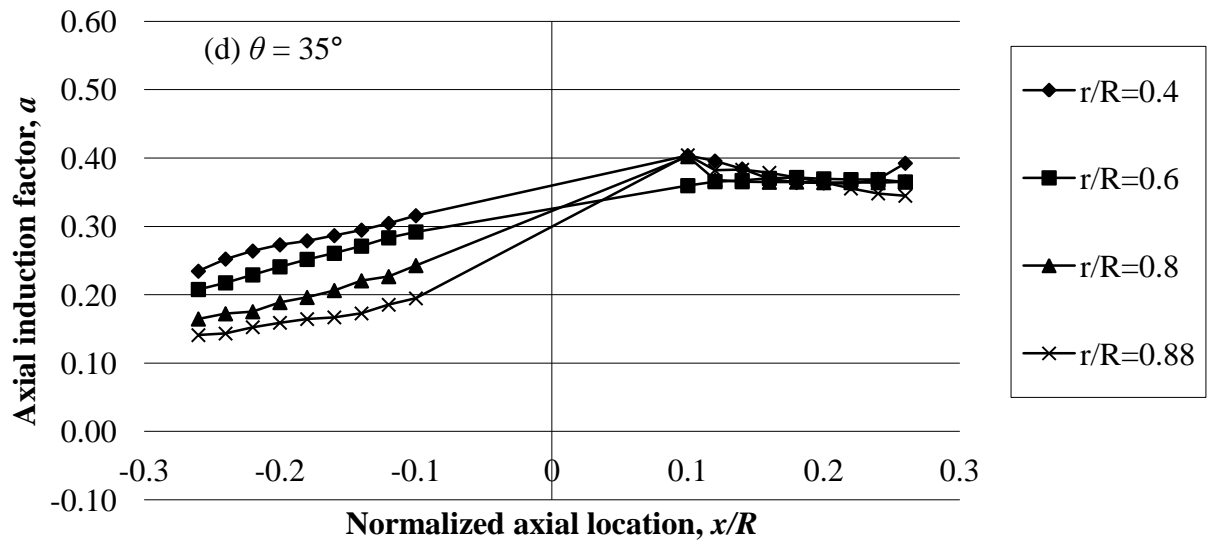
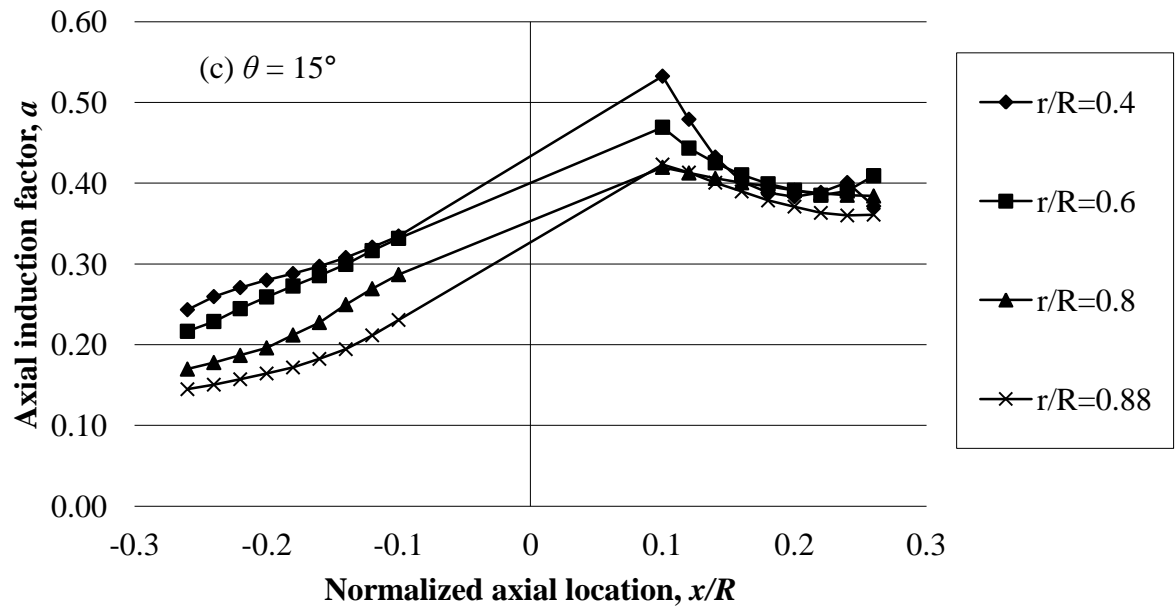
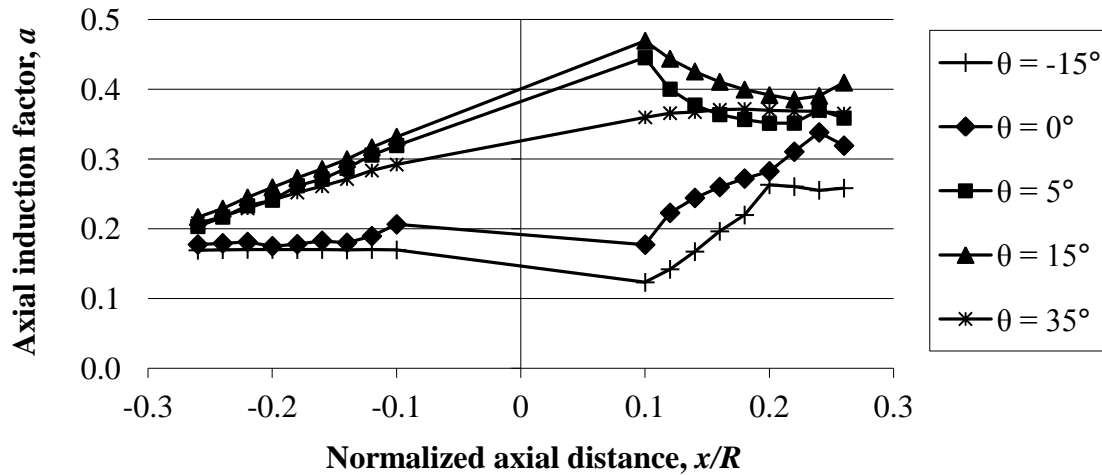


Figure 5.5: Axial variation of axial induction factor (a)  $\theta = -15^\circ$ , (b)  $\theta = 0^\circ$ , (c)  $\theta = 15^\circ$ , (d)  $\theta = 35^\circ$  (Operating condition  $U_\infty = 17$  m/s,  $N = 4000$  rpm and  $\lambda = 6.16$ )

For positive azimuthal angles ( $\theta > 0^\circ$ ) (Figure 5.5(c) and (d)), flow induction upstream of the rotor plane increases at a very consistent rate. For lower positive values of  $\theta$ , downstream, axial locations near the rotor plane show higher values of axial induction factor ( $a$ ) both for the inboard and outboard sections but fall at a higher rate than for higher positive azimuthal positions. The downstream values of axial induction factor ( $a$ ) nearer to the rotor plane for lower positive azimuths are also higher than those for higher positive azimuth positions. However, the higher values of axial induction factor ( $a$ ) were supposed to occur for the sections near the tip only due to the presence of the tip vortices. These higher values of axial induction factor ( $a$ ) for both the sections of the blade near the rotor plane indicate the presence of some trailing edge vortices from the blade which cause these high induction regions in the downstream side.

Figure 5.6 shows the axial variation of axial induction factor ( $a$ ) at a fixed radial location ( $r/R = 0.6$ ) and for different azimuthal angles. The radial location selected for this plot is near mid-span where the velocity field is not expected to be strongly influenced by the tip vortices. This figure shows that at  $\theta = 15^\circ$  the axial induction factor is higher than for all other azimuth angles shown. For this azimuthal position, the axial induction factor ( $a$ ) is higher immediately downstream of the rotor plane and decreases farther from the rotor plane before increasing again.



**Figure 5.6: Axial variation of axial induction factor at  $r/R = 0.6$  for various azimuthal angles (operating condition  $U_\infty = 17$  m/s,  $N = 4000$  rpm and  $\lambda = 6.16$ ).**

### 5.5 Radial Distribution of Axial Induction Factor at the Rotor Plane

In order to determine the radial distribution of axial induction factor at the rotor plane, two profiles were extracted at constant axial distances ( $x/R = -0.1$  and  $x/R = 0.1$ ). Profiles closer than  $0.1R$  to the rotor plane were not possible due to the reflections from the blades.

The values of axial induction factor ( $a$ ) at the rotor plane were obtained by linear interpolation between these two profiles. This was done for all the datasets and for all the azimuthal positions. During this linear interpolation, bending of the blades was not considered (see Appendix). Figure 5.7 shows the radial distribution of axial induction factor ( $a$ ) at the rotor plane at  $\theta = -15^\circ, 0^\circ, 15^\circ$  and  $55^\circ$  for  $N = 3000$  rpm,  $U_\infty = 14$  m/s and  $\lambda = 5.61$ . This figure also shows that at negative azimuthal positions the axial induction factor ( $a$ ) is lower than for positive azimuthal positions. For  $\theta = 15^\circ$  the value of axial induction factor ( $a$ ) at the rotor plane is the highest. These results are consistent with the results showing the axial variation of axial induction factor (e. g. Figure 5.6).

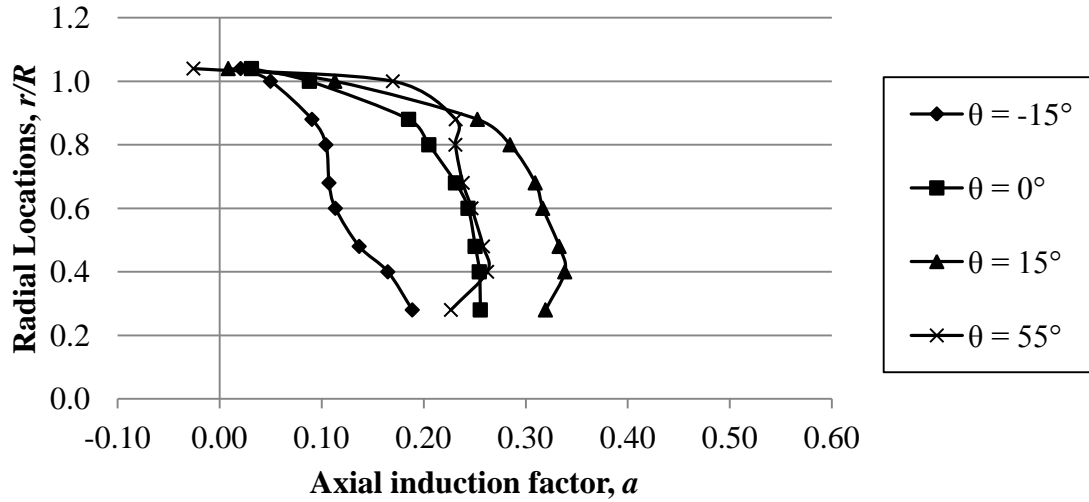


**Figure 5.7: Radial distribution of axial induction factor ( $a$ ) at different azimuthal angles (operating condition:  $N = 3000$  rpm,  $U_\infty = 14$  m/s and  $\lambda = 5.61$ ).**

Figure 5.8 was drawn to find the azimuthal position where the induction is a maximum at the rotor plane. This figure shows the azimuthal variation of axial induction factor ( $a$ ) at four different radial locations for  $N = 3000$  rpm,  $U_\infty = 14$  m/s and  $\lambda = 5.61$ . This figure clearly reveals that at negative azimuth positions, when the blade is yet to pass through the PIV plane, flow induction is low. At all radial locations, except near the tip ( $r/R = 1$ ), the azimuthal variation of axial induction factor ( $a$ ) follows the same pattern and the maximum value of axial induction factor is found at approximately  $\theta = 15^\circ$  for  $r/R = 0.4$  and decreases with the increment of radial distance. At a radial distance of  $r/R = 1$ , the maximum value of axial induction factor ( $a$ ) was found near  $\theta = 35^\circ$ . The value of axial induction factor ( $a$ ) near the tip is highly influenced by the presence of the tip vortices.

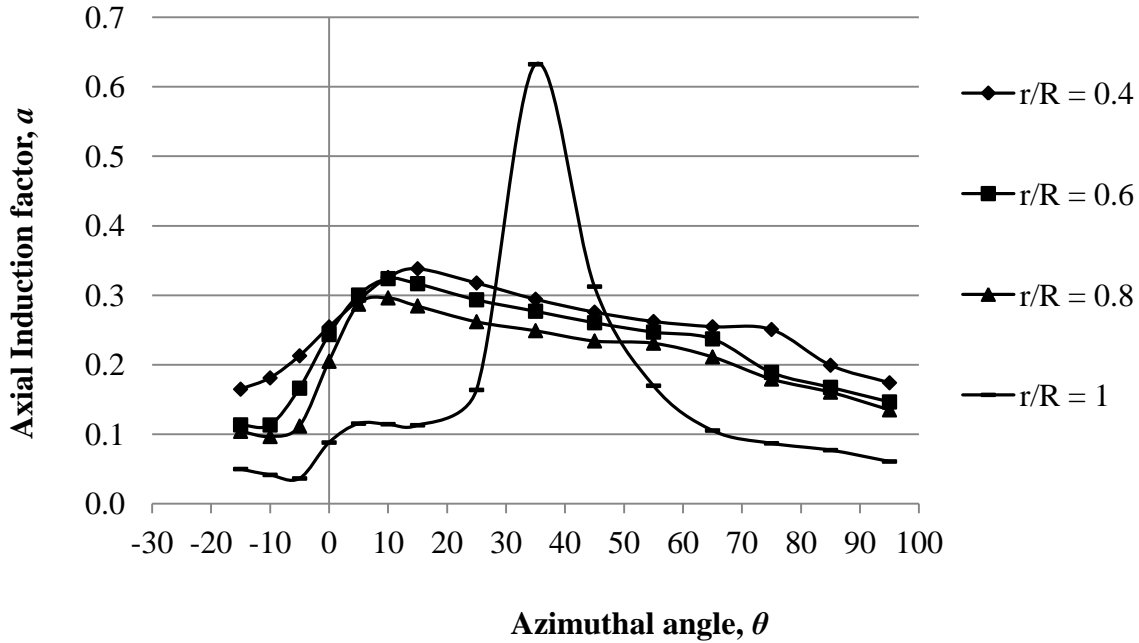


**Figure 5.8: Azimuthal variation of axial induction factor ( $a$ ) (operating condition:  $N = 3000$  rpm,  $U_\infty = 14$  m/s and  $\lambda = 5.61$ ).**

### 5.5.1 Azimuthal Averaging of Axial Induction Factor ( $a$ ) at the Rotor Plane

Section 5.5 described how the radial distribution of axial induction factor ( $a$ ) varies with azimuthal position ( $\theta$ ). One of the objectives of this research is to assess the performance by the Blade Element Momentum (BEM) method which assumes an azimuthally-averaged value of the axial induction factor ( $a$ ) at the rotor plane. To assess the performance of the BEM method the experimental results obtained at 15 different azimuthal positions were next averaged azimuthally. The 15 azimuthal positions selected for taking PIV images were not at regular azimuthal intervals. Azimuthal positions close to  $\theta = 0^\circ$  (in the range of  $-15^\circ < \theta < 15^\circ$ ) were chosen at  $5^\circ$  intervals and the rest of the positions were chosen at  $10^\circ$  intervals (see section 4.3). By applying weighting factors to the axial induction factor ( $a$ ) at different azimuthal positions, azimuthal

averaging of axial induction factor ( $a$ ) at the rotor plane was achieved for all of the operating conditions (tip-speed ratios).

Table 5.1 shows six different operating conditions and corresponding tip-speed-ratio ( $\lambda$ ) values. Figure 5.9 shows how the azimuthally averaged radial distributions of axial induction factor ( $a$ ) at the rotor plane vary with tip-speed ratio ( $\lambda$ ). This figure shows that at lower tip-speed ratios (Cases 1 and 2), the axial induction factor is lower than at higher tip-speed ratios. This indicates that the flow is not slowed down as much at the rotor plane at these operating conditions so not as much energy is being extracted from the approaching air. Most of the flow passes through the rotor plane without much interruption. At these low tip-speed ratios ( $\lambda$ ), inboard sections of the rotor plane have higher values of axial induction factor ( $a$ ) than outboard sections. At tip-speed ratios ( $\lambda$ ) near the optimum operating points (Cases 3 and 4), when the model HAWT is running efficiently, both inboard and outboard sections of the rotor plane show an almost constant value of the axial induction factor around 0.3. This is the “design” axial induction factor ( $a$ ) for the model HAWT (Schenstead, 2012). At higher tip-speed ratios ( $\lambda$ ), the axial induction factor at the rotor plane is higher. At these operating conditions the model HAWT is running very fast compared to the freestream velocity and the flow passing through the rotor plane is reduced significantly. At high tip-speed ratios axial induction factor at the rotor plane is much greater at outboard sections than at inboard sections. This is the opposite to lower tip-speed ratios ( $\lambda$ ).

Table 5.1: Operating conditions and corresponding tip-speed ratios ( $\lambda$ )

Case	Freestream velocity, $U_\infty$ (m/s)	Rotor rotational speed, $N$ (rpm)	Tip-speed ratio, $\lambda$
1	14	3000	5.61
2	17	4000	6.16
3	11	3000	7.14
4	14	4000	7.48
5	13.75	5000	9.52
6	11	4000	9.52

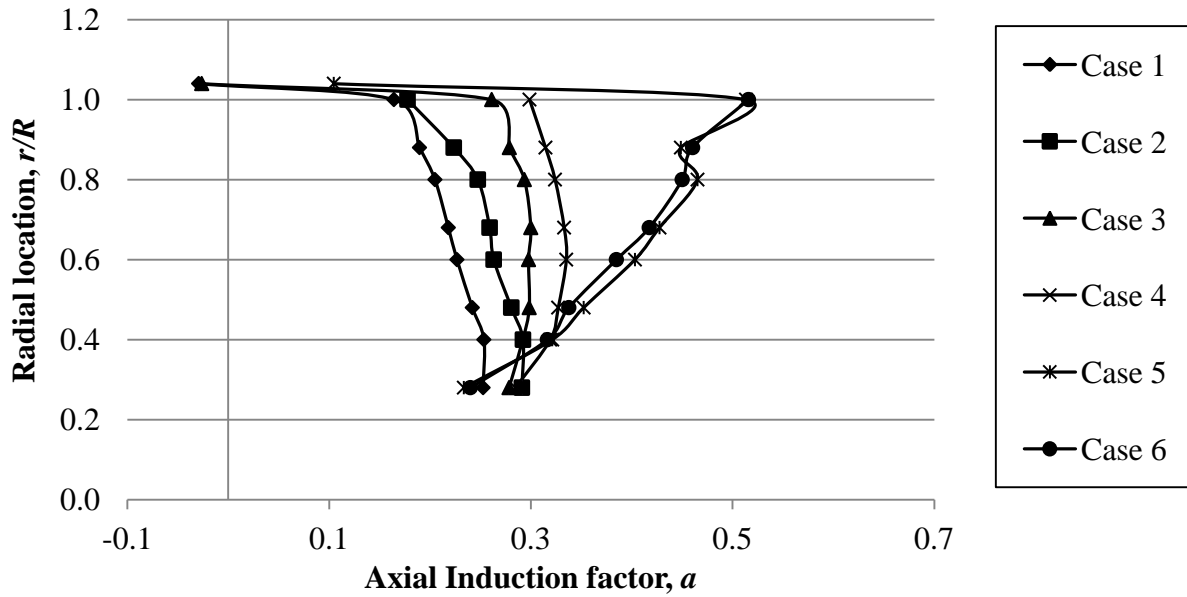


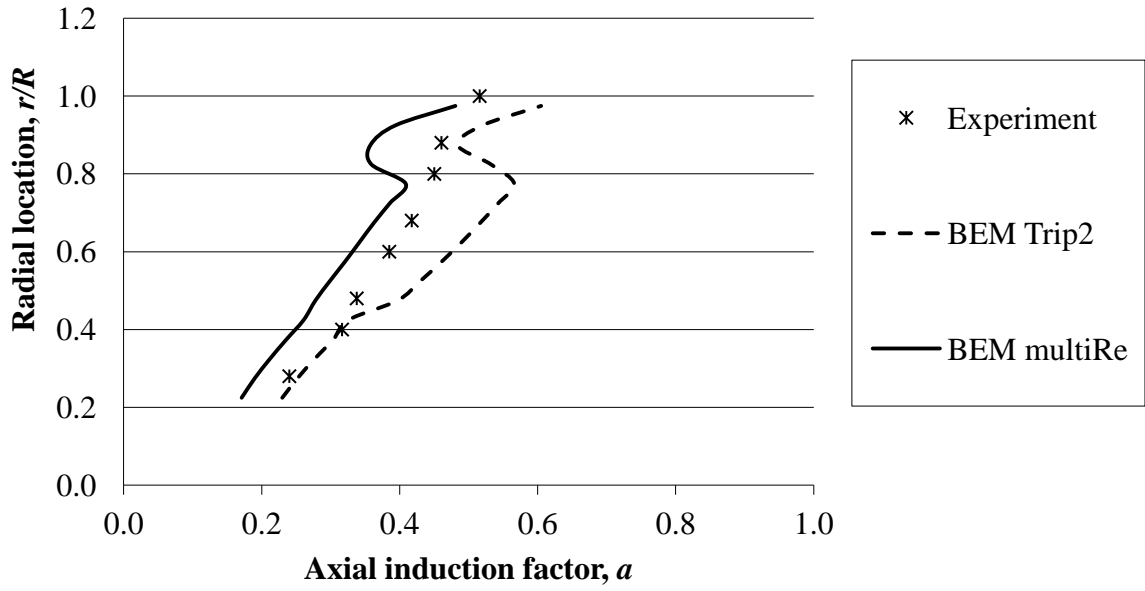
Figure 5.9: Azimuthally averaged radial distribution of axial induction factor ( $a$ ) at different tip-speed ratios ( $\lambda$ ).

## **5.6 Blade Element Momentum (BEM) results**

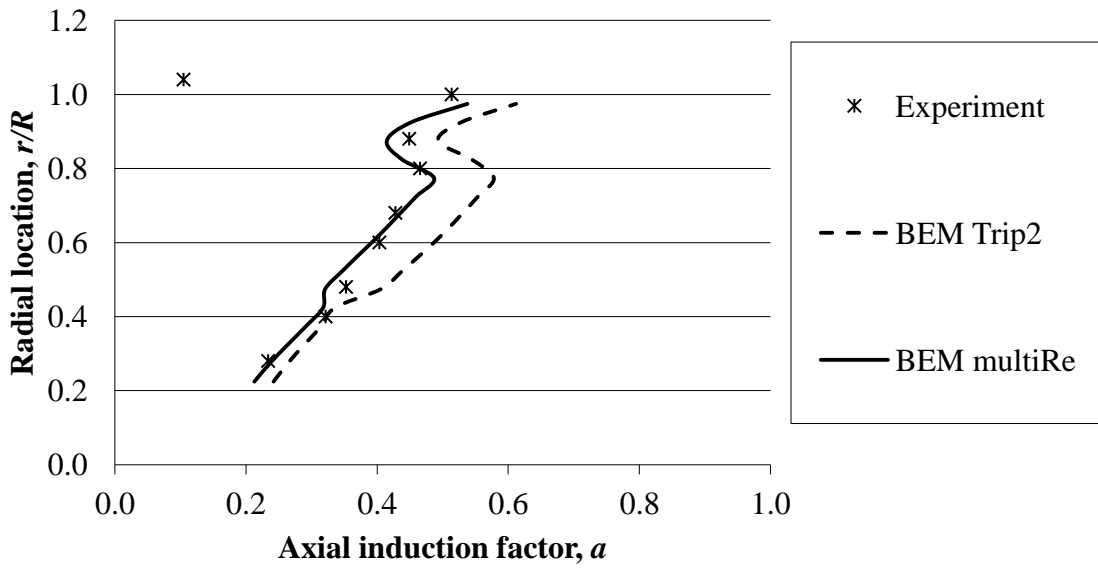
WT\_Perf is a computer code that uses the BEM method to predict wind turbine performance. In this section, the experimental results obtained by PIV will be compared to the results obtained from WT\_Perf to evaluate the performance of the BEM method. WT\_Perf was run at the same operating conditions at which PIV measurements were made. The inputs to WT\_Perf are blade geometry (radial distributions of chord and twist), aerodynamic data for the blade aerofoil sections, and the operating conditions. The model was configured considering one circumferential segment and 16 radial segments with 5000 iterations for the induction factor calculation. The Prandtl's tip loss model, hub loss mode, swirl effects, skewed wake corrections and advanced brake state corrections were activated. The blade element data files obtained from WT\_Perf as outputs contain radial distributions of axial induction factor ( $a$ ) along with other parameters. The BEM predictions were obtained for two boundary layer separation models; MultiRe and Trip2 conditions. Now, the radial distribution of axial induction factor ( $a$ ) will be plotted against the radial locations and compared to the experimental results.

Figure 5.10 compares the BEM predictions to the experimental results for each of the six operating conditions. Figure 5.10 is presented in descending order of the tip-speed ratios ( $\lambda$ ).

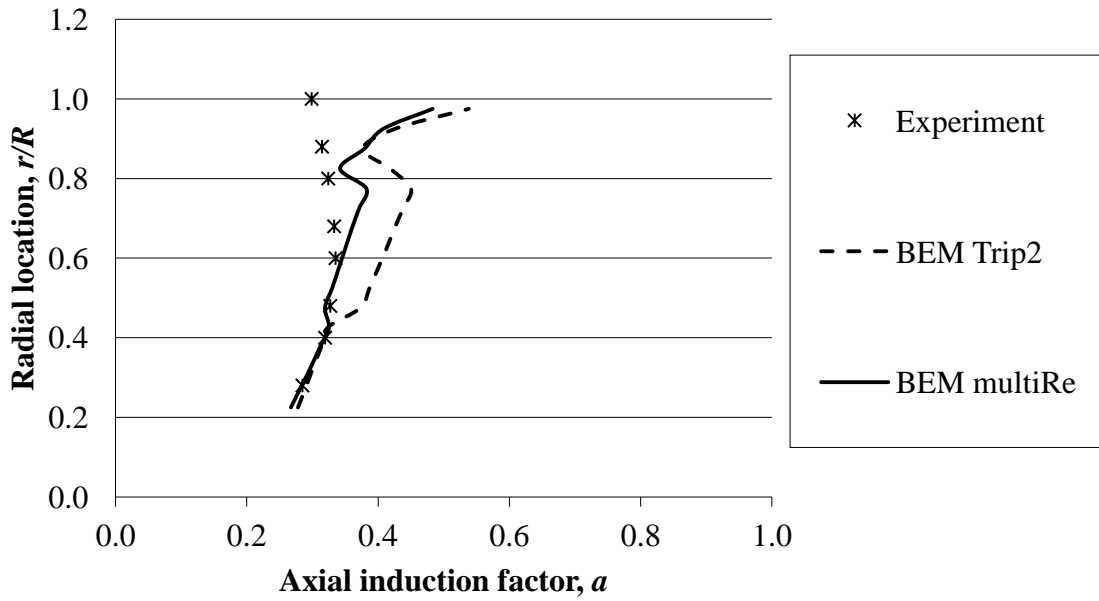
(a) Case 6 ( $\lambda = 9.52$ ,  $U_\infty = 11$  m/s,  $N = 4000$  rpm)



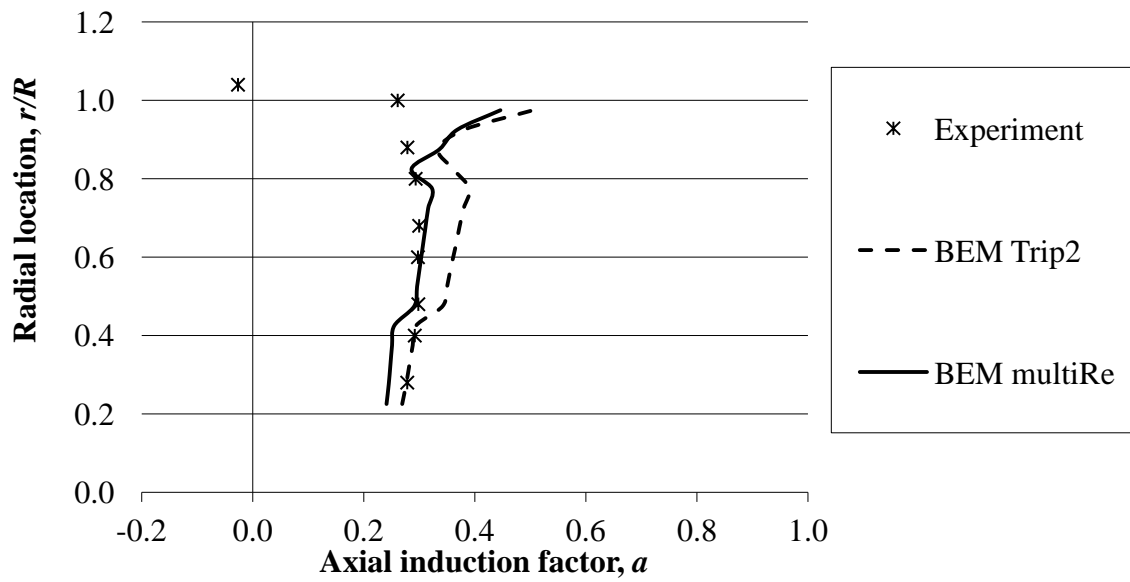
(b) Case 5 ( $\lambda = 9.52$ ,  $U_\infty = 13.75$  m/s,  $N = 5000$  rpm)



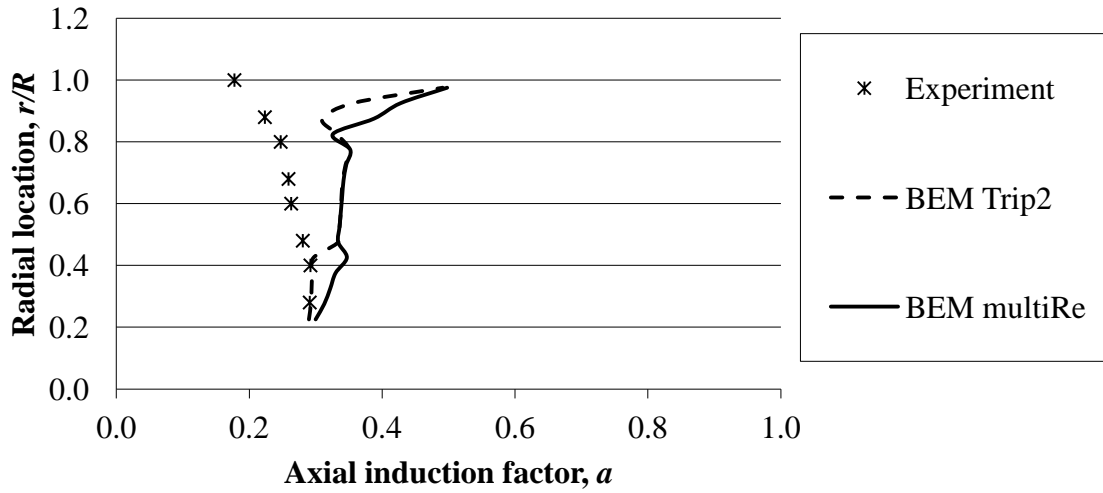
(c) Case 4 ( $\lambda = 7.48$ ,  $U_\infty = 14$  m/s,  $N = 4000$  rpm)



(d) Case 3 ( $\lambda = 7.14$ ,  $U_\infty = 11$  m/s,  $N = 3000$  rpm)



(e) Case 2 ( $\lambda = 6.16$ ,  $U_\infty = 17$  m/s,  $N = 4000$  rpm)



(f) Case 1 ( $\lambda = 5.16$ ,  $U_\infty = 14$  m/s,  $N = 3000$  rpm)

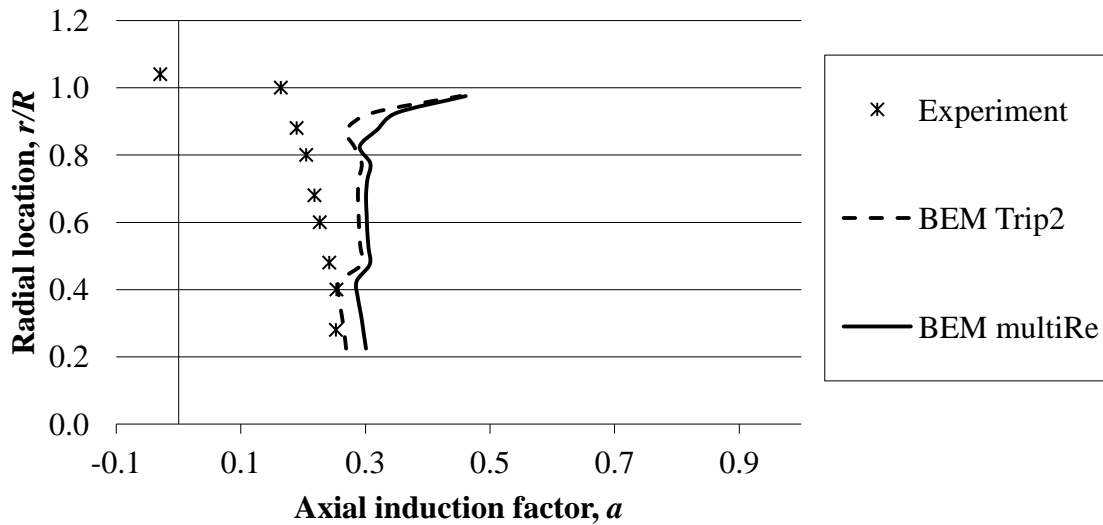


**Figure 5.10: Assessment of BEM predictions of axial induction factor for (a)  $\lambda = 9.52$  (11 m/s and 4000 rpm), (b)  $\lambda = 9.52$  (13.75 m/s and 5000 rpm), (c)  $\lambda = 7.48$  (14 m/s and 4000 rpm), (d)  $\lambda = 7.14$  (11 m/s and 3000 rpm), (e)  $\lambda = 6.16$  (17 m/s and 4000 rpm) and (f)  $\lambda = 5.61$  (14 m/s and 3000 rpm).**

These plots reveal that at the inboard sections of the rotor plane ( $r/R \leq 0.45$ ) BEM predictions match with the PIV results well for all of the operating conditions. The BEM Trip2 (fixed separation point) predictions match the experimental results better than the multiRe predictions. Madsen *et al.* (2007) compared the BEM method to the Actuator Disc (AD) model and reported an overestimation of the axial induction in the inboard sections by the BEM method. However, the current study shows a very good match of induction predicted by the BEM method with the PIV results.

For the middle sections of the rotor plane ( $0.45 \leq r/R \leq 0.8$ ) the BEM predictions are good at tip-speed ratios higher than the optimum tip-speed ratio ( $\lambda = 9.52$ ). The middle section results predicted by the multiRe BEM method are better than the Trip2 calculations. As the operating condition gets closer and closer to the optimum operating point on the performance curve, the BEM predictions show better agreement to the experimental results. At the most efficient operating condition ( $\lambda = 7.14$ ) the predictions are best among all other predictions at the midsection. At tip-speed ratios lower than the optimum operating point ( $\lambda = 6.16$  and  $5.61$ ) the BEM predictions deviate significantly from the experimental results. This strongly demonstrates the accomplishment of the current BEM method to predict the value of axial induction factor near the optimum operating point, where the wind turbines are mostly designed to operate. However, there is also a clear indication of the failure of the BEM method to predict the value of axial induction factor at tip-speed ratios lower than the optimum operating point.

BEM predictions near the tip ( $r/R > 0.8$ ) are the worst among all other sections except for the highest tip-speed ratio (case 5 and case 6,  $\lambda = 9.52$ ). Although the BEM calculations include Prandtl's tip loss corrections, the results deviate significantly from the experimental results at all operating conditions considered except the most inefficient operating condition ( $\lambda = 9.52$ ).

Madsen *et al.* (2007) found that BEM underestimated induction when compared to the Actuator Disc model. However, from this experiment it is observed that the BEM method overestimates the induction factor near the tip region for most of the operating conditions. The experimental results show a decreasing axial induction factor ( $a$ ) with radial distances near the tip and at some operating conditions even show negative values. The negative values of the axial induction factor near the tip are due to the presence of blade tip vortices. The BEM predictions (both multiRe and Trip2) show exactly the opposite trend. Incorporating some modifications regarding tip vortices in the BEM method is necessary to get predictions close to the experimental results.

The BEM predictions of axial induction factor as a function of radial location are not continuous but rather exhibit discontinuities near the radial locations  $r/R = 0.4$  and  $r/R = 0.8$ . This is due to the model HAWT blade design. The model HAWT blade is composed of three different aerofoil sections. The aerofoil properties of these sections are given as input to the BEM. The aerofoil properties of these junctions are not known. In the BEM method these junctions are considered as a step change from one aerofoil section to another. This is the reason of the presence of two step changes in the BEM results.

Two sets of PIV data were taken at operating conditions yielding the highest value of the tip-speed ratio ( $\lambda = 9.52$ , Case 5 and 6). Although the values of the tip-speed ratios for these two datasets are the same, the freestream velocities and rotor rotational speeds are different. The results of these two datasets are presented in Figure 5.10(a) and (b). At this tip-speed ratio ( $\lambda = 9.52$ ), the BEM and PIV results are very similar. The PIV and multiRe BEM results show the best match for  $U_\infty = 13.75$  m/s and  $N = 5000$  rpm.

It is observed that over the range of the tip-speed ratios ( $\lambda$ ) considered for this study, the BEM predictions of power coefficient ( $C_p$ ) are in good agreement with the experimental results. While good predictions of power coefficient ( $C_p$ ) are clearly important, good predictions of the more detailed flow information provided by the axial induction factor ( $a$ ) at all operating conditions are also essential to ensure the model is performing properly. The power coefficients were corrected for the confinement effects of the wind tunnel walls. However, BEM predictions of the radial distribution of axial induction factor ( $a$ ) at the rotor plane are poor at tip-speed ratios lower than the optimum operating condition. Axial induction factor ( $a$ ) is the velocity deficit normalized by the freestream velocity ( $U_\infty$ ). Although no blockage corrections were applied to the axial induction factors presented in this thesis, blockage is expected to have less effect on axial induction factor ( $a$ ) than on power coefficient ( $C_p$ ) since it will increase both the local velocity and the apparent freestream velocity.

# Chapter 6: Conclusions and Recommendations

Realizing the need for experimental datasets describing the flow field around the rotor plane of a wind turbine, flow measurements were taken around a model horizontal axis wind turbine (HAWT) designed by Schenstead (2012). For this purpose, the Particle Image Velocimetry (PIV) technique was used and measurements were taken at six different tip-speed ratios ( $\lambda$ ) on both the upstream and downstream side of the rotor plane along the radius of the rotor.

## 6.1 Summary of Testing

A preliminary test of the model HAWT was performed and the characteristic curve (power coefficient ( $C_p$ ) versus tip-speed ratio ( $\lambda$ )) was drawn to select the operating conditions for the experiment. The tip-speed ratios ( $\lambda$ ) considered for this experiment were 5.61, 6.16, 7.14, 7.48 and 9.52. Two sets of PIV data were taken at  $\lambda = 9.52$  with two different of freestream velocities. These preliminary datasets were corrected for wind tunnel blockage and were compared to the performance curve obtained from the BEM method (WT\_Perf). A good match of the two curves obtained from experiment and BEM was found.

Two hundred pairs of PIV images were taken at 15 azimuthal angles and at six different operating conditions and were analyzed to determine the velocity field. Along with other information, these velocity fields contain information about the axial induction factor ( $a$ ).

## 6.2 Conclusions

1. PIV measurements around the rotor plane of the model HAWT were successfully made at six different operating conditions. The maximum uncertainty in the measurements of tip-speed ratio ( $\lambda$ ) was 0.71%. The uncertainty in the PIV measurement of local velocity was 2.45%.
2. The value of axial induction factor ( $a$ ) was interpolated in the axial direction to find its value at the rotor plane. The maximum value of axial induction factor ( $a$ ) was found at  $\theta = 15^\circ$  at root section and decreases with radial distance.
3. Examining contour plots of axial induction factor in the  $x$ - $r$  plane reveals the presence of periodic high-induction bands downstream of the rotor which are due to the vortices shed from the trailing edge of the blades. The profiles of axial induction factor downstream of the rotor plane gave strong evidence of the presence of these periodic high-induction bands.
4. The value of axial induction factor was averaged azimuthally and interpolated axially to yield the radial distribution of axial induction factor at the rotor plane.
5. The range of experimental uncertainty in the measurements of axial induction factor ( $a$ ) was found to be from 9.8% to 0.15% for a range of axial induction factor ( $a$ ) from 0.2 to 0.9.
6. The axially interpolated and azimuthally averaged radial distribution of axial induction factor ( $a$ ) at the rotor plane was compared to the results of axial induction factor ( $a$ ) predicted by WT\_Perf.
7. The inboard sections of the blade ( $r/R < 0.45$ ) show good agreement with the BEM predictions at all the operating conditions considered.

8. The BEM predictions near the tip ( $r/R > 0.8$ ) show poor agreement with the experimental results. The failure of BEM in the tip region, the section mostly affected by the tip vortices, indicates room for improvement in BEM calculations with regard to vortex effects.
9. The mid-span ( $0.45 \leq r/R \leq 0.8$ ) prediction by the BEM method was very good for higher tip-speed ratios ( $\lambda$ ) and for optimum tip-speed ratio. However, at tip-speed ratios ( $\lambda$ ) lower than the optimum operating condition the prediction differs significantly from the experimental results.
10. The experimental data of radial distributions of axial induction factor ( $a$ ) for the same tip-speed ratio ( $\lambda = 9.52$ ) at the rotor plane show very good match to the BEM results. However, the BEM multiRe predictions are more accurate for  $U_\infty = 13.75$  m/s and  $N = 5000$  rpm.
11. BEM predicts well in the operating conditions higher than the optimum operating condition, better in the optimum operating conditions and differs significantly at the operating conditions lower than optimum tip-speed ratio. BEM predictions at tip-speed ratio,  $\lambda < 5$  could not be assessed due to the limitations of the speed controller.

### **6.3 Recommendations**

1. The existing experimental setup works very well at tip-speed ratios ( $\lambda$ ) higher than that which produces the maximum torque value. However, tip-speed ratios lower than five could not be achieved due to limitations of the speed controller. A different speed controller would be required to obtain stable operation low at tip-speed ratios.

2. The measurement of power using the magnetic brake has significant uncertainty due to the hysteresis inherent in this type of torque measurement. A new power or torque measurement instrument is required for performance testing without this uncertainty.
3. The BEM method also calculates the tangential induction factor. Therefore, for a full assessment of the BEM method, experimental validation of the tangential induction factor ( $a'$ ) along with the axial induction factor ( $a$ ) is required. To measure the tangential induction factor ( $a'$ ), the PIV camera must be repositioned inside the wind tunnel to make measurements in a plane perpendicular to the flow direction.
4. There were no seeding particles in the PIV images in the core of the tip vortices. That is why all the vectors generated inside the tip vortex core were spurious and the tip vortex intensity could not be measured. Choosing smaller seed particles would allow the vortex intensity to be found.
5. One of the walls of the wind tunnel of the high speed test section has a portion of plexiglass which is different from the rest. Taking PIV images through this portion gives attenuated and blurred raw images. PIV image correlation was not very good for these images. Replacing this portion of the wall with a more transparent plexiglass would give better images.
6. Laser reflections from sources other than the tracer particles are always unwanted in PIV images. Reflections from the shiny magnetic brake were found in most of the PIV images taken downstream of the rotor plane. Portions with significant reflections were masked in the PIV analysis. Painting the magnetic brake black would not totally avoid this reflection, but would reduce the problem.

#### **6.4 Contribution to Knowledge**

The BEM method calculates the radial distribution of axial induction factor ( $a$ ) at the rotor plane. Experimental studies for validation purposes of this axial induction factor distribution at the rotor plane are scarce. In this study, the flow around a model, horizontal-axis wind turbine designed and built at the University of Saskatchewan by Schenstead (2012) was measured at six different operating conditions. Radial distributions of axial induction factor ( $a$ ) were found at the rotor plane and BEM predictions were compared to these measurements. BEM fails to predict of the value of axial induction factor at the tip region for most of the operating conditions. However, the predictions are good at the root region. At the mid span region, BEM predicts good in the operating conditions higher than the optimum operating condition, better in the optimum operating conditions and differs significantly at the operating conditions lower than optimum tip-speed ratio. This flow information serves as an excellent database for understanding the aerodynamics of wind turbines and allows code developers to validate their design codes and make improvements by developing correlations for the tip loss correction and other factors.

# List of References

- Abe, K., Ohya, Y. (2004) “An investigation of flow fields around flanged diffusers using CFD” *Journal of Wind Engineering and Industrial Aerodynamics* 92 pp. 315–330.
- Abe, K., Ohya, Y. (2005) “Experimental and Numerical Investigation of Flow Fields Behind a Small Wind Turbine with Flanged Diffuser” *Journal of Wind Engineering and Industrial Aerodynamics* 93 pp. 951–970.
- Adaramola, M. (2008) “The Wake of an Exhaust Stack in a Crossflow” Ph. D. Thesis. University of Saskatchewan.
- Buhl, Jr., M.L. (2004) “WT\_Perf User’s Guide” National Wind Technology Center, National Renewable Energy Laboratory, Golden, Colorado.
- Buhl, Jr., M.L. (2005) “A New Empirical Relationship between Thrust Coefficient and Induction Factor for the Turbulent Windmill State” National Renewable Energy Laboratory Report, Golden, Colorado.
- Chamorro, L.P., Porté-Agel, F. (2009) “A Wind-Tunnel Investigation of Wind-Turbine Wakes: Boundary-Layer Turbulence Effects” *Boundary-layer Meteorology* 132 pp. 129-149.
- Coton, F.N., Wang, T., Galbraith, R.A. McD. (2002) “An Examination of Key Aerodynamic Modelling Issues Raised by the NREL Blind Comparison” *Wind Energy* 5 pp. 199–212.
- Dan-mei, H., Zhao-hui, D. (2009) “Near Wake of a Model Horizontal Axis Wind Turbine” *Journal of Hydrodynamics* 21 pp. 285-291.
- Du, Z., Selig, M. (1998) “A 3-D Stall Delay Model for horizontal Axis Wind Turbine Performance Prediction” *American Institute of Aeronautics and Astronautics* 98-0021 pp. 9-19.
- Du, Z., Selig, M. (2000) “The effect of rotation on the boundary layer of a wind turbine blade” *Renewable Energy* 20 pp. 167-181.
- Ebert, P.R., Wood, D.H. (1997) “The Near Wake of a Model Horizontal-Axis Wind Turbine-I. Experimental Arrangements and Initial Results” *Renewable Energy* 12 pp. 225-243.
- Ebert, P.R., Wood, D.H. (1999) “The Near Wake of a Model Horizontal-Axis Wind Turbine. Part 2 : General Features of the Three Dimensional Wake Field” *Renewable Energy* 18 pp. 513-534.

- Ebert, P.R., Wood, D.H. (2001) “The Near Wake of a Model Horizontal-Axis Wind Turbine. Part 3: Properties of the Tip and Hub Vortices” *Renewable Energy* 22 pp. 461-472.
- Global Wind Energy Council (2010) “Global Wind Report Annual Market Update, 2010”. Accessed July 24, 2012.  
 <[http://www.gwec.net/fileadmin/images/Publications/GWEC\\_annual\\_market\\_update\\_2010\\_-\\_2nd\\_edition\\_April\\_2011.pdf](http://www.gwec.net/fileadmin/images/Publications/GWEC_annual_market_update_2010_-_2nd_edition_April_2011.pdf)>
- Grant, I., Smith, G.H., Liu, A., Infield, D., Eich, T. (1991) “Particle Image Velocimetry Measurements of the Aerodynamics of a Wind Turbine” *International Congress on Instrumentation in Aerospace Simulation Facilities*, Rockville, MD, Oct. 27-31, 1991, Record A92-54301 pp. 23-35.
- Grant, I., Parkin, P. (2000) “A DPIV Study of the Trailing Vortex Elements From the Blades of a Horizontal Axis Wind Turbine in Yaw” *Experiments in Fluids* 28 pp. 368-376.
- Gupta, S., Leishman, J.G. (2005) “Comparison of Momentum and Vortex Methods for the Aerodynamic Analysis of Wind Turbines” *43rd AIAA Aerospace Sciences Meeting and Exhibit 10 - 13 January 2005, Reno, Nevada (AIAA 2005-594)*.
- Haans, W., Sant, T., Kuik, G.V., Bussel, G.V. (2008) “HAWT Near-Wake Aerodynamics, Part I: Axial Flow Conditions” *Wind Energy* 11 pp. 245–264.
- Hansen, M., Madsen, H. (2011) “Review Paper on Wind Turbine Aerodynamics” *ASME Journal of Fluids Engineering* 133 pp. 114001-3.
- Johansen, J., Madsen, H.A., Gaunaa, M., Bak, C., (2009) “Design of a Wind Turbine Rotor for Maximum Aerodynamic Efficiency” *Wind Energy* 12 pp. 261–273.
- Krogstad, P.A., Karlsen, J.A., Adaramola, M.S. (2010) “Performance of a Model Wind Turbine” *17<sup>th</sup> Australian Fluid Mechanics Conference*, Auckland, New Zealand, 5-9 December 2010.
- Lanzafame, R., Messina, M. (2007) “Fluid dynamics wind turbine design: Critical analysis, optimization and application of BEM theory” *Renewable Energy* 32 pp. 2291–2305.
- Madsen, H., Rasmussen, F. (2004) “A Near Wake Model for Trailing Vorticity Compared with the Blade Element Momentum Theory” *Wind Energy* 7 pp. 325–341.
- Madsen, H.A., Mikkelsen, R., øye, S., Bak, C., Johansen, J. (2007) “A Detailed investigation of the Blade Element Momentum (BEM) model based on analytical and numerical results and proposal for modifications of the BEM model” *Journal of Physics: Conference Series* 75 012016.

- Magnusson, M., Smedman, A.S. (1999) “Air Flow Behind Wind Turbines” *Journal of Wind Engineering and Industrial Aerodynamics* 80 pp. 169-189.
- Magtrol Model 6100 Closed loop Speed Control user’s manual, 1<sup>st</sup> Edition, 2005.
- Masson, C., Smaili, A., Leclerc, C. (2001) “Aerodynamic Analysis of HAWTs Operating in Unsteady Conditions” *Wind Energy* 4(1) pp. 1–22.
- Massouh, F., Dobrev, I. (2007) “Exploration of the Vortex Wake Behind of Wind Turbine Rotor” *Journal of Physics: Conference Series* 75 pp. 1-9.
- Medici, D., Dahlberg, J.A., Alfredson, P.H. (2009) “Wind tunnel measurements of the flow upstream a wind turbine: effects on the power production” *European Wind Energy Conference and Exhibition 2009, Marseille, France*. P 108.
- Rostamy, N. (2012) “Fundamental Studies of the Wake Structure for Surface-Mounted Finite-Height Cylinders and Prisms” Ph.D. Thesis. University of Saskatchewan.
- Schenstead, A. (2012) Personal communications.
- Schreck, S., (2002) “The NREL Full-Scale Wind Tunnel Experiment: Introduction to the Special Issue” *Wind Energy* 5 pp.77–84.
- Shen, W.Z., Hansen, M., Sørensen, J.N. (2009) “Determination of the Angle of Attack on Rotor Blades” *Wind Energy* 12 pp. 91–98.
- Shimizu, Y., Kamada, Y. (2001) “Studies on a horizontal axis wind turbine with passive pitch-flap mechanism (performance and flow analysis around wind turbine)” *ASME Journal of Fluids Engineering* 123 pp. 516–22.
- Shinneeb, A. (2006) “Confinement Effects in Shallow Water Jets” Ph.D. Thesis. University of Saskatchewan.
- Snel, H., Schepers, J.G., Montgomerie, B. (2007) “The MEXICO project (Model Experiments in Controlled Conditions): The database and first results of data processing and interpretation” *Journal of Physics: Conference Series* 75 012014.
- Sørensen, J.N., Kuik, G. (2009) “Actuator disc momentum theory for low lambda rotors” *Wind Turbine Wakes Extended Abstracts for Euromech Colloquium 508* pp. 20-22 October 2009, Madrid.
- Toshimitshu, K., Nishikawa, K., Haruki, W., Oono, S., Takao, M., Ohya, Y. (2008) “PIV Measurements of Flows around the Wind Turbines with a Flanged-Diffuser Shroud” *Journal of Thermal Science* 17 pp. 375–380.

- U.S. DOE. Report “20% Wind Energy by 2030.” July 2008. Accessed July 24, 2012. <[http://www.20percentwind.org/20percent\\_wind\\_energy\\_report\\_revOct08.pdf](http://www.20percentwind.org/20percent_wind_energy_report_revOct08.pdf)>
- Vermeer, N., Van Bussel, G.J. (1990) “Velocity measurements in the near wake of a model rotor and comparison with theoretical results” European Community Wind Energy Conference 1990, Madrid, Spain pp. 218–22.
- Vermeer, L.J., Sorensen, J.N., Crespo, A. (2003) “Wind turbine wake aerodynamics” Progress in Aerospace Sciences 39 pp. 467–51.
- Vries, M. (1979) “Fluid Dynamic Aspects of Wind Energy Conversion” AGARD Advisory Group for Aerospace Research & Development AGARD-AG-243 July 1979 pp C4-C9, Amsterdam.
- Whale, J., Fisichella, C.J., Selig, M.S. (2000a) “Correcting Inflow Measurements From Wind Turbines Using a Lifting-Surface Code” Journal of Solar Energy Engineering 122 pp. 196-202.
- Whale, J., Papadopoulos, H., Anderson, C.G., Helmis, C.G., Skyner, D.J. (1996) “A Study of the Near Wake Structure of a Wind turbine Comparing Measurements From Laboratory and Full-Scale Experiments” Solar Energy 56 pp. 621-633.
- Whale, J., Anderson, C.G., Bareiss, R., Wagner, S. (2000b) “An Experimental and Numerical Study Of The Vortex Structure In The Wake Of A Wind Turbine” Journal of Wind Engineering and Industrial Aerodynamics 84 pp. 1-21.
- Werle, M. (2010) “Wind Turbine Wall-Blockage Performance Corrections” Journal of Propulsion and Power 26 pp. 1317-1321.
- Zhang, W., Markfort, C.D., Porte-Agel, F. (2012) “Near Wake Flow Structure Downwind of a Wind Turbine in a Turbulent Boundary Layer” Experiments in Fluids 52 pp. 1219–1235.

# Appendix: The Effect of Blade Deflection on the Interpolation of Axial Induction Factor to the Rotor Plane

## *A.1 Consideration of Blade Deflection in Axial Interpolation of Axial Induction Factor ( $a$ ) at the Rotor Plane*

The thrust force on the model HAWT causes the blades to deflect. The blades also experience centrifugal forces which tend to elongate the blades and reduce the bending effect. The resultant of these forces on the blades, make the blades no longer perpendicular to the flow direction. The amount of blade deflection is most significant at heavily loaded operating conditions. Schenstead (2012) reports that maximum bending is suffered by the model HAWT blade at the most loaded operating condition which is corresponding to the tip-speed ratio,  $\lambda = 6.16$  ( $U_\infty = 17$  m/s and  $N = 4000$  rpm) and this bending effect is most significant near the tip of the blade. He also reported the distribution of deflection along the span of the blades. The bending changes the  $x = 0$  location and affects the linear interpolation of axial induction factor ( $a$ ) to the rotor plane. If the blade is deflected from the nominal rotor plane, then the value of axial induction factor ( $a$ ) at the rotor plane must be calculated as a proper weighted average of the value at the nearest upstream and downstream locations.

Figure A.1 shows the azimuthally averaged radial distribution of axial induction factor at the rotor plane of the model HAWT for the cases when bending was considered and when bending was not considered for the heavily loaded condition ( $\lambda = 6.16$ ). Along most of the blade span, bending has a very minimal effect on the axial induction factor at the rotor plane. Near the

tip region, bending of the rotor plane has the most significant effect on the axial induction factor ( $a$ ). At the heavily-loaded operating condition at the tip of the blades, the difference is about 6%. This difference being small and only occurring very near the tip, bending effects of the model HAWT blades were not considered for any of the operating conditions.

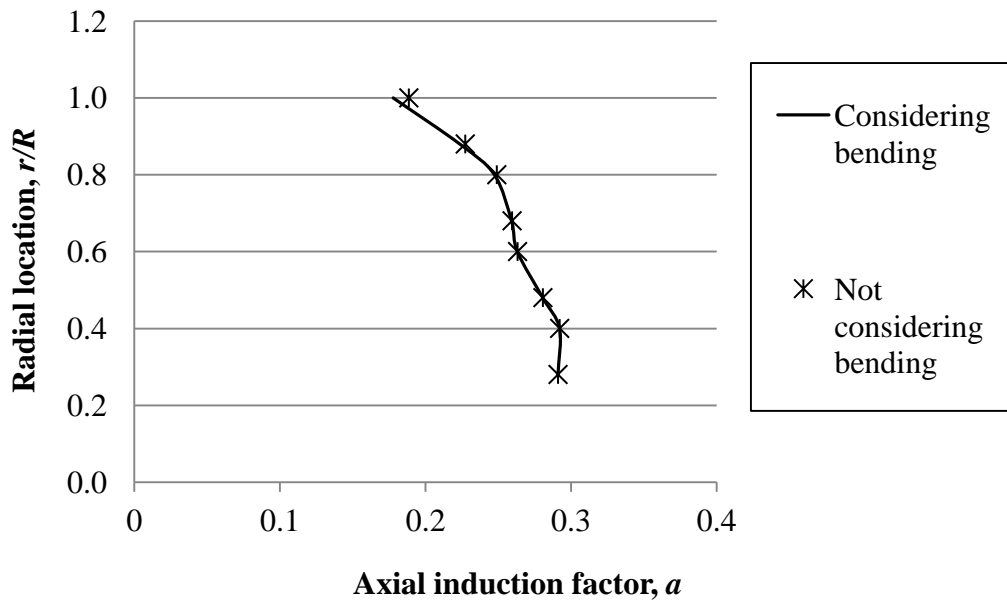


**Figure A.1: Radial distribution of axial induction factor ( $a$ ) at the rotor plane considering and not considering bending effects at heavily loaded condition ( $\lambda = 6.16$ ).**